UNIVERSITÀ DEGLI STUDI DI MILANO
FACOLTÀ DI SCIENZE MATEMATICHE, FISICHE E NATURALI
DOTTORATO DI RICERCA IN
FISICA, ASTROFISICA E FISICA APPLICATA

Development of Detectors for Dosimetry and Spectrometry in BNCT Epithermal Neutron Fields

Settore Scientifico disciplinare FIS/07

Coordinatore: Prof. Marco Bersanelli
Tutore: Prof. Grazia Gambarini
Cotutore: Prof. Amos Breskin

Tesi di Dottorato di:
Giacomo Bartesaghi
Ciclo XXII°

Anno Accademico 2008-2009

Contents

Introduction

The work described in this thesis has been devoted to several physical topics concerning a radiotherapy method that makes use of neutron beams. Studies regarding the neutron transport, the interaction with water equivalent materials and the spectral variations of a neutron beam with energies until few tens of MeV have been carried out.

In the fight against cancer, together with chemotherapy and surgical removal, radiotherapy is one of the most important treatments. Boron neutron capture therapy (BNCT) is an experimental radiotherapy whose aim is to selectively damage the cancer cells releasing heavy charged particles in them. By means of a proper molecular carrier, the isotope boron-10 is accumulated in the tumour cells; afterwards, the patient (or an explanted organ) is irradiated in a neutron field. The high capture cross section of ^{10}B is exploited, causing the emission in the cancer cells of short range ions with high radiobiological effectiveness (RBE), together with a substantial sparing of the healthy tissue without boron. Currently, neutron beams with sufficient intensity for BNCT treatments can only be extracted from nuclear reactors.

In principle, BNCT provides advantages for some kinds of tumours that could make it competitive with respect of radiotherapy treatments with photon and hadron beams. In fact, the heavy charged particles which are emitted by the boron captures have a high RBE value, and can be effective in the control of radioresistant tumours (like glioblastoma). Moreover, providing a boron carrier capable to concentrate itself mainly in the tumour cells, BNCT has the ability to more effectively target multicentric deposits of tumor than is possible with other radiotherapy techniques. The latter characteristic would be exploited in the treatment of diffuse cancers.

The first BNCT experimental treatments were performed during the '50s. Since then, the fortunes of such an experimental treatment varied with ups and downs. Over the last few decades, anyway, the BNCT has progressed slowly but steadily, even if several crucial problems are still present, involving a number of different disciplines. Some of the main problems that are under investigation in order to propose BNCT for clinical treatments concern pharmocokinetics. In fact, the

quest for an effective boron delivery agent is still opened; moreover, it is necessary to develop reliable methods for monitoring the boron concentration in healthy and tumour cells. As far as the design of radiation sources is concerned, groups of nuclear engineers work on the development of facilities capable to provide neutron fields with the desired characteristics in terms of beam quality and accessibility. To this purpose, a lot of efforts are devoted to the development of neutron sources based on accelerators, that could be suitable to be installed in a hospital environment.
Concerning the physical research, dosimetric methods that enable to perform reliable measurements in BNCT fields are still under development. Differently from the conventional radiotherapy, the tissue exposed to a BNCT radiation field is traversed by four distinct radiation components, each one with a different linear energy transfer (LET) and causing the absorption of dose having different RBE. Such a complexity makes dosimetry in BNCT very challenging.
The main goal of dosimetry in BNCT it the measurement of physical dose distributions, which involves characterizing the radiation field by measuring the depth-dose distribution, off-axis profiles, etc., in water equivalent phantoms. Beside the therapeutic dose, aimed to damage the tumour cells, it is important to determine the distribution of the dose due to the undesired radiation components. In fact, for a BNCT treatment the neutron fluence has to be sufficiently high in order to achieve the tumor control; but, on the other hand, the maximum admitted fluence is established on the basis of the absorbed dose in healthy tissues without boron (due mainly to neutron scattering and photons), which has to be within tolerance limits.
The most used detectors for gamma and neutron dose evaluation are paired ionization chambers and thermoluminescence detectors (TLD) but, because of a number of unpredictable factors, such dosimeters can hardly reach an accuracy below 8-10% (one standard deviation). It is therefore recommended to perform both the photon and neutron dose measurements exploiting more than one type of experimental technique.
This thesis concerns the development of radiation detectors for dosimetry and spectrometry in BNCT neutron fields. The first part of the research activity has been devoted to the development of radiochromic gel dosimeters, that are based on Fricke solutions and are manufactured in the laboratory in form of layers. Such gel layer dosimeters, that are based on a gelling agent (Agarose or gelatine) and are infused with a radiochromic Fricke solution, have been proposed some years ago, and they have proved to give a valuable method for determining in-phantom absorbed dose spatial distributions. Recently, they have been named FGLDs (Fricke Gel Layer Dosimeters), and the dosimetric method based on them has been improved. Differently from ionization chambers and TLDs that perform point measurements, FGLDs can provide bidimensional images of the different

dose components absorbed in a water equivalent material. Utilizing Fricke gel dosimeters with different isotopic composition, it is possible to separately obtain images of boron, photon and dose components. In this thesis work, a procedure was studied for measuring 2D spatial distributions of all secondary radiation doses in neutron fields by means of gel dosimeters of suitable isotopic composition.
In order to modify the dosimeter isotopic content without sensibly affecting the neutron transport, the dosimeters are designed in form of layers (typically 3 mm thick). In such a way, radiation transport is primarily determined by the phantom material. Such dosimeters are produced in the laboratory and are analyzed by means of an experimental set up based on a CCD camera. Acquiring and analyzing the transmitted images of a dosimeter, before and after irradiation, it is possible to achieve the difference of optical density for each pixel which is proportional to the absorbed dose. With the MatLab® code a proper software was developed, that allows to perform artefact amendment, thickness correction and a pixel-to-pixel analysis for dose separation.
In this work, FGLDs were used for the characterization of the BNCT facility source of the LVR-15 reactor at the Nuclear Research Institute (NRI) of Řež (Czech Republic), where BNCT clinical trials are performed. Detailed Monte Carlo (MC) calculations, simulating in-phantom neutron transport and dose absorption, were performed by means of the MCNP5 code.
In BNCT radiation beams, one of the most relevant contributions to the absorbed dose in healthy tissue is due to elastic scattering of epithermal and fast neutrons on hydrogen nuclei. The RBE of this radiation component strongly depends on the neutron energy spectrum and is usually determined by means of MC calculations combined with biological measurements. Reliable measurements of neutron spectrum and spatial resolution would be therefore very important for accurate treatment planning. To this purpose, the second part of the research activity described in this thesis concerns the development of a a novel neutron spectrometer with imaging capability, consisting of a neutron moderator, a neutron-to-charged-particles converter and a gaseous detector based on Thick Gas Electron Multiplier (THGEM) electrodes. The latter are charge multipliers that have been originally proposed by the Radiation Detection Laboratory research group of the Weizmann Institute of Science (WIS), in Rehovot (Israel).
The basic idea of the proposed detector is to exploit the Bonner-sphere spectroscopy method in a flat geometry configuration, with the aim to characterize BNCT neutron beams in the energy range between 100 keV and 20 MeV. By mounting neutron moderators of different thicknesses in front of a position sensitive epithermal and thermal neutron detector, different sensitivities for different neutron energies are obtained. By means of suitable deconvolution techniques it is expected to derive information regarding both the spatial and spectral distributions of the fast neutrons within the BNCT beam.

For the detector design, a number of MC simulations has been performed with the MCNP5 code, with the aim of studying and comparing different geometrical configurations and material compositions. A sensitive frontal area of 30×30 cm^2 is planned; anyway, at first a prototype of 10×10 cm^2 has been designed, assembled and tested.
The charged particles escaping from the neutron converter (a 10×10 cm^2 ^{10}B layer, 2 μm thick) are imaged by means of a gaseous detector, based on double THGEM and a 2D read out board. In this work, before assembling the spectrometer, a lot of efforts have been devoted to the development of the imaging gas detector, that by itself could be applied to detect radiation of various qualities. Studying various gas mixtures (based on Ar or Ne plus different percentages of CH_4) and electronic settings, the gas detector imaging performance, together with its gain and stability, was investigated and improved. The development of the gaseous detector was carried out at the Radiation Detection Laboratory of the WIS.
The spectrometer prototype was built, assembling together the gas detector, the neutron converter and a set of moderators. In order to employ a spectrometer in a neutron field with a continuous spectrum and to perform spectral unfolding, it is necessary to accurately characterize the detector response for various moderator thicknesses and neutron energies (Response Functions, RFs). The RFs for a number of discrete energies were determined by means of MC calculations and verified experimentally at a few selected energies, using monoenergetic neutron beams. The irradiations of the prototype were carried out in reference neutron fields at the Neutron Physics Department of the Physikalisch-Technische Bundesanstalt (PTB) in Braunschweig (Germany).
This thesis starts with the description of dosimetric methods applied in BNCT radiation fields (Chapter 1). Then, FGLDs are introduced, together with a description of the read out method and of the analysis algorithms (Chapter 2). MC calculations, concerning in-phantom neutron transport and absorbed dose distribution, were performed simulating the neutron source of the LVR-15 BNCT facility (Chapter 3). Images and profiles of boron, photon and neutron dose distributions were achieved carrying out measurements in water equivalent phantoms. The obtained results were compared with data achieved by means of other experimental techniques (TLDs and paired ionization chambers) and of MC calculations (Chapter 4).
The basic concepts and the design carried out by MC calculations of the neutron spectrometer are described (Chapter 5). Then, the gaseous detector set up is described (Chapter 6) with the experimental activity concerning the detector development with Ar/CH_4 and Ne/CH_4 fillings (Chapters 7 and 8). Finally, the spectrometer assembly and characterization at the PTB neutron source are reported (Chapter 9).

Chapter 1

Dosimetry for BNCT

1.1 Rationale of BNCT

BNCT is an experimental cancer radiotherapy that targets tumour at the cellular level with high LET radiation.
A BNCT treatment is composed by two steps: at first, a boron carrier capable to concentrate itself mainly in the tumour cells is administered to the patient; then, at a proper time after the drug administration, the patient (or the organ) to be treated is exposed to a thermal or epithermal neutron field. ^{10}B nuclides capture slow neutrons with high probability (σ = 3837 b for 25 meV neutrons), leading to one of the following reactions:

$$^{10}\mathrm{B} + \mathrm{n} \rightarrow {}^{4}\mathrm{He} + {}^{7}\mathrm{Li} + 2{,}31\ \mathrm{MeV} + \gamma\ (0{,}48\ \mathrm{MeV})\ (94\%)$$
$$^{10}\mathrm{B} + \mathrm{n} \rightarrow {}^{4}\mathrm{He} + {}^{7}\mathrm{Li} + 2{,}79\ \mathrm{MeV}\ (6\%)$$

The α and ^{7}Li particles release almost all their kinetic energy in the malignant cells, since they have a combined average range of 12-13 μm, comparable to the linear dimensions of a mammalian cell; moreover, being heavy charged particles with a total average energy of 2.34 MeV, they have an elevated LET resulting in a high radiobiological effectiveness (RBE). Therefore, providing an effective tumour-seeking boron carrier, BNCT is in principle a very selective cancer therapy, suitable for radioresistant and diffuse cancers [1].
Despite its complexity, in the last years BNCT has obtained encouraging results, however without passing completely the toxicity and efficacy trials [2, 3]; it needs multidisciplinary efforts in order to become competitive with the traditional radiotherapy based on electrons and photons. The crucial point is the healthy tissue sparing, achievable developing highly selective boron carriers and studying suitable neutron sources. As far as BNCT neutron beams are concerned, it is customary to define the neutron energy ranges as follows:

Thermal: < 0.5 eV
Epithermal: 0.5 eV - 10 keV
Fast: > 10 keV

BNCT experimental treatments carried out until now have been performed with neutron beams provided by nuclear research reactors; in particular, thermal neutron fields, for their low penetration power, are useful only for shallow depth tumour or extracorporeal treatments but for therapeutic benefits to deeper tissues higher energies are necessary. For this reason, in the last two decades significant efforts have been devoted to develop epithermal neutron beams that, thermalizing in the patient tissues, are capable of providing a suitable thermal neutron flux at depths of 8-10 cm [4]. Due to their relevance in the current research, this thesis work focuses on epithermal neutron beams.
From the dosimetric and radiobiological point of view, epithermal neutron beams are very challenging. In fact, the absorbed dose in a patient is due to components of different quality and RBE. Moreover, the total dose and the relative fractions of the various components also depend on the isotopic composition of the irradiated materials and the characteristics of the neutron beam (spectrum, divergence and photon contamination). In order to predict the treatment effects on human tissues, the evaluation of the total absorbed dose is meaningless, and it is necessary to characterize the beam quantifying each dose component in a tissue equivalent phantom [5].

1.2 Absorbed dose components in a tissue equivalent phantom exposed to an epithermal neutron beam

An epithermal neutron beam coming from a nuclear reactor contains unavoidably a certain photon background, and a fast neutron component as well. When such a mixed radiation beam enters in a phantom made of a tissue equivalent material that contains some amount of boron, four dose components are produced [1]:

i) The boron dose: it constitutes the so-called therapeutic dose, that comes from the high LET charged particles produced by thermal neutrons captured by ^{10}B.

ii) The gamma dose: it is due to background photons coming from the reactor column and moderator materials, and from 2.2 MeV photons produced by the hydrogen thermal neutron captures (^{1}H(n,γ)^{2}H, $\sigma = 0.33$ b for 25 meV neutrons). Also 0.48 MeV photons produced by boron captures are present;

anyway they can be ignored from a dosimetry perspective, because they are much less prevalent and less energetic than gammas from hydrogen captures.

3) The neutron dose: it comes from epithermal and fast neutrons scattering in the phantom material, mainly on hydrogen nuclei, and this effect produces locally deposited energy due to recoil protons.

iv) The nitrogen dose: nitrogen is present in various percentages in the different human tissues. The ^{14}N isotope absorbs a thermal neutron and emits a 0.63 MeV proton with the ^{14}N(n,p)^{14}C reaction (σ = 1.9 b for 25 meV neutrons).

The relative contributions to the total absorbed dose of the secondary radiations emitted in the above reported reactions change from point to point in the irradiated volume, and depend on the neutron energy spectrum, on beam geometry and on the size and dimension of the irradiated volume.
The boron, neutron and nitrogen doses, owing to the submillimetric range of the secondary charged particles, can be considered as locally deposited, as far as dosimetric measurements in a given volume are concerned. On the other hand, the 2.2 MeV photons produced by the hydrogen neutron captures have a low mass absorption coefficient in water ($4.7 \cdot 10^{-2}$ g/cm^2 [6]), and typically their energy is deposited some centimeters away from the point where the capture reactions has occurred. Therefore, in a given point of the irradiated phantom, the photon dose depends on the distribution of hydrogen captures in all the surrounding material.
For a given radiation source for BNCT, it is necessary to characterize the beam measuring the distributions of all the dose components in tissue equivalent phantoms. The measurements of such distributions, as for example in-depth or off-axis profiles, enables the determination of the characteristics of the impinging radiation field but also prepares the data to be used for patient dose calculation during the treatment planning processing.
Several methods for BNCT dosimetry have been proposed, whose principal characteristics will be mentioned in the next section; the first part of this thesis work concerns a dosimetric method based on gel dosimeters in form of layer that enables to achieve in-phantom continuous distributions of the absorbed doses.
Primary neutron spectrum differs considerably between various BNCT facilities. From the spectral characteristics strongly depends the neutron diffusion in the tissues, as well as the distribution of nuclear reactions causing the different dose components. In particular, the spatial and spectral distribution of recoil protons, which has a particular relevance from the radiobiological point of view, depends essentially from the fast component of the neutron spectrum. The neutrons dose

absorbed by the healthy tissue determines the maximum neutron fluence that is allowed for a BNCT treatment and it is mainly determined by means of MC calculations. A detailed characterization of the neutron source is necessary for a realistic calculation, and therefore reliable measurements of the neutron energy spectrum and beam divergence would be very important for achieving accurate treatment planning. To this purpose, the second part of this thesis work is devoted to the development of a of a neutron spectrometer enabling to perform spectral measurements of neutron beams in the energy interval between 100 keV and 20 MeV with imaging possibilities.

1.3 Dosimetric methods for BNCT

The presence at the same time of radiation components of different qualities in a phantoms exposed to a BNCT radiation beam, and the high radiation intensity required for treatments make very challenging to perform reliable dosimetric measurements. Table 1.1 shows the main methods employed in BNCT dosimetry; for a detailed review, see [5].
Usually boron and nitrogen dose components are not measured directly, but they are determined from thermal fluence measurements by means of kerma approach [7]. For such a purpose, activation foils are usually employed, providing an uncertainty of 7% in thermal fluence measurements [8]. Other techniques based on active detectors are available, like lithium doped diodes [9] and BF_3 counters [10].
Photon and neutron doses are usually measured by means of paired ionization chambers [8, 11]. These are twin gaseous detectors: one has a tissue equivalent wall and it is sensitive to both photon and neutron components; the second one, having a graphite wall, is sensitive just to the photon component. The response of both chambers is corrected for various factors in order to obtain the respective absorbed dose. Subtracting the dose measured with the graphite chamber from the one read with the tissue equivalent chamber one achieves separately the photon and the neutron doses.

The simple design and the high reproducibility of their response make ionization chambers the reference dosimeters for photon radiotherapy fields; such good characteristics are challenged in mixed photon and neutron fields, and the measurement accuracy is not always satisfying. Nevertheless, the method based on dual ionization chambers is considered as the most feasible for photon and neutron dose measurements in BNCT radiation fields, with estimated uncertainty of 5-10% for gamma ray dose and 15-20% for the neutron dose [1, 8].
Also TLDs can be employed in order to achieve separately different dose components. Two detectors with different sensitivities to different radiation components

Methods	**Quantities to be measured**		
	Thermal neutron fluence	Photon dose	Neutron dose
Activation measurements	×		
Si(Li)-Diode	×		
BF_3 counter	×		
Paired ionization chambers		×	×
TLD	×	×	
Alanine dosimeters	×	×	

Table 1.1: Main methods in BNCT dosimetry; for each method the quantities that can be measured are indicated.

(gammas and thermal neutrons) are needed, and by means of proper algorithms operating on the glow curves, the values of the total responses can be separated into the various contributions [12, 13].
Alanine dosimeters are useful to measure photon absorbed dose [14]. In such dosimeters, free radicals are produced proportionally to the absorbed dose, and they are quantified by the procedure of electron spin resonance. Alanine dosimeters have a not negligible response to thermal neutrons, and the consequent correction has to be carefully evaluated. Recently, a method to produce alanine detector for thermal neutron fluence, by mixing gadolinium oxide or boric acid with alanine, has been presented [15].
All the dosimetric methods described above have different advantages and drawbacks; anyway, it is important to underline that, due to the complexity of the dosimetry of a mixed neutron-gamma ray beam, the accuracy of the dose delivered to a patient required in conventional radiotherapy is difficult to achieve in BNCT applications.
Although a recommendation report exists [5], there is not yet a single internationally accepted standard method for dosimetry in epithermal neutron beams. Therefore, in BNCT dosimetry, the need to compare the results of dosimetric measurements with different methods is greatly emphasized.
This thesis describes a method based on gel dosimeters in form of layer that has valuable capabilities for the dosimetry of BNCT. Such a method has been proposed several years ago from our group, and has been continuously improved. The layer gel dosimeters, based on Fricke solution infused in a gel, are named Fricke gel dosimeters in form of layers (FGDLs).
All the methods described above can perform only point measurements; therefore, if a spatial distribution of absorbed dose has to be evaluated, a scan moving the probe in the phantom has to be carried out. Moreover, most of them are not made of tissue equivalent material. On the other hand, as it will be shown in the next

chapter, FGLDs, have the unique capability to achieve separately continuous 2D distributions of the various dose components in a tissue equivalent material.

Chapter 2

Fricke Gel Layer Dosimeters for epithermal neutron beams

In this chapter the method for BNCT dosimetry based on FGLDs is described. At first, a brief historical overview of gel dosimetry is given, regarding in particular the applications for standard photon radiotherapy (Sec. 2.1). Then, the experimental method based on FGLDs is introduced, and its recent developments are described in Sec. 2.2. Finally, the full description of gel dosimeters and of the method that enables to achieve separately the 2D distribution of the dose components in a tissue equivalent material is given in Sec. 2.3.

2.1 Overview of gel dosimetry

This thesis work is devoted to the development of experimental techniques for radiation measurements in epithermal neutron beams; anyway, it is interesting here to describe the main steps of gel dosimetry development [16, 17], which has concerned mainly the radiotherapy based on photon beams. This overview will provide also a description of the status of the art of gel dosimetry.
In the last decades, the continuous improvement of conformal photon radiotherapy techniques has required a corresponding development of suitable dosimetric methods [18]. In principle, gel dosimeters could be very appropriate for measurements required by modern radiotherapy techniques (as intensity modulated radiation therapy, IMRT [19]), because they are tissue-equivalent, they allow to achieve dose continuous spatial distributions and their response basically does not depend on the radiation energy [20]. In fact, the aqueous gel matrix, in which the radiation-sensitive chemicals are infused, allows to keep in a water equivalent material, with some limitations, the spatial distribution of the radiation induced chemical reactions.

Starting from the '50s, radiation-induced color changes in dyes dispersed in different kinds of gel matrices have been investigated [21]. A fundamental breakthrough in gel dosimetry was due to Gore and Shultz [22], that in 1984 investigated the magnetic relaxation properties of a gel containing the Fricke solution. Fricke solution is a ferrous sulphate solution, proposed by Fricke in 1927 [23]; when it is exposed to ionizing radiation, a number of radiation-induced chemical reactions are caused, which eventually induce the oxidation of ferrous ions (Fe^{2+}) into ferric ones (Fe^{3+}). The Fe^{2+} and Fe^{3+} ions possess different paramagnetic moments and, hence, they differently perturb the relaxation rates of neighboring water protons. In their work, Gore and Shultz demonstrated that changes due to absorbed dose in Fricke dosimetry solutions could be measured using nuclear magnetic resonance (NMR).
In 1986 Appleby et al. [24] reported that Fricke solutions dispersed throughout a gel matrix could be used to obtain 3D spatial dose information if analyzed by magnetic resonance imaging (MRI). Anyway, the sensitivity of Fricke gel dosimeters read out by MRI technique is quite low. For this reason, in 1991 Appleby and Leghrouz [25] proposed to add the metal ion indicator xylenol orange (XO) to the Fricke solution. The XO molecules form with Fe^{3+} ions chemical complexes that show a light absorption peak at about 585 nm. By means of spectrophotometric analysis, a considerably enhancement of the ions detection efficiency was produced.
The main limitation in the use of Fricke gel dosimeters is the time constraint imposed by the diffusion of ferric ions after the irradiation. The introduction of XO gave an advantage also regarding this problem; in fact, such a compound improves the stability of the spatial dose information by reducing the diffusion coefficient of iron ions [26]. During the last years, Fricke solutions with various gelling agents such as gelatine, agarose, sephadex and polyvinyl alcohol were investigated in order to minimize the diffusion coefficient.
In 1958, Hoecker proposed gel dosimeters based on radiation-induced polymerization [27]. Such dosimeters are monomer solutions; when they are irradiated, a polymerization reaction occurs by cross-linking of the monomers induced by the free radical products of water radiolysis, causing a stable distribution of radiation effects.
During the '90s a lot of efforts were devoted to the development of polymer gel dosimeters, and many compositions were proposed [28]. Anyway, even if they do not have the diffusion limitations of Fricke gel dosimeters, there are other significant limitations in their use. Due to the nature of their free radical chemistry, polymer gel dosimeters are susceptible to atmospheric oxygen inhibition of the polymerization processes. As a result, these gel dosimeters have to be manufactured in an oxygen-free environment [29], and inserted in phantoms having walls with low oxygen permeability. Together with the use of potentially toxic chemi-

cals, this problem was a significant limitation in the introduction of gel dosimetry into the clinic.
An alternative polymer gel dosimeter formulation was proposed by Fong et al. in 2001 [30]. In such a dosimeter, named normoxic polymer gel dosimeter, atmospheric oxygen is bound in a metal-organic complex thus removing the problem of oxygen inhibition and enabling polymer gels to be manufactured on the bench-top in the laboratory. In the last years different compositions of normoxic gel dosimeters have been studied [31].
As far as gel dosimeter evaluation is concerned, beyond the main method that is based on MRI, others techniques can be cited. For example, Gore, Maryañski et al. [32] proposed in 1996 an optical scanner for polymer gel read out, based on a laser beam, photodiode detectors and a rotating gel platform. When the gel is irradiated, light scattering microparticles are produced by polymerization. Afterwards, the laser beam scans across the gel between each incremental rotation of the platform, and a set of optical density projections is obtained. Finally, a cross sectional image of the radiation field is reconstructed.
Afterwards, other methods of gel dosimeter analysis have been proposed, like X-ray computed tomography [33], vibrational spectroscopy [34] and ultrasound [35].
Presently, it is common opinion that the potential of gel dosimetry is not fully realized, and the development of both Fricke and polymer gel dosimeters is still going on. In fact, there is not yet consensus on optimal gel formulation or optimal evaluation technique to be used, and to date a number of problems has still to be solved before introducing gel dosimeters in the clinical routine [20].
One of the major problems that have to be faced concerns gel preparation and storage. In fact, the influence of cooling rate on the accuracy of gel dosimeters is known [36]; in particular, an uneven cooling rate during gel preparation produces nonuniform dose sensitivity. This problem affects mainly large volume dosimeters, where temperature inhomogeneities between central and peripheral material are hardly unavoidable during the cooling down process.
In our laboratory a particular approach to gel dosimetry has been proposed, that allows to reduce some problems that commonly affect gel dosimeters. The proposed gel dosimeters are manufactured in form of layer (3 mm thick at maximum) and are based on Fricke solution infused in gel matrices. As it will be described below, FGLDs are radiochromic gels and are imaged before and after the irradiation by means of a CCD camera with an optical band-pass filter. The difference of optical density is proportional to the absorbed dose.
FGLDs, by themselves, enable to provide 2D distributions of absorbed dose, that appears as a drawback if compared with the potentiality of other gel dosimeters to provide 3D distributions. Nevertheless, layer-shaped gel dosimeters allow to attenuate troubles that commonly affect gel dosimeters, because problems are more

manageable; moreover, when applied to BNCT dosimetry, they provide the unique possibility to obtain reliably continuous distributions of the various dose components. In addition, as it will be mentioned in the next section, stacked FGLDs in photon beams, by means of a proper software, can provide a 3D rendering of the absorbed dose.

2.2 Recent developments of FGLDs

In the last years, our group has continuously improved the method based on FGLDs by defining their best chemical composition, by optimizing the image acquisition assessment and by developing a dedicated software for image analysis [37, 38]. The instrumentation required for performing the read out procedure is easily transportable and it can be set up near the irradiation facility.
As far as dosimeter analysis is concerned, algorithms for artefacts amendment due to eventual small defects in the gel structures or inhomogeneous illumination of the sample were proposed [39]; moreover, a procedure to mathematically amend possible thickness inhomogeneity in gel layers was developed [40]. In-phantom irradiation of several stacked gel layers can be performed, together with the use of a software capable to merge several 2D images. In this way, 3D dose distributions were achieved [41].
All these improvements allowed to adopt FGLDs for both photon radiotherapy [42] and BNCT [43] dose distribution measurements. In particular, encouraging advances were recently achieved employing FGLDs in IMRT and high dose rate (HDR) brachytherapy fields. In order to reduce the problems due to sensitivity inhomogeneities, a pixel-by-pixel calibration is carried out irradiating the dosimeter twice in a known uniform photon field, before performing the irradiation in the treatment field. In this way, a correction matrix for sensitivity disuniformity, covering the whole dosimeter area, is obtained. For example, in the evaluation the anisotropy function of a HDR brachytherapy ^{192}Ir source, a disagreement of less than 3% between measured data and data calculated by means of treatment planning software has been obtained [44].
In the following section the procedure for experimental dose imaging in BNCT epithermal neutron beams, based on FGLDs, is described.

Components	Concentration
Gelatine from porcine skin	3% of final weigth
Xylenol orange	0.165 mM
Sulphuric acid	25 mM
Ferrous ammonium sulphate	0.5 mM

Table 2.1: Chemical composition of a *standard* FGLD.

2.3 FGLDs for BNCT beams: materials and methods

2.3.1 Composition

FGLDs are radiochromic laboratory-made dosimeters of various shapes; the ones employed in this work had a rectangular shape with an area of 16×14 cm^2 and a thickness of 3 mm. The gel matrix is contained in a plastic frame, within two sheets (1 mm thick) of transparent polystyrene or polymethylmethacrylate.
In this work, the Fricke gel named *standard* has the following composition: porcine skin gelatine, acting as gelling agent; ferrous sulphate [$Fe(NH_4)_2(SO_4)_2{\cdot}6\ H_2O$)]; sulphuric acid [$H_2SO_4$] and xylenol-orange [$C_{31}H_{27}N_2\ Na_5O_{13}S$], in the amount shown in Table 2.1. It is useful to remark that, in standard FGLDs, solutes are in millimolar concentrations and they have the only role of detecting the effect of radiation without affecting the absorbed dose. Therefore, such dosimeters have an excellent water equivalence.

In order to detect the various dose components that are of interest in BNCT, gels with different isotopic compositions are employed. Beside the standard gel, other kinds of employed gels are: *borated* gel, produced adding to the standard gel 35 ppm of ^{10}B, which corresponds to the typical concentration in a tumour tissue; and *heavy water* gel, analogous to the standard one but made with heavy water (99.99% pure).

2.3.2 Analysis method

The optical density of a material traversed by light at a given wavelength can be defined as follows:

$$OD = \log_{10}(I_0/I) \tag{2.1}$$

where I_0 is the intensity of the light entering in the sample and I the transmitted light intensity. Following the Lamber-Beer law, if the analyzed material con-

tains an absorber substance whose absorption cross section for the considered light wavelength is σ, the optical density can be expressed as follows:

$$OD = nl\sigma \tag{2.2}$$

where n is the absorber concentration and l the optical path length. From the previous equations, it is easily found that the transmitted light intensity is related to the absorber concentration by the following relation:

$$I = I_0 \ \exp(-nl\sigma) \tag{2.3}$$

FGLDs are imaged, before and after irradiation, by placing them on a uniform light diffuser (LLUB by PHLOX®); the intensities of the transmitted light (I_{bef} and I_{aft}) are imaged by means of a CCD camera (uEye by IDS®) as 2D matrices of gray level (GL) indeces. If GL_{bef} and GL_{aft} are the GL matrices acquired respectively before and after the irradiation, the difference of optical density ($\Delta(OD)$) induced by radiation in the dosimeter can be expressed as follows:

$$\Delta(OD) = OD_{aft} - OD_{bef} = \log(\frac{I_{bef}}{I_{aft}}) = \log(\frac{GL_{bef}}{GL_{aft}}) \tag{2.4}$$

From 2.2 comes that the quantity $\Delta(OD)$ is proportional to the variation of absorber concentration, and that it can be quantified by pixel-to-pixel manipulation of the two GL matrices.
When a FGLD is exposed to ionizing radiation, a number of chemical reactions occur that induce oxidation of Fe^{2+} ions into Fe^{3+}. Ferric ions bound to XO molecules form chemical complexes which absorb visible light at a wavelength around 585 nm. Performing the read out analysis by means of a CCD camera equipped with a band-pass filter peaked around the same wavelength, it is possible to measure the yield of ferric ions that, up to saturation effects, is proportional to the absorbed dose. Therefore, for a given pixel, it is found that:

$$\Delta(OD) = k \cdot absorbed\ dose \tag{2.5}$$

that is, the spatial distribution of absorbed dose is linearly proportional to the obtained $\Delta(OD)$ matrix. The sensitivity coefficient k depends on gel composition, and therefore it is affected by unavoidable uncertainties during the preparation process. Moreover, k depends on the cooling down rate during the gelling procedure that can be different in the various regions of the dosimeter; therefore, where it is possible, a pixel-by-pixel calibration in a known uniform photon field is carried out.
The measurements described in this thesis have been carried out at a nuclear reactor where it was not possible to pre-irradiate the gel dosimeters in a known photon

field. For this reason, assuming a single value of k for a given gel preparation, a calibration of some samples has been carried out with a ^{137}Cs source located in Milan.

2.3.3 Separation of the various dose components

The method that allows to separately achieve images of the various dose components is based on irradiating in succession two layer dosimeters, having different isotopic composition, placed at the same position in a water equivalent phantom. In some experimental situations, the symmetry of the set up allows to irradiate in the phantom both dosimeters at the same time. In this way, the dosimeters are exposed to the same neutron and photon fluences.
As described in Sec. 2.3.1, not all the employed kinds of FGLDs are water equivalent; anyway, what is of basic importance for the described method, is that the slight thickness of the layer does not affect the neutron transport in the phantom. In other words, the neutron and photon fluences in the region of space occupied by a layer dosimeter can be considered the same as if the region would be filled with the phantom material. The described method enables to separate the photon dose, which is produced by photons emitted mainly by surrounding phantom material, and the dose due to short range secondary radiation which is produced in the dosimeter itself.
Since standard FGLDs are water equivalent, they are sensitive to gamma dose (D_γ) and neutron dose (D_n) coming from neutron scattering on hydrogen nuclei. Borated gel is produced adding 35 ppm of ^{10}B to standard gel; in this way, it absorbs the same photon and neutron doses of a standard one, and furthermore the boron dose (D_B), that is due to the short range charged particles emitted by boron captures. The separation of D_B from D_γ plus D_n can be achieved irradiating a standard dosimeter and a borated one and analyzing them taking into account the sensitivities of each kind of gel to the different radiation components.
To achieve images of neutron and photon dose, a standard gel is irradiated with a heavy water one. The latter is sensitive to D_γ and D_d, that is neutron dose due to neutrons scattering on deuteron nuclei. The employed algorithm exploits the different effect of epithermal and fast neutrons scattering on protons and deuterons.
In both cases, both dosimeters are imaged before and after the irradiation, acquiring GL matrices; afterwards, suitable algorithms for artifacts and thickness inhomogeneity amendment are applied. Finally, a pixel-to-pixel analysis following the algorithms explained below is performed, enabling to separately achieve the images of the dose components.
In the next two paragraphs the algorithms used for achieving images of the photon, neutron and boron doses are described. As far as images of nitrogen dose are

concerned, they can be achieved with gel dosimeter layers from the boron dose images by applying the ratio of boron to nitrogen kerma factors, as done for example in [45].

2.3.3.1 Boron dose determination

The boron dose distribution is measured irradiating at the same time a borated and a standard dosimeter. Gel samples of both kinds are calibrated by means of a reference photon source, determining the photon calibration coefficients (named respectively k_B and k_{st}).
After that the $\Delta(OD)$ matrix of both dosimeters has been achieved, the response of the standard gel dosimeter is subtracted from the response of the borated one. Taking into account the relative sensitivity of Fricke gel to the products of boron captures with respect to photons (α_B), the boron dose can be obtained as follows:

$$D_B = \frac{k_B \Delta(OD)_B - k_{st} \Delta(OD)_{st}}{\alpha_B} \tag{2.6}$$

By comparing the measured values of $\Delta(OD)$ with the dose values calculated using thermal neutron fluences, obtained by means of activation foils and kerma factors, the relative sensitivity to the ^{10}B reaction products with respect to gamma rays, has resulted that $\alpha_B = 0.41 \pm 0.03$ [45].

2.3.3.2 Photon and neutron doses separation

In order to obtain the separate evaluation of the photon and neutron doses, a standard gel together with a heavy water one are used. The method to measure the neutron dose by means of gel dosimeters, initially proposed for measurements at the epithermal column of TAPIRO research reactor [13], has been now more exhaustively studied and improved.
It is well know that the sensitivity of Fricke dosimeters depends on the radiation LET; the ionization density indeed affects the radical recombination mechanisms. So, for a pair of dosimeters, the $\Delta(OD)$ matrices of the standard and heavy water dosimeters are given by:

$$\Delta(OD)_{st} = \alpha_1 D_\gamma + \alpha_2 D_n \tag{2.7}$$

$$\Delta(OD)_{hw} = \alpha_3 D_\gamma + \alpha_4 D_d \tag{2.8}$$

where the α coefficients represent, for each gel dosimeter, the sensitivities to the respective radiation components. From the previous equations it is possible to

obtain the expressions of D_n and D_γ :

$$D_n = \frac{\alpha_3 \Delta(OD)_{st} - \alpha_1 \Delta(OD)_{hw}}{\alpha_2 \alpha_3 - \alpha_1 \alpha_4 \cdot f} \tag{2.9}$$

$$D_\gamma = \frac{\Delta(OD)_{st} - \alpha_2 D_n}{\alpha_1} \tag{2.10}$$

where $f = D_d/D_n$.
The gel sensitivities to photons (α_1 and α_3) of the two gel dosimeters are determined by calibration with a reference gamma source, irradiating for each preparation some gel samples with doses from 5 to 25 Gy.
As far as dose components due to recoil nuclei are concerned, the following consideration have been made. In the spectral distribution of a typical epithermal neutron beam for BNCT, the quantity of neutrons above 10 MeV is a small fraction of the total epithermal and fast neutrons. The same is valid for the LVR-15 epithermal beam (see Appendix A), that was studied in this work. For this reason, the energy of recoil protons coming from neutron scattering must be below this value Therefore, for the Fricke gel sensitivity to recoil protons (α_2) the results of Bragg peak measurements [46] were utilized, from which emerges a relative response to protons with respect to photons of 85%.
The sensitivity to recoil deuterons α_4 was estimated by general considerations regarding Fricke dosimeter sensitivity dependence on radiation LET. In fact, the higher is the LET, the higher is the ion recombination probability, resulting in an attenuation of *OD* variation for a given absorbed dose. No experimental data about Fricke gel sensitivity to deuterons are available in literature. For the α and ^{7}Li particles emitted in the reactions of ^{10}B, as mentioned in the previous paragraph, a value of 0.41 ± 0.03 has been experimentally measured; then, taking into account that the LET of deuterons of these energies is between those of recoil protons and of the boron emitted particles, it was considered reasonable to adopt as dosimeter sensitivity to deuterons with respect to photons a value of 55%.
The value $f = D_d/D_n$ is not constant in the various regions of the phantom, since it depends on neutron spectrum that varies thermalizing in the phantom material. Anyway, by means of MC calculations, the f values in the phantom were calculated on the beam axis as a function of depth, obtaining a distribution whose narrow spread enables to select a single value of f.

Chapter 3

MC calculations: neutron transport in phantom

The dosimetry method based on FGLDs has been applied as a contribution to the characterization of the LVR-15 reactor epithermal neutron beam. For this purpose, couples of FLGDs have been inserted in water equivalent phantoms and irradiated in the BNCT treatment room.
In BNCT fields, the distribution of the absorbed dose is more sensitive to the shape and composition of the whole phantom in comparison with conventional radiotherapy techniques. In fact, the absorbed dose in a given point of the phantom depends on the source energetic and geometric characteristics, and moreover on the neutron spectral distribution in all the surrounding material in the phantom itself. Incidentally, such a complex situation, together with the assortment of radiation components having different RBE, are the reasons why in all the BNCT facilities the standard calculations for treatment planning are based on MC simulations.
In this work, MC calculations concerning radiation transport and dose distribution in tissue equivalent phantoms exposed to the epithermal neutron beam of the NRI BNCT facility were carried out. Simulations have been performed with the MCNP5 code [47], using as radiation source the same source designed for the treatment planning software (MacNCTPLAN [48]).
Epithermal and fast neutrons (with maximum energy of some MeV) interact within an aqueous material mainly by elastic collisions, eventually achieving thermal equilibrium. In general, as the neutron kinetic energy decreases, the probability of being captured (for example by ^{1}H or ^{10}B nuclei) is raised. For a given incoming neutron beam, it is important to investigate the in-phantom trend of the epithermal and fast components, which are responsible of the neutron dose, and the thermal fluence distribution, which is related to the distributions of photon emission (from hydrogen capture) and boron dose.

Summarizing, a number of MC simulations were performed for the following purposes:

- to investigate the in-phantom neutron transport and thermalization; neutron fluences in an array of points were calculated.
- to calculate the boron dose distribution in a layer containing 35 ppm of ^{10}B, that is is strictly dependent on in-phantom neutron transport and moderation.
- to calculate the on-axis f ratio (see 2.9) on the beam axis, that is necessary for neutron and photon dose separation.

In this chapter, after the description of the MC geometry (Sec. 3.1), just the results concerning the first point are depicted (Sec. 3.2). MC outcomes regarding absorbed dose distributions will be shown in the next chapters, in comparison with experimental data.

3.1 MC geometry

The epithermal column of the LVR-15 reactor ends with a circular collimator mouth having a diameter of 12 cm. Since a not negligible neutron fluence is observed coming from the area outside this mouth, in MC the calculations neutrons are emitted by a plane circular source having a diameter of 32 cm, following a probability distribution that depends on the radial distance from the collimator center. Once the initial position on the source plane has been determined, each neutron is emitted accordingly to both energy and divergence distributions that depend on the initial radial distance of the same neutron. The neutron energy distribution in the central region of the collimator mouth can be seen in Fig. A.3.
Two phantoms employed for measurements have been reconstructed in the MC geometry, both filled with water: the standard phantom ($50 \times 50 \times 25$ cm^3) and the cylindrical phantom (d: 16 cm, h: 14 cm). The standard phantom was placed with the largest face in contact with the neutron source, properly reproducing the real configuration; the same for one of the cylinder basis. In both cases, the symmetry axis was coinciding with the beam axis.
At first, the MC geometry was set in order to investigate the distribution of the three neutron spectral components (thermal, epithermal and fast) on the central plane. In both phantoms, a grid of 32×28 points has been considered, placed on a vertical plane along the beam axis. The grid pitch was 0.5 cm, covering therefore an area of 16×14 cm^2. In each point the neutrons flux, divided in the three energy components, has been calculated.

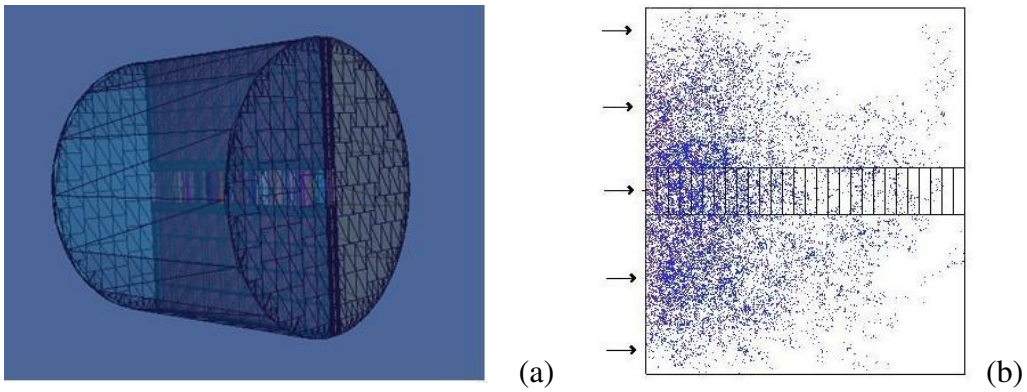

(a) (b)

Figure 3.1: (a) 3D representation of the cylindrical phantom. (b) Cross-sectional view of the cylindrical phantom. Black arrows indicate the incoming neutron beam, and blue points represent the neutron collisions.

In order to simulate the relative boron dose distribution, two $16 \times 14 \times 0.3$ cm^3 layers of aqueous material were inserted in the phantoms, similarly to the layer dosimeters. In one of the layers 35 ppm of ^{10}B were added, and both layers were divided in to 32×28 equal cells. In each cell, the number of boron neutron captures has been calculated. Fig. 3.1(a) shows a 3D representation of the cylindrical phantom; the two layers put on the central plane are visible, together with an array of cells.
Finally, the latter geometry was used also to calculate the ratio between neutron doses in standard and heavy water dosimeters. For such a purpose, the layer containing borated water was replaced with one filled with heavy water. In each cell the energy deposited by scattered neutrons has been calculated. As an example, Fig. 3.1(b) shows a cross section of the cylindrical phantom; the cells along the central axis are visible, and blue points represent neutron collisions.

3.2 Results

Fig. 3.2 shows the distribution of neutron fluxes at three different depths in the cylindrical phantom along the beam axis. Moreover, the entrance neutron spectrum is depicted. The effect of neutron scattering and thermalization is evident: the fast and epithermal components decrease as a function of depth, while a large thermal peak appears.
The results concerning spectral calculations along the central axis can be summarized plotting the trend of the three spectral components (see Fig. 3.3). The exponential decrease of the epithermal and fast components is visible; moreover, the thermal flux increases in the first region of the phantom, reaching its maximum

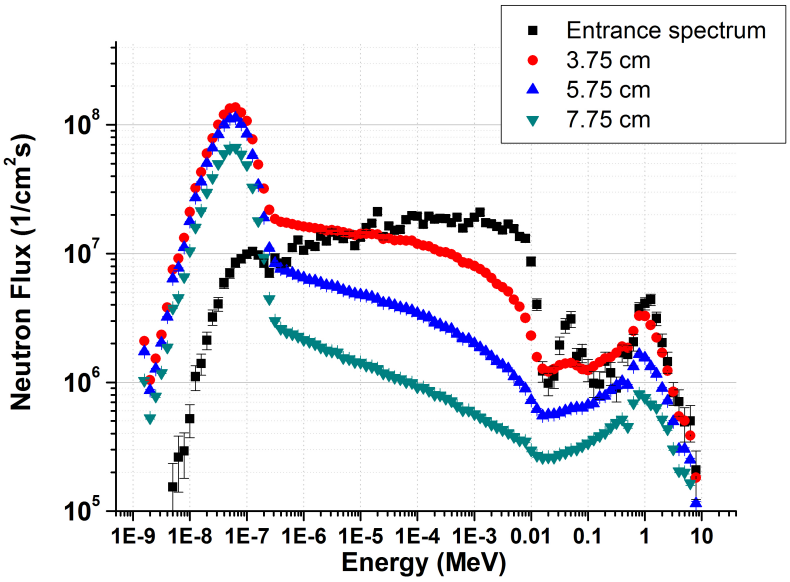

Figure 3.2: Spectral distributions of the neutron fluence at different depths in the cylindrical phantom.

at around 2 cm. As far as boron dose distribution is concerned, it is reasonably to expect its maximum at the same depth. The analogous plots concerning neutron flux on the central axis of the standard phantom are not shown here, because they would be almost indistinguishable from the cylindrical phantom case.

Plots in Fig. 3.4 show a comparison between thermal neutron fluxes on the central plane of the two phantoms. In both cases, a maximum thermal flux of around $9 \cdot 10^8$ cm^{-2}s^{-1} is calculated at a depth of 2 cm. Remarkable differences are visible in the external regions, where the thermal flux is much higher in the standard phantom; in this case, in fact, the larger dimensions of the phantom produce a higher inscattering of thermal neutrons, in comparison with the cylindrical phantom. On the other hand, the thermal flux along the central axis is very similar in the two cases.

Plots in Fig. 3.5 show the epithermal neutron flux in the two phantoms, that steeply decreases as a function of depth. Simulations show that the fast neutron flux (see Fig. 3.6) is about one order of magnitude less than the epithermal one. Comparing both epithermal and fast components between the two phantoms, very similar distributions are obtained, with discrepancies within 1%.

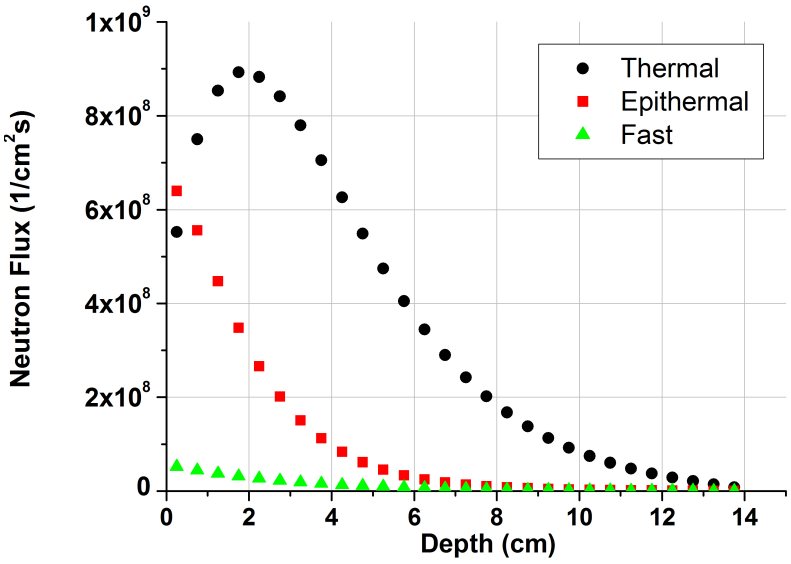

Figure 3.3: Flux of the different spectral components, versus depth in the cylindrical phantoms. Error bars are smaller than points.

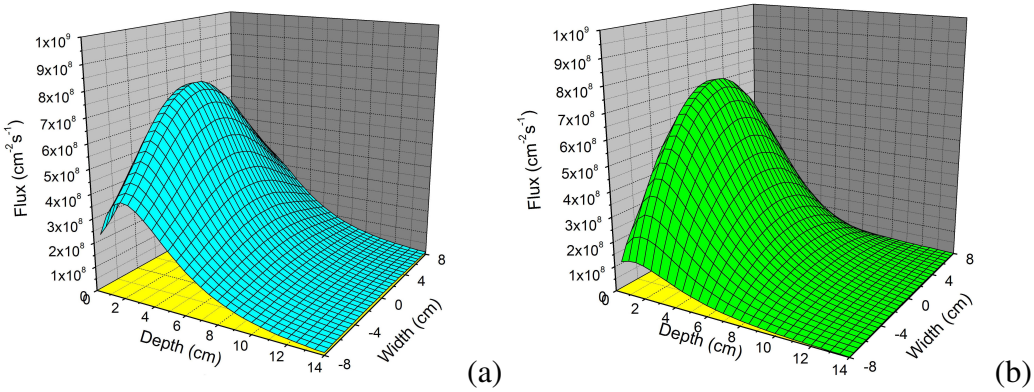

Figure 3.4: Calculated thermal neutron flux on the central plane of the standard phantom (a) and of the cylindrical phantom (b).

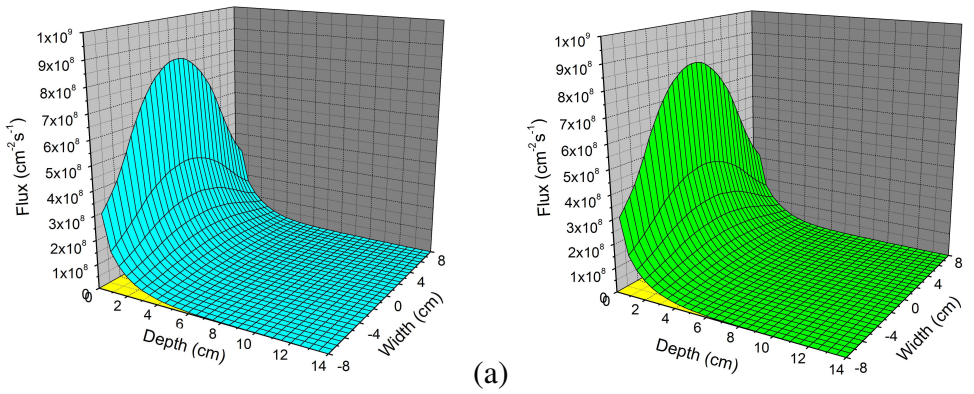

Figure 3.5: Calculated epithermal neutron flux on the central plane of the standard phantom (a) and of the cylindrical phantom (b).

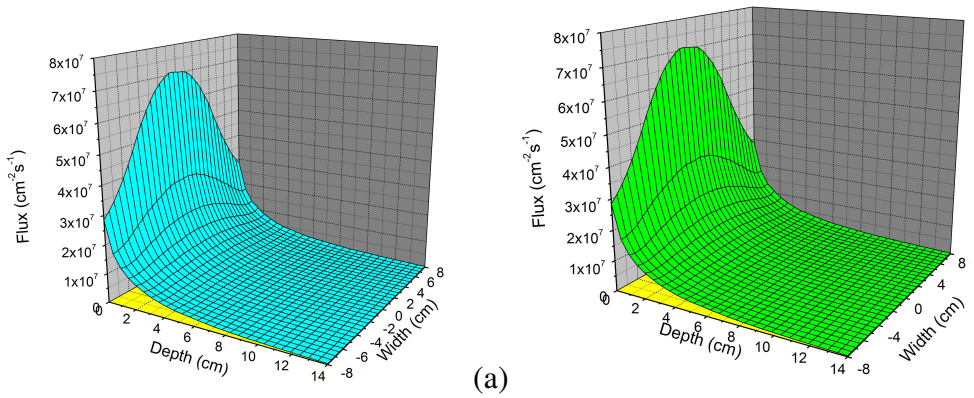

Figure 3.6: Calculated fast neutron flux on the central plane of the standard phantom (a) and of the cylindrical phantom (b).

Chapter 4

Results of dose measurements by means of FGLDs

In this work, FGLDs have been employed for the radiation source characterization of the BNCT facility at the Nuclear Research Institute of Řež (see Appendix A). Couples of dosimeters have been inserted in two different water equivalent phantoms: a cylindrical phantom (d: 16 cm, h: 14 cm), made of non-dosimetric gel, and a standard water phantom ($50 \times 50 \times 25$ cm^3). Fig. 4.1 shows two phantoms containing the gel dosimeters positioned in the treatment room in front of the 12 cm diameter collimator mouth.
In this chapter the results of experimental measurements of dose distributions, carried out with FGLDs, are shown. At first, results concerning boron dose images are described, with particular attention to the dissimilarity of dose distributions in the two phantoms that has been foreseen by MC calculations described in Sec. 3.2. Experimental results are compared with MC calculations (Sec. 4.1). Then, a study concerning the separation of the on-axis neutron and photon doses in the cylindrical phantom is carried out. The results are compared with data taken by means of TLDs and double ionization chambers (Sec. 4.2).

4.1 Boron dose measurements

At first, a boron dose distribution on the central plane of the cylindrical phantom was achieved. Plots in Fig. 4.2 show the images resulting from the analysis of the standard and borated FGLDs, performed after two hours of irradiation. The ^{10}B concentration in the borated gel was 35 ppm. In particular, Fig. 4.2(a) shows the $\Delta(OD)$ matrix of the standard gel multiplied by its photon calibration coefficient (k_{st}, see 2.6); analogously, Fig. 4.2(b) reports the $\Delta(OD)$ matrix of the borated gel multiplied by k_B. These plots represent the effects of photon and neutron

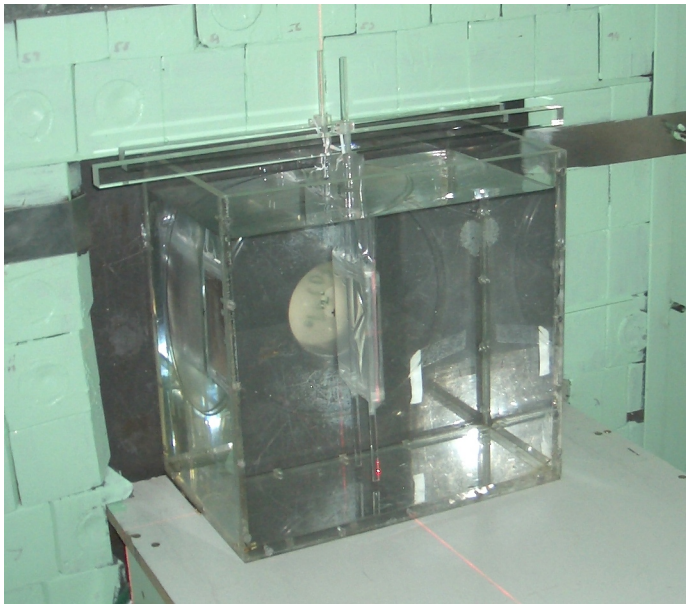

(a)

(b)

Figure 4.1: Standard (a) and cylindrical (b) phantoms in the treatment room. In both cases the gel dosimeters placed in a vertical position are visible.

doses (plus boron dose, in the boron gel) on the dosimeter optical density, multiplied by the respective calibration coefficients that have been determined with a reference photon source. By means of the pixel-to-pixel algorithm (2.6), the 2D

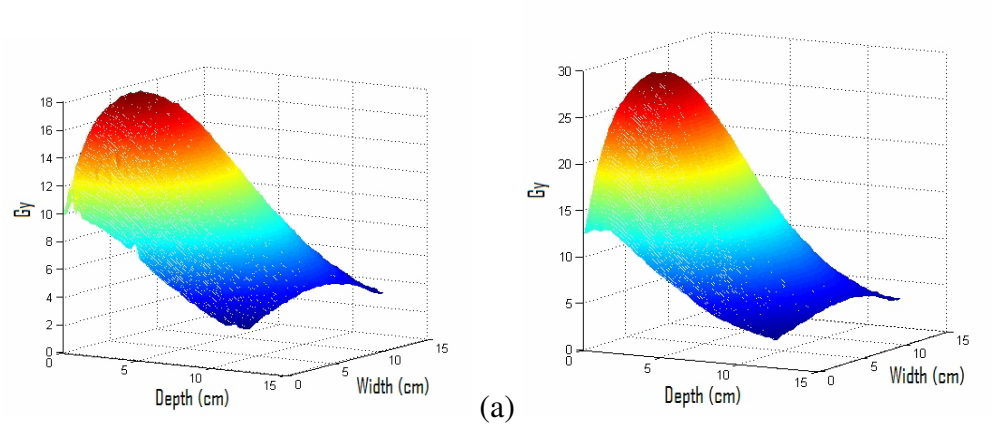

Figure 4.2: Dosimeter responses of a standard (a) and a borated (b) FGLD, given by the $\Delta(OD)$ matrices multiplied by the respective photon calibration coefficients. The cylindrical phantom was placed with its central axis fitting the beam axis; the dosimeters were put on the vertical symmetry plane. With respect to the plots, the beam came from the left.

distribution of boron dose in the central plane is achieved (Fig. 4.3).
From the 2D images of boron dose, it is possible to extract dose profiles in any desired direction. In both phantoms, the measured boron dose rate distributions are strictly related to the calculated thermal neutron fluxes that have been shown in Fig. 3.4. MC data about neutron transport present a strong similarity between the two phantoms, as far as the thermal neutron flux along the beam axis is concerned. Such a similarity is confirmed analyzing the on-axis distributions of boron dose (Fig. 4.4) in the two phantoms. These dose profiles are compared with MC simulations regarding the relative distribution of boron captures in the gel layer. In both cases, the agreement between experimental and MC data is very good.
Beside the in-depth dose profiles, also transverse profiles were studied. Fig. 4.5(a) reports the comparison between gel dosimeters and MC data, regarding transverse profiles of boron dose at three different depths in the cylindrical phantom; MC data have been normalized to the central point of the 2.75 cm depth profile. The comparison is satisfying, with discrepancies within few percents.
The comparison between the calculated thermal fluxes in the two phantoms shows slight differences along the beam axis, while in the regions at larger distance from the axis the dissimilarity increases. This effect has been explained as due to the presence in the standard phantom of a larger amount of surrounding material that increases the neutron inscatter, and it clearly turns out in the comparison between transversal dose profiles in the two phantoms (see Fig. 4.5(b)).
In order to fully understand the described experimental procedure, it is impor-

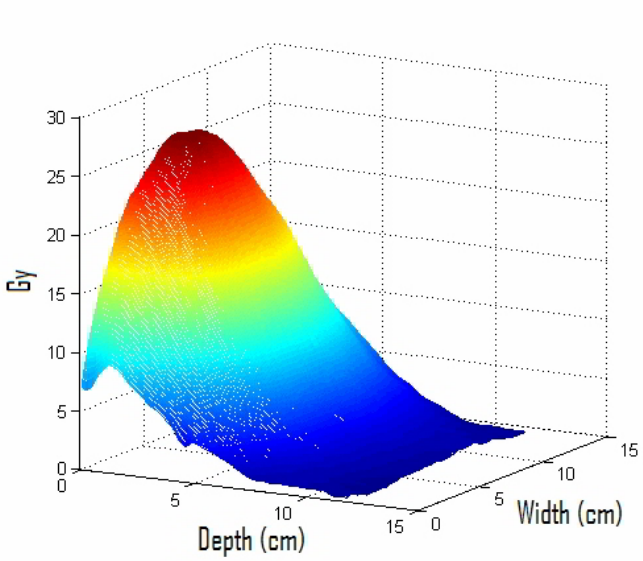

Figure 4.3: Boron dose distribution on the central plane of the cylindrical phantom, after two hours of irradiation. The ^{10}B concentration was 35 ppm.

tant to remark that plots in Fig. 4.2, though expressed in Gy, do not represent the total absorbed dose and neither are proportional to it. The standard dosimeter has absorbed, with different sensitivity, the dose components due to photons and neutrons; the borated dosimeter has absorbed the same doses plus that due to the charged particles generated during boron reactions. What is depicted in Fig. 4.2 is the difference of optical density, representing the effect of the absorbed dose in two the gel layers, multiplied by the respective calibration coefficients related to photon dose. From the matrices shown in such plots, data in Fig. 4.3 are derived by means of the described algorithm, which takes the pixel-to-pixel difference between the two matrices, and normalizes it for the relative gel sensitivity to boron dose with respect to photon dose. In fact, looking at the absolute values of such three plots, it is possible to recognize the effect of the lower sensitivity of gel dosimeters to the boron dose with respect to the photon one. In fact, looking at the absolute values of such three plots, it is possible to recognize the effect of the lower sensitivity of gel dosimeters to the boron dose with respect to photons.

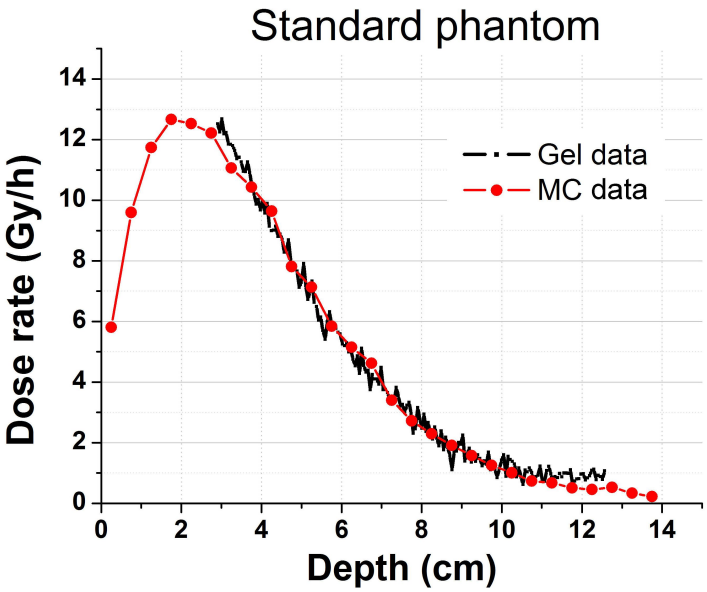

(a)

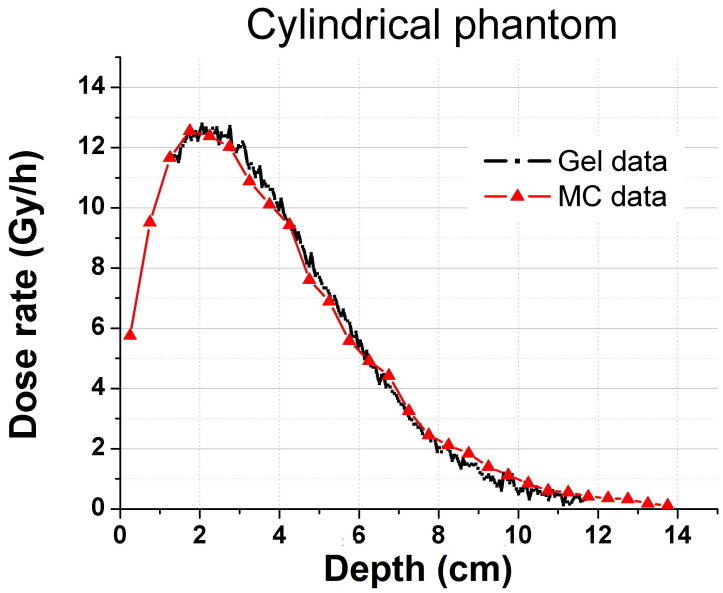

(b)

Figure 4.4: In-depth boron dose rate distributions along the beam axis in the standard (a) and cylindrical (b) phantoms. Data measured by means of FGLDs are compared with MC data, whose error bars are smaller than symbols.

4.2 Photon and neutron dose measurements

The distributions of photon and neutron doses were determined in the standard phantom with coupled standard and heavy water dosimeters. Fig. 4.6 shows exam-

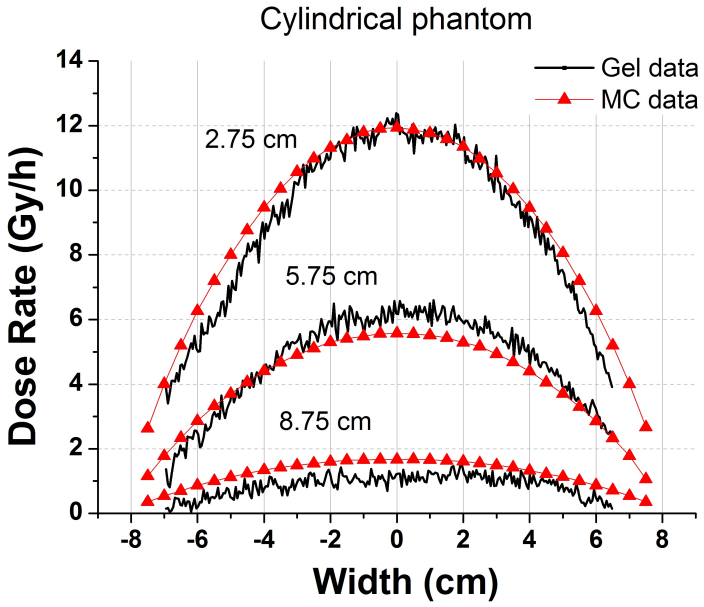

(a)

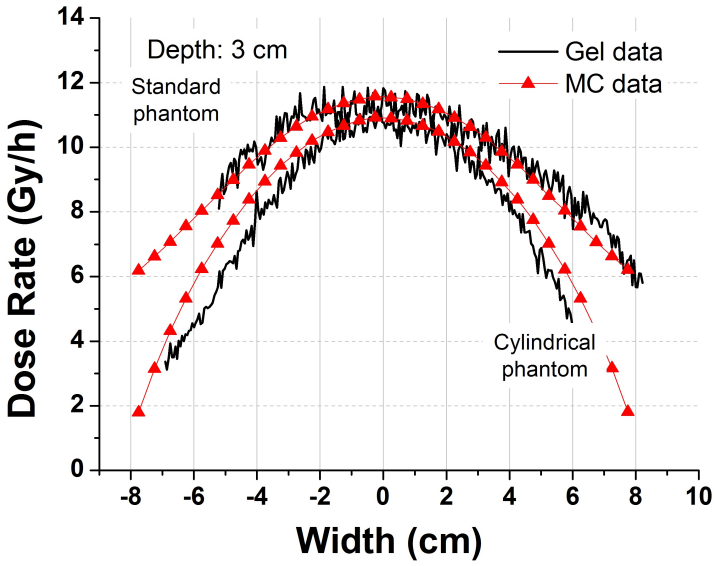

(b)

Figure 4.5: (a) Transverse profiles of boron dose taken at different depths in the cylindrical phantom. (b) Comparison between transverse profiles of boron dose taken at 3 cm depth, in the standard and in the cylindrical phantoms.

ples of $\Delta(OD)$ extracted from the images along the beam central axis. Dosimeters were irradiated for 2h at nominal reactor power. For each dosimeter the response

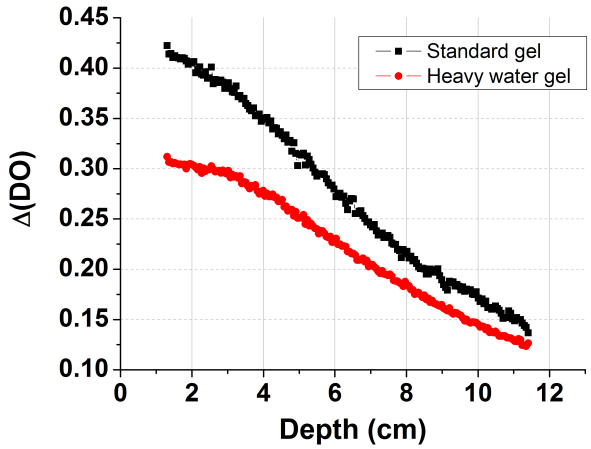

Figure 4.6: Difference of optical density (before and after a 2h irradiation) along the phantom central axis for standard and heavy-water gel dosimeters.

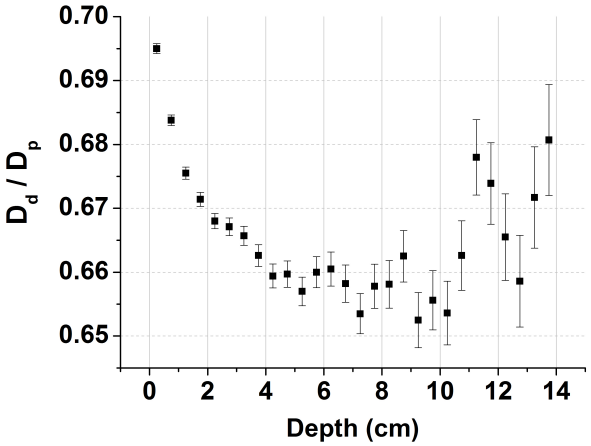

Figure 4.7: Calculated ratio D_d/D_p as function of depth along the beam axis in the standard phantom.

in term of $\Delta(OD)$ is correlated to the total absorbed dose, according to the sensitivity to each dose component. The response of standard gel dosimeter is due to photons and recoil protons and that of gel dosimeter made with heavy water is due to photons and recoil deuterons.
In order to apply the algorithms for dose separation (2.9 and 2.10), the ratio $f = D_d/D_p$ along the phantom central axis has been determined by means of MC calculations, as a function of depth. This ratio, shown in Fig. 4.7, varies with

depth owing to the change in the neutron spectrum. Nevertheless, discarding the first three points (since the dosimeter data are available only beyond 1.4 cm), the standard deviation of the obtained distribution results to be around 1%; therefore, a constant value of 0.665 ± 0.001 has been adopted, calculated as weighted average.

In Fig. 4.8, the obtained photon and neutron on-axis dose profiles vs. depth in the cylindrical phantom are reported. For intercomparison, photon dose data obtained with TLDs are reported too, showing very good agreement. TLD data were achieved using CaF_2:Tm chips (TLD-300), following the method explained in [49]. Moreover, in order to check the trend of the neutron dose, the results of the calculations initially performed for f determination were utilized; such data are given for a single neutron exiting from the collimator mouth, and therefore they were here normalized to the experimental dose at 1.75 cm depth. Error bars on the Monte Carlo data are smaller than symbols, ranging from 0.3% (first point) to 7% (deepest point); the consistency is well evident. Finally, to verify the correctness of the absolute values, neutron dose data measured by Binns et al. [50] with twin ionization chambers are inserted, showing a very good agreement as well.

The good agreement with the results obtained with other experimental techniques confirms the validity of the proposed method for separating neutron and photon doses, and in particular the adequacy of the parameters chosen for the applied algorithms.

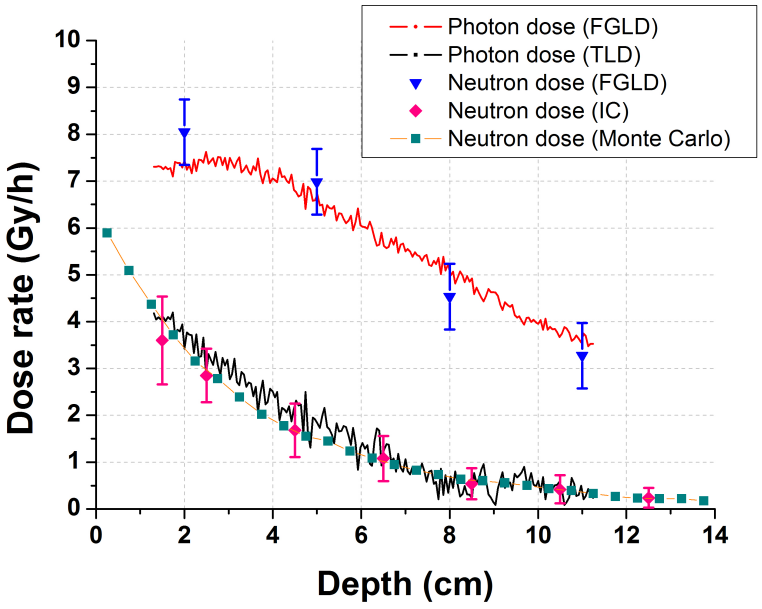

Figure 4.8: Photon and neutron dose rate profiles obtained with Fricke gel dosimeters, photon dose rate values obtained with TLDs, neutron dose rate measured with twin ionization chambers [50] and data obtained by Monte Carlo calculations. All results are reported as a function of depth in the standard phantom along the beam central axis.

Chapter 5

Proposal for a novel neutron spectrometer: design by MC calculations

This chapter describes a study concerning a novel neutron spectrometer based on a neutron-to-charged particle converter and a gaseous detector, whose design has been carried out by means of MC calculations.
Nowadays, between all the existing neutron spectrometers, the method based on Bonner spheres is the most common one [51, 52]. It can provide neutron spectral unfolding on a wide energy range (from meV to GeV), with simplicity of practical operation, but great complexity of the subsequent necessary calculations. In fact, the result of the unfolding procedure is strictly dependent on the a priori knowledge of the neutron field. In particular, not only spectral information is needed, but geometrical characteristics (like divergence) of the neutron fields are needed for a valuable unfolding procedure.
The development of a neutron detector based on neutron moderators with different thickness, a neutron-to-charged particle converter and a position sensitive gaseous detector is here described. The aim of the project is to develop a device with a flat geometry, allowing to perform spectral measurements of neutron beams in the energy interval between 100 keV and 20 MeV with imaging possibilities.
The plane geometry, with moderator blocks wider than the neutron beam collimator mouth, and the imaging capability of the detector are expected to allow more truthful procedures of the unfolding process an then, at the end, more correct results. Also the beam divergence will be less troublesome, because the imaging modality gives the possibility of devising a method for achieving better information about this beam parameter.
Using neutron moderators of different thicknesses in front of the detector, the set up will show different sensitivities for different neutron energies; knowing the RF

for a number of discrete energies from MC calculations and from experimental measurements in monoenergetic beams, it should be possible, by means of a deconvolution process, to get information about the neutron energy spectrum, like in the Bonner sphere method. The flat detector will be suitable for measurements in neutron fields whose divergence is not well known.
A number of MC simulations have been performed by means of the MCNP5 code with the aim of optimizing the neutron spectrometer configuration, by studying and comparing different geometrical configurations and material compositions. Results are presented in the chronological order that led to the final design. Several aspects had to be taken into account in order to design the instrument; the main issues being: evaluation of the spectroscopic capability (by means of the RF calculation), of the detection efficiency and of the imaging performance (spatial resolution as function of the incoming energy and of moderator thickness).
This chapter starts with the investigation of four "general" detector configurations (Sec. 5.1) that are largely schematic. For each of these, a set of five moderators of different thickness have been considered and in every case, several quantities related to spectral and imaging performance have been calculated. The obtained results are shown in plots and tables, to permit a comprehensive comparison among the different configurations. Once the best general configuration was chosen, it was developed by means of more detailed MC calculations, considering a MC geometry closer to the actual experimental set up (Sec. 5.2). During this study as well, the RFs have been calculated and the imaging capability has been estimated. Finally, the ultimate set up was achieved and investigated (Sec. 5.3) with MCNP5, reproducing in detail the geometric and material set up.
In Sec. 5.4, several irradiations with continuous neutron spectra were simulated. The obtained responses, together with the RFs of the various moderators, have been utilized in performing an unfolding algorithm. Even when starting with different default spectra, the spectra obtained by deconvolution were very similar to the original ones, demonstrating the feasibility of an unfolding process with the obtained RFs.

5.1 General configurations

5.1.1 Description of the general configurations

Two kinds of geometrical configurations have been considered, each with two different isotopic compositions of the neutron moderators. Thus, in total, four general configurations have been studied; these are named respectively Lin1, Lin2, Rev1 and Rev2 (see Fig. 5.1). For each one, a set of 5 moderators with different thicknesses has been considered. The aim of this study was to compare the de-

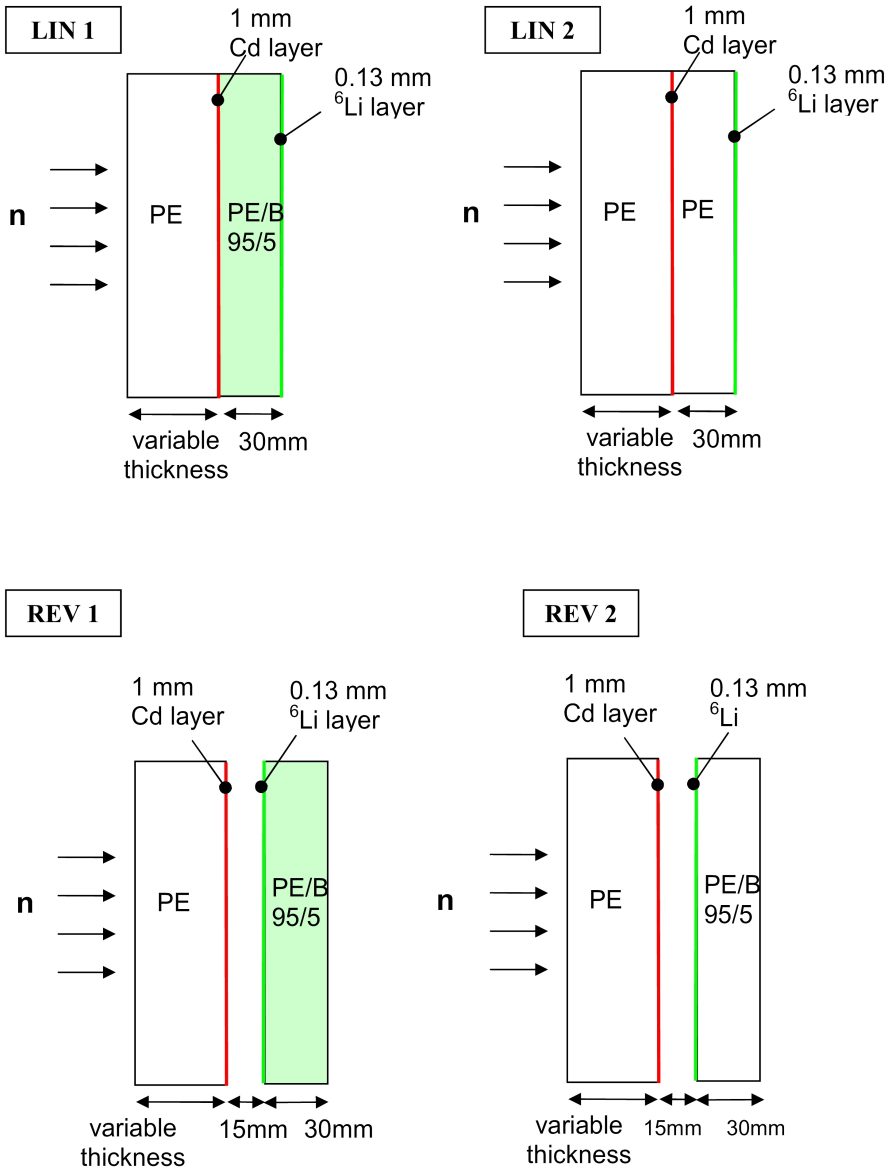

Figure 5.1: Lateral sections of the four general configurations. Lin1 is distinguished from Lin2 by the elemental composition of the moderator second layer; the same applies to the neutron reflector of Rev1 and Rev2. The 15 mm gap in the Rev configurations corresponds ideally to the space occupied by the gas detector.

tector performances achievable with four simple configurations; subsequently, the most promising set up was investigated in detail.
All the configurations have a frontal area of 30×30 cm^2 and contain a neutron-

to-charged-particle converter. Several isotopic compositions have been considered for the converter. In the first steps of the investigation, a converter composed of a 130 μm thick ^{6}Li layer was considered. The idea was to exploit the potentially high thermal neutron detection efficiency (and low gamma sensitivity) of metallic ^{6}Li converters (^{6}Li(n,α)^{3}H, σ = 941 b for 25 meV neutrons [53]), but due to practical issues (as explained below) the detector was finally assembled using a ^{10}B converter. The thickness corresponds to the range of the tritium particles produced in the ^{6}Li neutron capture, maximizing the conversion efficiency [54, 55].
The Lin1 configuration constitutes a neutron moderator made of pure polyethylene (PE) (0.93 g/cm^3), followed by a Cadmium foil (1 mm thick) and by 3 cm of PE 5% Boron doped (0.95 g/cm^3). The boron contained in the plastic was taken into account assuming natural isotopic abundances (^{10}B: 18.8%; ^{11}B: 81.2%).
The basic idea of configuration Lin1 is the following: neutrons moderated in the first PE layer are absorbed by the Cd foil, while those moderated in the second layer (3 cm thick) may diffuse and be captured in the Li foil (and therefore possibly detected). Since the diffusion process causes a loss of spatial information about the incoming radiation, some boron (5% of the total weight) is inserted in the PE between the Cd and the Li layers in order to decrease the neutron diffusion length in this region. Of course employing borated plastic implies a loss of detection efficiency; in order to evaluate the pros and cons of the presence of boron in the second moderator layer, the Lin2 configuration was also investigated, in the same geometrical set up as Lin1 but with the entire moderator made of pure PE.
For both Lin1 and Lin2, a set of five moderators were considered, with total thicknesses of 3, 5, 10, 15 and 20 cm; in the 3 cm case the first moderator layer is omitted.
Rev1 and Rev2 are based on a different concept: neutrons with energies above the Cd absorption threshold ($\sim$ 0.5 eV) can traverse the 15 mm empty gap (in which, ideally, the gas detector should be placed); because of their elevated energy, most of those epithermal neutrons will also cross the Li converter layer and enter the 3 cm thick PE reflector, where they are further moderated and partly diffuse back to the Li layer, where they are ultimately captured and detected.
Following the above considerations about neutron diffusion length, both a set up with the 5% B-enriched reflector (Rev1) and one made of pure PE (Rev2) have been considered. Each Rev configuration is composed of five PE moderators, having thicknesses of 2, 5, 10, 15 and 20 cm, while the reflector thickness is 3 cm in each case.

5.1.2 Response function calculation

For a given general configuration, the response functions (RFs) have been calculated by means of MCNP5 simulations for each moderator thickness. A circular

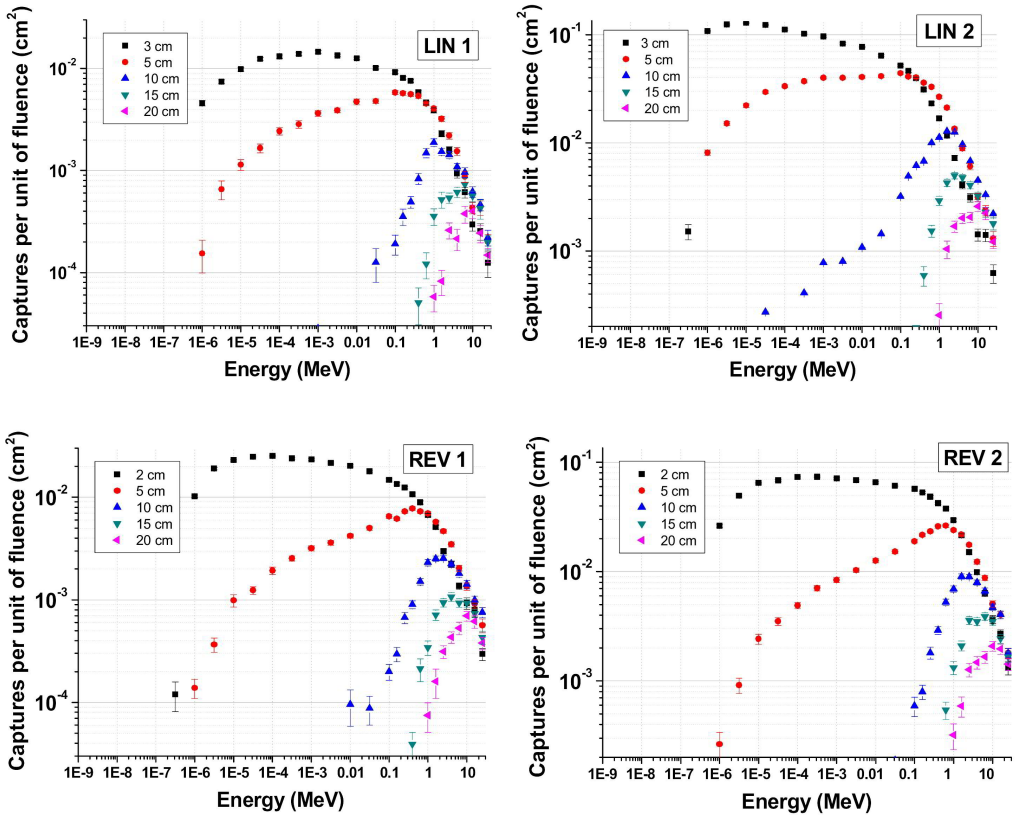

Figure 5.2: RFs of the four general configurations shown for each moderator thickness in terms of neutron captures in the central circular area (d = 1 cm) of the converter layer. Note that plots on the right have different scales than those on the left.

neutron source of 12 cm of diameter irradiating the detector with a parallel beam of neutrons has been considered; the source energy spectrum is composed of 29 discrete energies in the range from 1 meV to 25 MeV.

The employed MC code is not able to follow the ions produced by the boron neutron captures. Therefore, the number of neutron captures has been used as reference for the RF calculation. Of course, this aspect has to be taken into account for the detector absolute calibration.

In the center of the ^{6}Li foil, a cylindrical volume (diameter: 1 cm, height: 130 μm) has been selected, in which the number of neutron captures are counted. Fig. 5.2 shows the RFs of all the configurations, normalized per unit incoming fluence of monoenergetic neutrons.

For a given configuration, increasing the moderator thickness causes the RF peaks

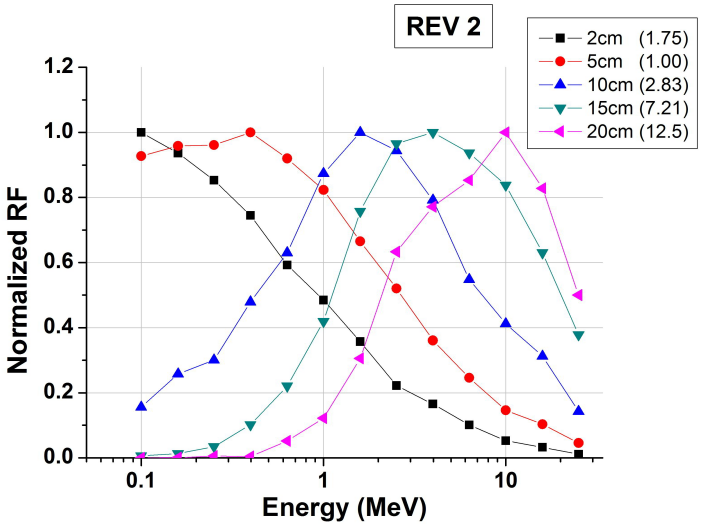

Figure 5.3: Normalized RFs of the Rev2 configurations in the energy range between 100 keV and 25 MeV. The normalization factors applied for each moderator thickness are indicated.

to shift toward higher energies, which is useful for deconvolution purposes; however, a loss of overall efficiency is also apparent. Moreover, in each case the thinnest moderator shows by far the highest sensitivity to epithermal neutrons, with a poorly peaked RF.

As expected, configurations Lin2 and Rev2 (without boron inside) show a greater efficiency than the other cases; in particular, the overall efficiency estimated with moderators of 10 cm, 15 cm and 20 cm is more than four times higher that in the Lin1 and Rev1 cases.

Following the above considerations, as far as the evaluation of RFs is concerned, the Rev2 set up seems to be preferable over the other configurations for the following reasons: i) the absence of boron ensures a higher efficiency; ii) the sensitivity to epithermal neutrons achieved with the thinner moderator is not so high; iii) moreover, the RF obtained with the 5 cm thick moderator is fairly well peaked, unlike the Lin1 and Lin2 cases. Fig. 5.3 shows the RFs of the Rev2 configurations, normalized to the their respective maximum between 100 keV and 25 MeV; the shape of the RFs are significantly different and the peaks appear nicely separated, which is important for deconvolution purposes.

E_n	Moderator thickness	Lin1 FWHM	Lin2 FWHM
0.5 MeV	3 cm	3 cm	5 cm
0.5 MeV	10 cm	7 cm	8 cm
5 MeV	3 cm	2 cm	4 cm
5 MeV	10 cm	5 cm	9 cm

Table 5.1: FWHM obtained for the Lin configurations.

E_n	Moderator thickness	Rev1 FWHM	Rev2 FWHM
0.5 MeV	2 cm	2 cm	6 cm
0.5 MeV	10 cm	9 cm	9 cm
5 MeV	2 cm	2 cm	6 cm
5 MeV	10 cm	9 cm	9 cm

Table 5.2: FWHM obtained for the Rev configurations.

5.1.3 Spatial resolution analysis

For each configuration, the spatial resolution has been evaluated by means of the following method: the central 10×10 cm^2 area of the boron layer was divided into 100 square pixels, and the detector frontal side was irradiated in the center with a monochromatic, collimated neutron beam having a square section of 1 cm^2. The number of neutron captures in each pixel has been calculated, obtaining a 2D distribution. The full width half maximum (FWHM) of such a distribution was chosen as reference parameter for evaluating the spatial resolution.
For each general configuration, four simulations have been carried out; the thinnest and the 10 cm thick moderators have been considered, irradiated with 0.5 and 5 MeV neutron beams. Tables 5.1 and 5.2 show the obtained results; some examples are shown in Fig. 5.4.

In each case, the obtained FWHM is of the order of several centimeters. Factors responsible for this poor value are the fraction of partly moderated fast and epithermal neutrons that diffuse away from the beam axis via multiple scattering and neutrons thermalized in the region behind the Cd shield. Indeed, as expected, the Lin1 and Rev1 configurations, containing boron in all the plastic material, exhibit a narrower FWHM because slower neutrons with long scattering history (and correspondingly large lateral diffusion) are captured by the B.
The Rev1 and Rev2 configurations exhibit a spatial resolution that is not very different from those obtained respectively with Lin1 and Lin2 and, moreover, they provide better RFs, as shown in the previous paragraph. For these reasons, the

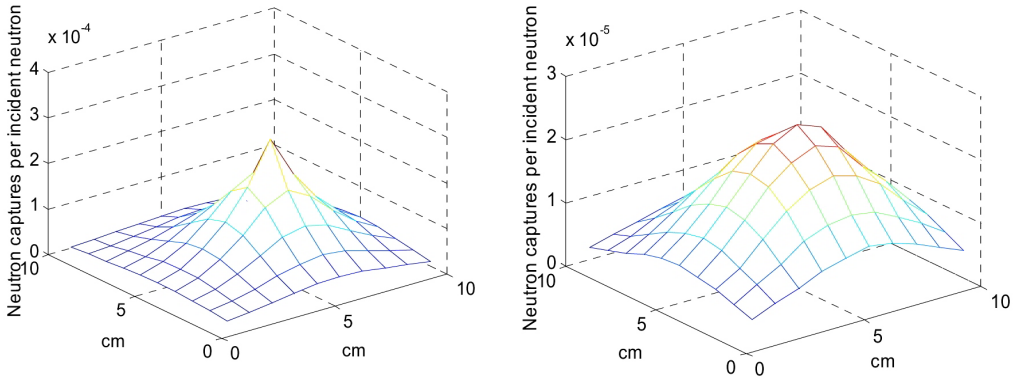

Figure 5.4: Examples of neutron capture distributions in the converter foil, obtained by irradiating the detector with a square beam (area: 1 cm^2) of 0.5 MeV neutrons. Such distributions have been obtained in the Lin1 configuration, with a 3 cm (left) and a 10 cm thick moderator (right).

Rev configurations, containing an "albedo" reflector, merit a more detailed study that employs a more realistic geometry, as described in the next section.

5.2 Advanced geometry analysis

5.2.1 Description of the configurations

Once a general configuration containing a neutron reflector was selected, a more realistic geometry based on it has been developed. In the MC simulations, the detector size has been reduced to a sensitive area of 10×10 cm^2, since larger THGEM electrodes are not presently available; moreover, it has been inserted into a sealed vessel similar to the one used in the experimental set up (see Fig. 5.5). This is a stainless steel vessel with a cylindrical symmetry (internal diameter: 20 cm, internal depth: 9.8 cm) and a circular frontal window. The latter is capped with the moderator.
As far as the design of the real detector is concerned, the decision to employ a boron layer as neutron converter has been taken, because it is easier to handle and commercially available compared to ^{6}Li. In most cases, the kinetic energy of alpha particles emitted by the ^{10}B(n,α)^{7}Li ($\sigma = 3837$ b for 25 meV neutrons [53]) reactions is 1.47 MeV, corresponding to a range in boron of 3.3 μm. This corresponds to the most efficient thickness for a thermal neutron converter; in any case, at present the manufacturer (CASCADE® Detector Technology GmbH) cannot guarantee satisfactory time stability for a ^{10}B layer thicker than 2 μm.
Following the manufacturer's indications, a 10×10 cm^2 ^{10}B layer with a thickness

of 2 μm deposited on a 0.1 mm thick aluminium foil has been considered in the simulations; it is positioned inside the chamber, in contact with a $10 \times 10 \times 3$ cm^3 PE reflector. A gap of 1.5 mm of air is maintained between the Cd foil and the ^{10}B layer, representing the space occupied by the gas detector.
The detector is irradiated with a parallel beam of neutrons emitted by an homoge-

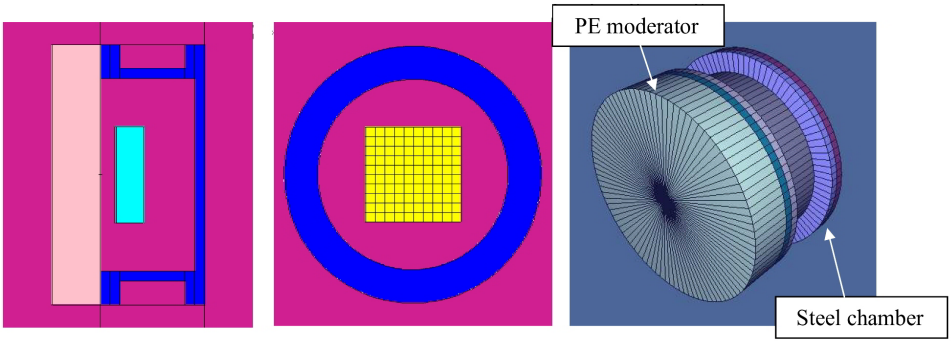

Figure 5.5: Longitudinal and frontal sections of the MC geometry, together with a 3D image; the frontal section is taken at the location of the boron layer (yellow). A 5 cm thick moderator (pink) is depicted in front of the 20 cm inner diameter steel chamber (blue), which contains the boron layer and the reflector.

neous circular source of 32 cm in diameter; the whole frontal area of the chamber is therefore uniformly irradiated. As usual, neutrons at 29 discrete initial energies from 1 meV to 25 MeV have been simulated for the RF calculations.
For a given incoming neutron energy, it is reasonable to expect a non-homogeneous distribution of neutron captures inside the converter layer. Edge-effects and neutron scattering in the chamber walls contribute to modify the neutron spectrum and fluence inside the chamber. In order to evaluate these effects, the ^{10}B layer is divided into 100 square pixels, each with an area of 1 cm^2. In fact, in the preliminary calculations, the total number of boron neutron captures in the 16 central pixels has been calculated, in order to decrease the computing time. In the following analysis, the RFs will be expressed in terms of number of captures inside the converter 4×4 cm^2 central area per unit fluence for a given incoming energy.
Following the analysis described in the previous section, a set up consisting of a pure PE moderator, a Cd foil placed on the chamber window and a reflector was studied; moreover, two configurations without Cd but with a homogeneous PE/B 95/5 moderator were examined. The borated plastic was considered with the same aim of the Cd layer: that is, to absorb moderated neutrons. In brief, the following configurations were investigated:

- Conf1: PE (ρ = 0.93 g/cm^3) moderator in contact with a 1 mm thick Cd

E_n	Moderator thickness	Conf1 FWHM	Conf2 FWHM	Conf3 FWHM
0.5 MeV	3 cm	8 cm	8 cm	8 cm
0.5 MeV	10 cm	9 cm	10 cm	9 cm
5 MeV	3 cm	8 cm	8 cm	7 cm
5 MeV	10 cm	9 cm	10 cm	9 cm

Table 5.3: FWHM obtained for each configuration. Neutron energy (E_n) and moderator thickness are indicated.

layer, and a PE reflector.

- Conf2: PE/B 95/5 (0.95 g/cm^3) moderator (no Cd foil) and a PE reflector.
- Conf3: PE/B 95/5 moderator (no Cd foil) and a PE/B 95/5 reflector.

Similarly to the previous section, for each configuration the RFs and the FHWM were calculated.

5.2.2 Response function calculation

RFs calculated for the three configurations under examination are shown in Fig. 5.6. No significant difference appears between Conf1 and Conf2; the effect of the Cd layer is therefore comparable with the boron doping in the plastic moderator. Considerably different are RFs when boron is also present in the reflector; as expected, an overall loss of efficiency is clearly visible.

5.2.3 Spatial resolution analysis

The results of the spatial resolution analysis, carried out as described in the previous section, are shown in Table 5.3. Generally, the presence of the steel chamber increases the obtained FWHM with respect to the general configurations. The slightly better resolution achieved due to the presence of boron in the reflector (Conf3) does not compensate for the loss of efficiency apparent in the RF analysis. Therefore, Conf1 and Conf2 seem to be the preferable options; due to the availability of borated plastic, the ultimate detector design was based on the Conf2 configuration, that is with a borated plastic moderator, no Cd layer and a pure PE reflector.

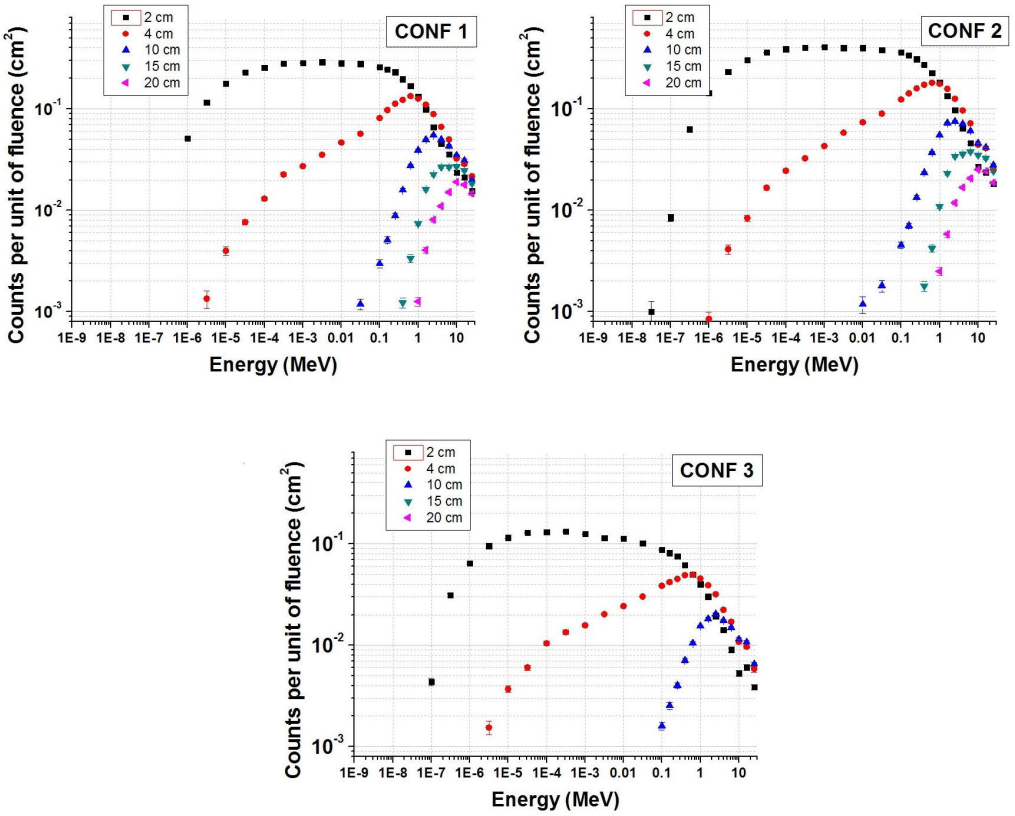

Figure 5.6: RFs of the three configurations described in the 5.2.1 paragraph.

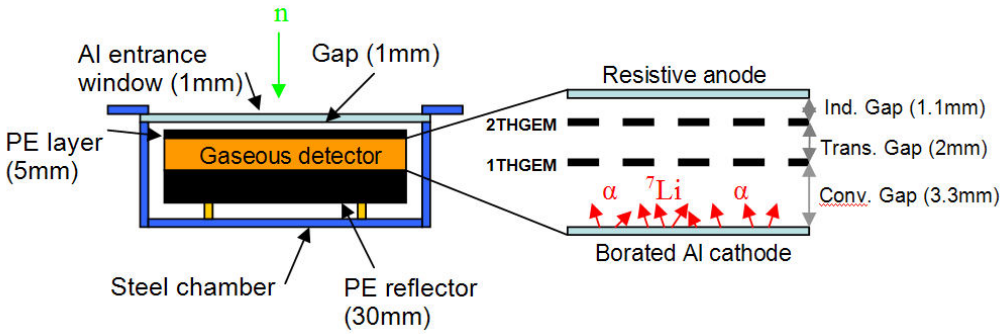

Figure 5.7: Ultimate detector configuration, reproduced in the MC calculations. The gaseous detector is shown in detail.

5.3 Ultimate set up

Starting from the Conf2 configuration, the ultimate MC geometric structure has been developed, containing all the mechanical and electronic details (see

Fig. 5.7). A set of PE/B moderators were designed in order to cap the steel chamber tightly; their design (wall thickness, internal and external shape) and composition (Nickel-chromium steel, grade 304, $\rho = 7.9$ g/cm^3) reproduce accurately the real one. The chamber entrance window is sealed with an aluminium (2.7 g/cm^3) 1 mm thick foil. When the chamber is evacuated, this foil bends appreciably. Therefore, in order to protect the inner parts, a $120 \times 120 \times 5$ mm^3 PE (0.94 g/cm^3) layer has been inserted between the gaseous detector and the window (leaving a 1 mm gap between the window and the PE layer).
The neutron reflector is made of a PE (0.94 g/cm^3) cylinder (h: 30 mm, d: 170 mm). Between the 5 mm thick PE layer and the 30 mm thick PE reflector, the gaseous detector is inserted, taking up 7.4 mm in total. The following sequence of items describes the electrodes reproduced in the MC set up, starting from the delay-line board in contact with 5 mm PE layer.

1) read out delay-line board (0.5 mm thick, made of Garolite G-10, 1.8 g/cm^3)
2) anode (1 mm, G-10, 1.8 g/cm^3)
3) 1 mm empty gap
4) 2THGEM (0.4 mm, G-10, 1.6 g/cm^3)
5) 2 mm empty gap
6) 1THGEM (0.4 mm, G-10, 1.6 g/cm^3)
7) 2 mm empty gap
8) converter layer (2 μm, ^{10}B, 2.3 g/cm^3)
9) aluminium foil (0.1 mm, 2.3 g/cm^3)

The latter is placed in contact with the PE neutron reflector.
With such a geometrical set up, the RFs calculated via the usual method are shown in Fig. 5.8(a). A set of five PE/B moderators has been considered; the thickness of the two thinnest moderators was increased to 4 and 6 cm respectively, in order to reduce the detector sensitivity to epithermal neutrons which, in typical BNCT fields with their high epithermal flux, would dominate the detector response. The five RFs appear nicely peaked and well separated, as can be seen in the fast neutron energy range (Fig. 5.8(b)). Moreover, the 5 mm thick PE layer inserted in the chamber acts as a neutron moderator, as well as the gas detector electrodes, increasing the efficiency for fast neutrons.
As far as spatial resolution is concerned, FWHM values comparable to Conf2 of Table 5.3 have been obtained.

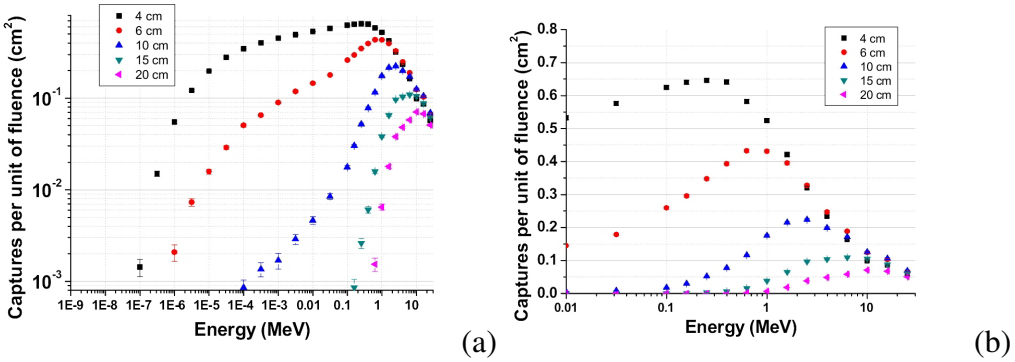

Figure 5.8: RFs of the ultimate set up.

5.4 Unfolding test

By means of the MXD_FC33 deconvolution software (a later version of the MAXED code [56, 57]), an unfolding test was performed utilizing the RFs obtained with the ultimate set up. MXD_FC33 was written specifically for the unfolding of Bonner sphere data, but it can be adapted for use with other types of "few-channel" unfolding. It is based on the maximum entropy method [58]. The described test is an ideal experiment, and was performed to check the feasibility of performing spectrometry with our instrument in the energy range of interest employing the calculated RFs. Several detector irradiations in neutron fields with continuous spectra were simulated. At first the ^{252}Cf fission spectrum was chosen for the test. A simulation was carried out for each moderator, calculating the number of counts, that is the neutron capture events in the central 4×4 cm^2 area of the converter per unit of particles emitted by the source.

In order to perform the unfolding algorithm and achieve an estimation of the neutron spectrum, MXD_FC33 needs, beside the RFs and the number of counts per each moderator, a "default" spectrum, that is a "guessed" spectrum containing the a priori information.

The deconvolution procedure was carried out twice starting from two default spectra, both very different from the ^{252}Cf one. The first default spectrum was selected to be one that appears "flat" when represented per unit of lethargy on a logarithmic x-axis. Subsequently, a spectrum exponentially diverging as function of energy in the same representation was chosen. In both cases the energy intervals considered were between 10 keV and 25 MeV.

In Fig. 5.9 the ^{252}Cf spectrum used to irradiate the detector, the two default spectra and the respective unfolded spectra are shown. In both cases, a very satisfying similarity between the reconstructed spectra and the ^{252}Cf one was obtained, even starting from very dissimilar default spectra.

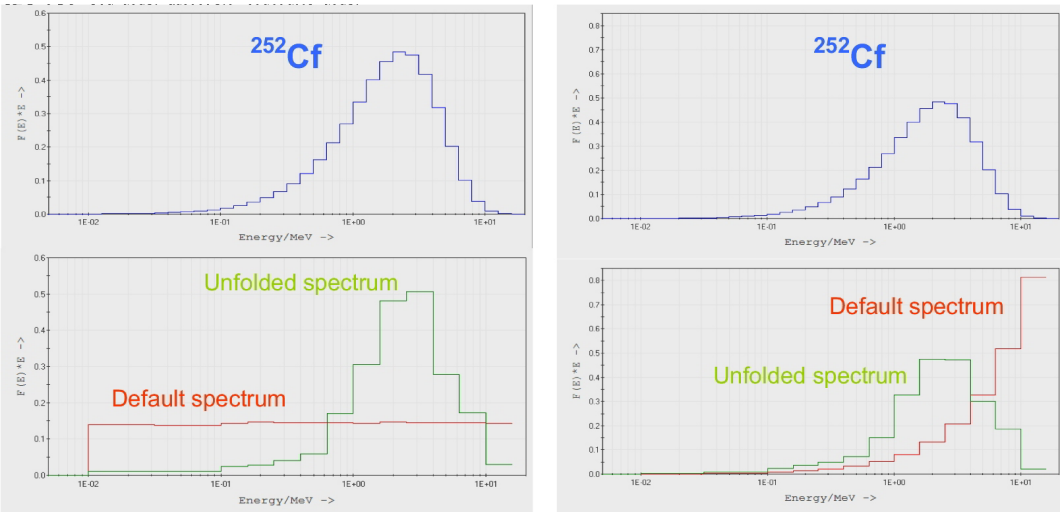

Figure 5.9: In the upper plots, the ^{252}Cf fission spectrum utilized in the MC simulations. The plots below show the energy distributions reconstructed with the MXD_FC33 code, together with the respective default spectra. Energy distributions are expressed in fluence per unit of lethargy (MeV/cm^2).

An analogous test has been performed simulating an irradiation with the neutron beam of the BNCT epithermal column of the NRI (Rez-Prague) [48]. The spectrum utilized in the MC calculations is visible in the upper plot of Fig. 5.10. As default, a flat spectrum from 10^{-2} eV to 25 MeV was selected. The unfolded spectrum adequately reproduces the general shape of the real one. In particular, the intensity of the epithermal region is accurately reproduced, as is also the fast peak around 1 MeV. With respect to the thermal region, the RFs contain no information; hence, the unfolding procedure proposes in this region an energy distribution that is identical to the default spectrum. In any case, this problem affects an energy region that is not of interest in the present project. The described tests demonstrate that the spectrometer design, whose development has been described in this chapter, allows in principle a useful unfolding procedure of a continuous neutron spectrum to be implemented in the epithermal and fast neutron regions.

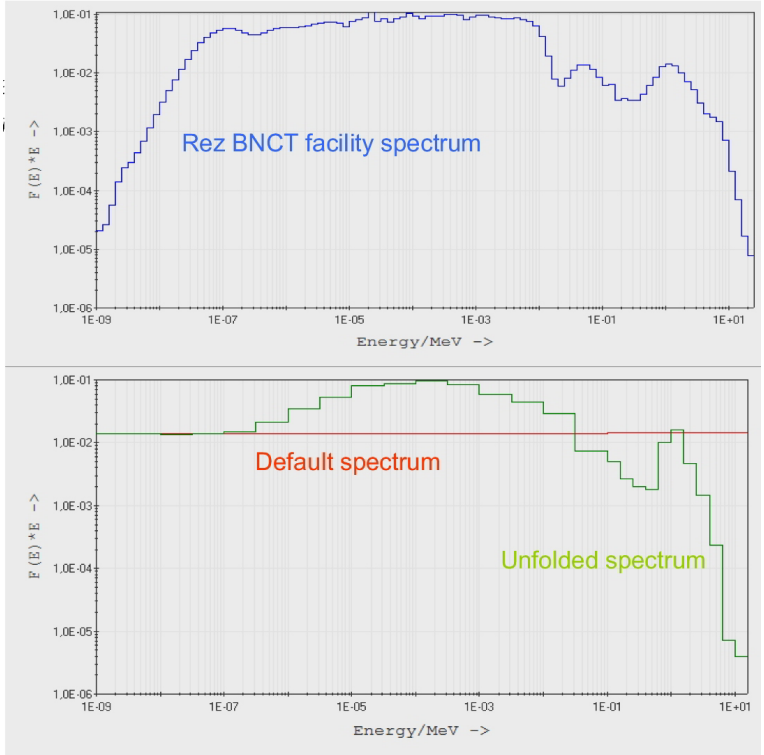

Figure 5.10: The neutron spectrum of the epithermal column of the LVR-15 reactor (above), and the spectrum resulting from the unfolding procedure. Energy distributions are expressed in fluence per unit lethargy (MeV/cm^2).

Chapter 6

Proposal for a novel neutron spectrometer: gaseous detector set up

In this chapter the gaseous detector components are described. First, the detector general set up is depicted, including details of the employed electrodes (Sec. 6.1). Then, the description focusses on the imaging system, in particular on the 2D imaging board and read-out electronic chain (Sec. 6.2). In Sec. 6.3 two methods for effective gain determination are presented. Finally, the three kinds of radiation sources used for the detector development are described (Sec. 6.4).

6.1 General detector set up

The imaging detector is composed of a metallic mesh cathode, two THGEMs in cascade, a resistive anode and a 2D read-out electrode [59]. The detector set up is schematically shown in Fig. 6.1, together with a picture of a THGEM surface.
The detector working principle is as follows: the incoming radiation can interact with the gas in the 10 mm conversion gap, creating free electron-ion pairs. Following the drift electric field (E_{drift}) lines, the free electrons are focussed in the holes of 1THGEM and multiplied. The resulting charge cloud, due to E_{trans}, crosses the 2.1 mm thick transfer gap and is further multiplied in 2THGEM. Finally the ensuing cloud, passing through the induction field (E_{ind}), reaches the resistive anode and is imaged by the 2D read-out electrode, using delay-line encoding.
The two THGEM electrodes are produced by means of standard printed circuit board (PCB) technology. They are made of a 0.4 mm thick FR-4 board, covered on both sizes with 35 μm thick Cu layers. On the 10×10 cm^2 active area 0.5 mm diameter holes are arranged in an hexagonal pattern, with 1 mm of pitch. The rim

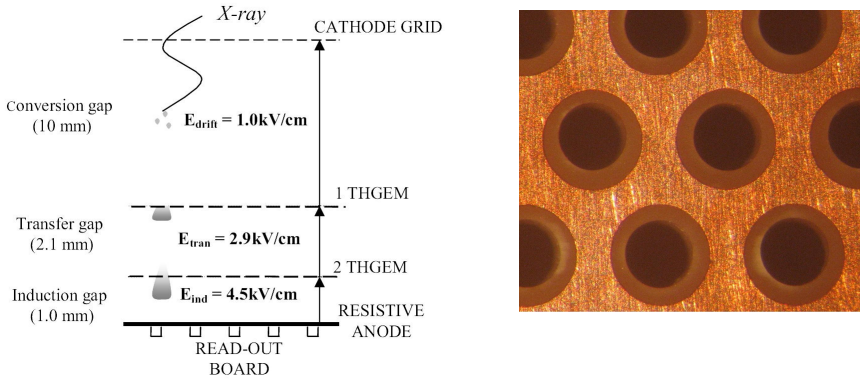

Figure 6.1: Schematic of the detector set up. The usual electric field settings, when the detector is filled with Ar/CH_4, are indicated. On the right, a microscope picture is shown, representing the surface of a THGEM electrode with holes of 0.5 mm of diamater and a pitch of 1 mm.

etched around the holes is 0.1 mm thick.
The resistive anode is composed of a 2 MΩ/□ graphite layer sprayed on a FR-4 substrate, and it is coupled with a double-sided PCB read-out electrode [54, 61, 62]. The charge collected on the resistive anode induces signals on the X-Y strips that are printed on both sides, with a pitch of 2 mm. Such strips connect diamond-shaped pads, and on each side of the board they are coupled to a discrete delay-line circuit (see Fig. 6.2).

The latter is composed of 52 LC cells with an inductance of L = 290 nH and a capacitance of C = 27 pF per cell; the corresponding delay is 1.4 ns/mm; the total delay for each coordinate is thus 140 ns. The avalanche location is derived from the time difference between induced signals propagating along the discrete LC delay-line circuit.
The detector is located within a cylindrical stainless steel chamber whose external diameter is 27 cm, with a 25 μm thick Mylar window of diameter 20 cm glued to the steel by means of epoxy paste (Araldite 2011).
After the detector is assembled, the chamber is sealed, vacuum pumped ($<$ 1 mbar) and then filled with the selected gas at atmospheric pressure. Throughout the measurements, a continuous gas flow is maintained into the vessel via a connection to the laboratory gas system. The steel chamber together with the flow system is shown in Fig. 6.3.

Each electrode of the detector is biased by means of high voltage power supplies (CAEN® model N471A), through a 22 MΩ serial resistor, to limit possible discharge currents. A current limit of 100 nA was usually set on the power supplies biasing the THGEMs, in order to further reduce discharge current and prevent

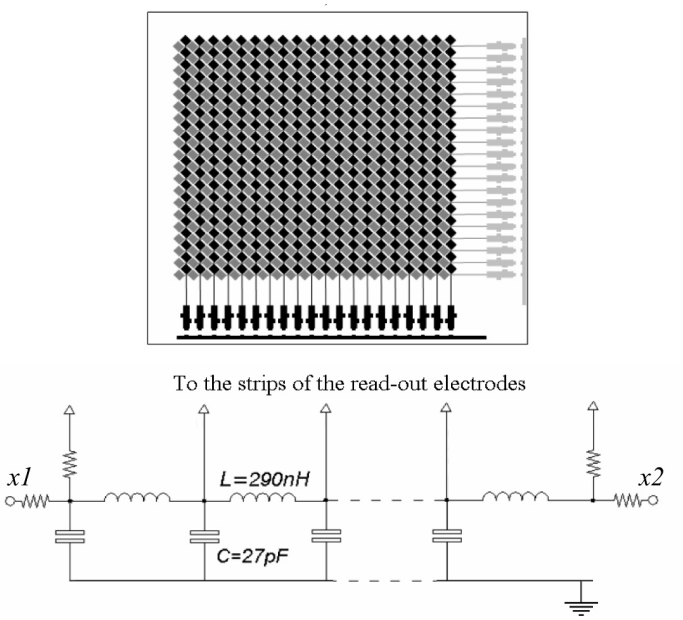

Figure 6.2: Schematic of the read-out board, that has a sensitive area of 10×10 cm^2. A detail of the delay circuit connected to the parallel strips is also depicted [59].

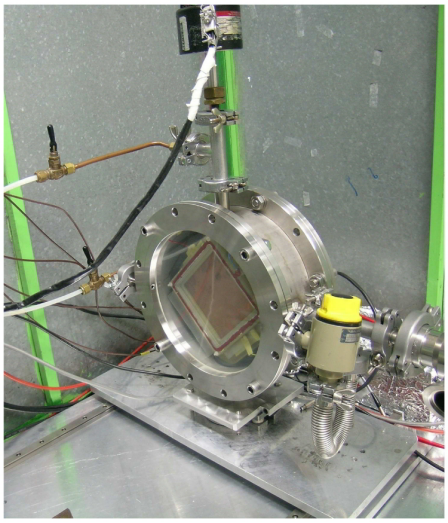

Figure 6.3: The cylindrical steel chamber containing the detector. The frontal Mylar window (diameter = 20 cm) is visible, together with the gas inlet and outlet.

electronic device damage. When the detector was filled with Ar/CH_4, the high voltage values were typically set such that the E_{conv}, E_{drift} and E_{ind} electric fields were at 1, 2.9 and 4.5 kV/cm respectively.
The signal from the electrode on the second THGEM top was either fed to a charge sensitive preamplifier (ORTEC® model 109, with sensitivity 100 mV/pC) or a fast preamplifier (VV44, MPI Heidelberg), providing either integrated charge signal for absolute gain measurements or a fast common trigger for position measurements.

6.2 Imaging system description

The imaging system is based on a delay-line board that is read out by a Time to Digital Converter (TDC) (an HPTDC8 PCI card by RoentDek®), having at maximum resolution an input bin size of 25 ps. The general scheme of the data acquisition (DAQ) system is shown in Fig. 6.4. A trigger signal occurring for each

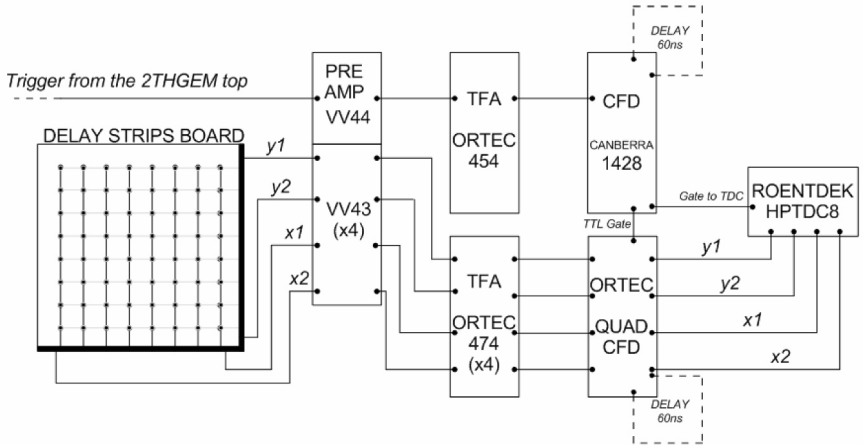

Figure 6.4: DAQ scheme. The TFAs and the CFDs are installed in a NIM crate, while the TDC is a PCI card installed in a PC.

gas avalanche in 2THGEM is used as a common start for the TDC, that measures the arrival times of the NIM pulses generated by the four delay-line signals ($x1$, $x2$, $y1$, $y2$). A proper data acquisition software (CoboldPC 2002 by RoentDek®) provides the data storage and a preliminary analysis of the signal arrival times.
The trigger signal is taken from the top surface of the second THGEM; when an avalanche occurs in this THGEM, the ions drifting towards the first one induce a certain amount of charge on its surface. The induced current is fed in a fast current sensitive preamplifier (VV44, MPI Heidelberg); the pre-amp output is shaped and

amplified by a Timing Filter Amplifier (TFA) 454 by EG&G Ortec® and discriminated by a Constant Fraction Discriminator (CFD) Canberra 1428. The delay time of this CFD is set to 60ns with an appropriate circuit. The CFD emits from the frontal panel a digital pulse employed as a common start by the TDC and from the rear side a TTL signal which enables the gate for the discriminators of the delay-lines.
Each signal coming from the four delay-line ends is collected by a fast preamplifier (VV43, MPI Heidelberg) and fed in a TFA EG&G Ortec 474. The four amplified signals are then independently discriminated by an EG&G Ortec Quad Constant-Fraction 100 MHz Discriminator (delay time: 60 ns). This discriminator, gated by the TTL pulse generated by the trigger line, produces four NIM signals that are fed in the TDC. All the TFAs and CFDs are installed in a NIM crate.
Therefore, when an avalanche occurs in the second THGEM, the electronic chain generates a trigger signal that starts four independent time measurements by the TDC; this device measures the arrival time of the four NIM pulses (two for each spatial coordinate) and the CoboldPC software registers on the PC the corresponding four digits for each event. The software can also perform data analysis; in our case, a routine was developed in order to display the following ten histograms:

- event distributions of the four time signals ($x1$, $x2$, $y1$, $y2$)
- single coordinate spatial distributions ($posx = x1 - x2$, $posy = y1 - y2$)
- single coordinate sums ($sumx = x1 + x2$, $sumy = y1 + y2$)
- bidimensional event distribution (*posx* and *posy* on the x and y axis, respectively)
- as the previous one, but with some custom constraints on *sumx* and *sumy*.

Each histogram can be saved as a plot file or an ASCII file.

6.3 Gain measurement techniques

In order to measure the detector gain, two different methods have been applied, that are denoted pulse and current modes.

6.3.1 Pulse mode

The first method is based on the measurement of the charge induced on the top of the second THGEM by the charge avalanche traversing the electrode. The

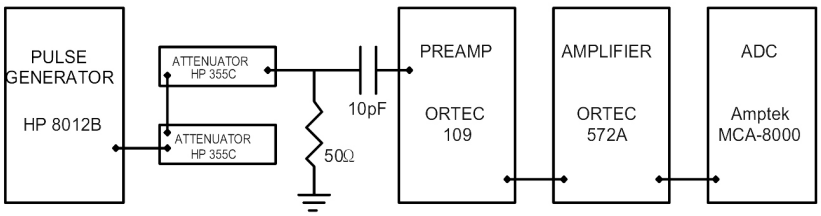

Figure 6.5: Set up for the electronic chain calibration.

absolute value of the induced charge is estimated from the calibration of the electronic chain.
The charge induced on the 2THGEM top surface is measured connecting this electrode with a DAQ composed of a charge sensitive pre-amplifier (Ortec Preamplifier Model 109), a linear amplifier (Ortec 572A) and an analog to digital (ADC) device (Amptek MCA-8000, with 2048 channels) connected to the computer.
Initially, the electronic chain is calibrated using a small capacitor (10 pF) to inject a test charge into the charge sensitive preamplifier input (Fig. 6.5). The unit responds to the negative-going edge of the test pulse (square wave with low frequency of around 100 Hz and width of 1 ms), which has a transition time of less than 20 ns. This negative-going edge is followed by a relatively flat part of the waveform so that it appears as a step function. Charge transfer to the input is according to $Q = C \cdot V$, where $Q =$ total charge, $C =$ value of test capacitor, and $V =$ amplitude of voltage step. Thus, for a given pulse amplitude, the amount of charge injected in the electronic chain is known, and the ratio between electrons and ADC can be measured.
Considering the W factor of the gas and irradiating the detector with a monochromatic photon source (such as a ^{55}Fe source), the number of free electrons released by the incoming radiation in the conversion gap is known. The ratio between ionization charge and charge induced on the second electrode is henceforth referred to as “effective gain”.

6.3.2 Current mode

A different method to the one described in the previous paragraph is based on the measurement of current intensity on several electrodes. The detector must be irradiated with an intense radiation source (for example, an X-ray rube). At first, just a reversed E_{drift} is applied, with a cathode mesh connected to a galvanometer. The measured current, referred to as normalization current, is due to the ionization electrons created by the radiation in the conversion gap. Subse-

quently, maintaining the same radiation intensity, the electrodes are connected as shown in Fig. 6.6, with the 2THGEM bottom connected together with the anode to the galvanometer. At this point, the ΔV_{THGEM} (that is the bias across the two THGEM surfaces) is increased step by step, and the ratio between the measured current and the normalization current determines the "effective gain".

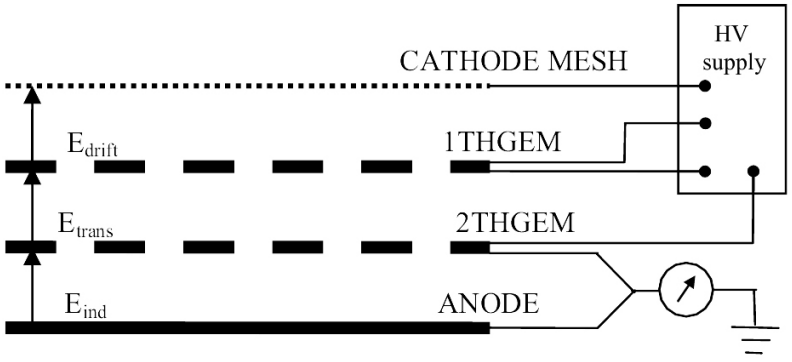

Figure 6.6: Experimental set up used for the effective gain measurement in current mode.

6.4 Radiation sources

During the development stage, the gaseous detector was irradiated using three types of radiation sources. For radioprotection purposes, the chamber was inserted in a shielding metal box of dimensions $150 \times 60 \times 100$ cm^3. The detector and the source may be positioned at different relative distances (maximum: 120 cm).
A ^{55}Fe 5.9 keV photon source was employed; if necessary, a 1 mm diameter collimator can be attached to it. It was usually positioned outside the chamber, close to the Mylar window.
Moreover, an Apogee X-ray tube by Oxford Instruments® with a Cu target was employed, at a maximum anode voltage of 50 kV and current of 1.0 mA. The tube emits a bremsstrahlung spectrum filtered at low energies. When sufficient high voltage is applied on the anode, the Cu K_α fluorescence line is populated, and a considerable number of photons is emitted at the corresponding energy (8.979 keV).
Finally, an encapsulated ^{241}Am source was used. It emits α particles at around 4.5 MeV, together with 60 keV photons (36% of relative intensity) [63]. Because of the low range of the emitted α particles, the source was positioned inside the

chamber, 1 cm before the anode grid, with a collimator of 1 mm in diameter positioned at 0.7 cm distance from the source, as shown in Fig. 6.7.

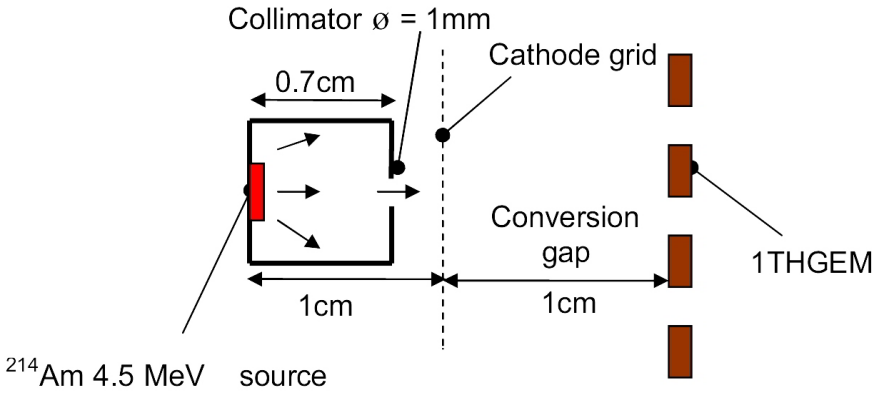

Figure 6.7: Scheme of the ^{241}Am source positioned inside the chamber.

Chapter 7

Development of the gaseous detector with Ar/CH_4 filling

In this thesis work, a gaseous detector based on double THGEMs and a 2D imaging board was coupled to a neutron-to-charged-particle converter. Such a converter is sensitive mainly to neutrons that have been previously slowed down in the moderator, losing in such a way their initial direction. In fact, the MC simulations described in Chapter 5 foresee spatial resolution of the order of several centimeters. Therefore, as far as the gaseous imaging detector is concerned, there is no need for submillimetric resolution.
Anyway, during the experimental development, the gaseous imaging detector was considered by itself, attempting to find the electronics and mechanical settings capable of achieving optimal imaging performance. Such an imaging detector could indeed eventually be employed for a variety of purposes in the field of ionizing radiation detection.
This chapter summarizes the principal results achieved in the course of developing the gaseous detector filled with Ar/CH_4 95/5 at 1 atm. A continuous gas flow (80 cm^3/min) was maintained into the vessel during the measurements by a connection to the laboratory gas system. The detector effective-gain as function of ΔV_{THGEM} was measured in pulse mode, and the dependence of the energy resolution on drift was studied (Sec. 7.1). The imaging performance was investigated, in particular with respect to the dependence of spatial resolution on the gain (Sec. 7.2). Since in the ultimate configuration the gaseous detector was coupled to a high LET particles emitter, several tests with a ^{241}Am α source were carried out at an appropriately low gain (Sec. 7.3). Finally, with the same radiation source, the detector gain stability was investigated (Sec. 7.4).

Ampl. shaping time	Ampl. gain	Electrons/ADC
0.5 μs	$\times$20	$2.3 \cdot 10^3$
0.5 μs	$\times$50	$9.7 \cdot 10^2$
0.5 μs	$\times$100	$5.0 \cdot 10^2$

Table 7.1: Calibration of the electronic chain for pulse-height gain measurements

7.1 Effective gain and energy resolution

The detector effective gain has been evaluated in pulse mode (see Sec. 6.3.1). Initially, the electrons/ADC ratio was measured with the electronic set up shown in Fig. 6.5. Results obtained for different amplifier settings are shown in Table 7.1. Once the correspondence between ADC channels and number of electrons collected on the 2THGEM top was established, it was possible to perform pulse-mode gain measurements as function of the ΔV_{THGEM} irradiating the detector with the ^{55}Fe source.
Several gain scans were carried out increasing the ΔV_{THGEM} and until the onset of discharge (that is, when the THGEMs sparked three or four times per minute). The measurement shown in Fig. 7.1 shows that the detector attains a maximum effective-gain of around $8.5 \cdot 10^3$ at a ΔV_{THGEM} of 1160 V. The obtained gain, achieved with the detector under unstable conditions (several sparks per minute) was not satisfactory, particularly when compared to gains higher than 10^4 at ΔV_{THGEM} = 1100 V obtained by Cortesi et al. [59] with an analogous experimental set up. The dissimilar performance can be explained assuming different manufacturing quality of the electrodes; in the case described in [59], a couple of THGEM electrodes was employed, that were no longer available at the time of the test described here. A resolution of 20% has been obtained, that is comparable with values obtained with ordinary GEMs [64].
It is known that energy resolution depends strongly on E_{drift}, as shown in Fig. 7.2(a). If no drift field is present in the conversion gap, the ion-electron recombination probability is high, and only the free electrons that are released in the region close to the first THGEM are collected into the holes; moreover, as the drift field in the conversion gap increases, more and more electrons are focused into the holes, such that the measured gain also increases (see Fig. 7.2(b)). At around a Edrift of 1 kV/cm, all ionization electrons produced by the radiation are focused in the THGEM holes and multiplied by the avalanche processes, such that the detector attains its maximum gain value and its best energy resolution.

The collected charge is quite stable as function of E_{drift} in the region from 1 kV/cm to 2 kV/cm. Above this value, a reduction of the collected charge is detected, that is due to a defocusing effect [65]: the electrons are over-accelerated by the high drift field and they are not efficiently focused into the THGEM holes, but

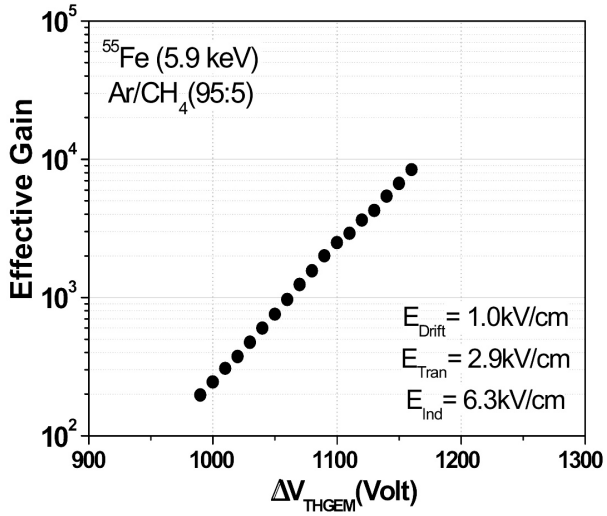

Figure 7.1: Pulse-mode gain scan perforemed in Ar/CH_4 with a 5.9 keV photon source.

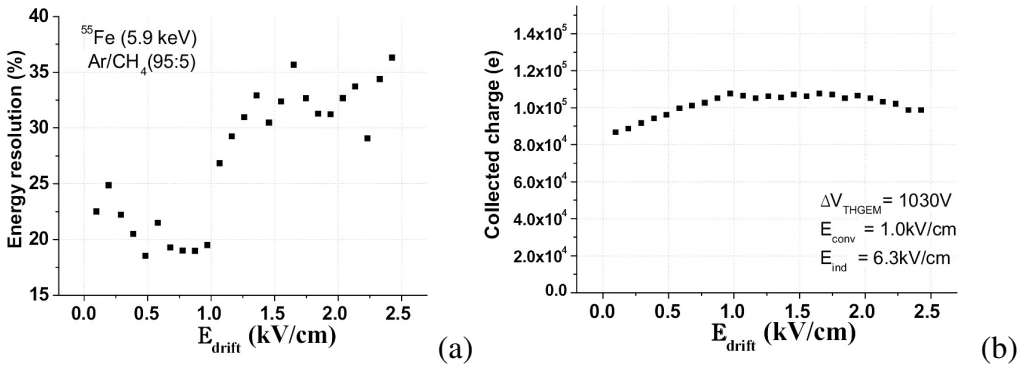

Figure 7.2: (a) Energy resolution expressed as the ratio between standard deviation and mean value of the ^{55}Fe peak versus Edrif. (b) Total charge collected on the top of the second THGEM. In this plot, 10^5 electrons correspond to a gain of around 440.

are collected on the electrode top metal face. For the same reason, an excessively high drift field degrades the energy resolution. From the two plots in Fig. 7.2 it appears that setting $E_{drift} = 1$ kV/cm assures complete charge collection with an energy resolution around 20% at 5.9 keV.

7.2 Imaging properties

An intensive effort was carried out in order to test and improve the detector imaging performance. The image homogeneity and the spatial resolution were investigated. The obtained results were, however, unsatisfactory; in particular, a distortion in the signal emitted by the delay-line board was detected, causing pronounced parallel lines in the empty field (that is obtained with the detector area fully irradiated) image.
Despite the unsatisfying homogeneity of the empty field, a study of the spatial resolution was performed. At first, the relation between TDC data (ns) and space was determined, shielding the detector window with a pierced metal mask; measuring the relative distances between the holes on the mask and considering the distribution of spots in the acquired image, a ratio of 0.0765 mm/ns was estimated.
The spatial resolution of the imaging system was measured evaluating the FWHM of the point spread function (PSF); the latter was derived by means of the edge spread function (ESF) technique [59, 66]. The detector window was partially shielded with a 2 mm thick aluminium layer and irradiated with the X-ray tube (voltage: 12.5 kV, current: 0.15 mA). From the obtained image, the projection of the edge profile was extracted and fitted with the following empirical model function:

$$ESF(x) = a_0 + \frac{a_1}{1+\exp(-a_2(x-a_3))} \tag{7.1}$$

where a_0 is related to the transmission of the Al layer, a1 is the brightness of the full irradiated sensitive area, a_2 is the steepness of the edge function (related to the spatial resolution of the imaging system) and finally a_3 is the centroid of the edge function. Differentiating the empirical model of the ESF, it is possible to obtain the FWHM of the PSF, which is given by:

$$FHWM = \frac{3.53}{a_2} \tag{7.2}$$

The steeper the ESF, the narrower the PSF. Fig. 7.3 shows a grey-scale image of the layer edge, and the fit of its projection along the x-axis.

Fig. 7.4 shows the trend of the FWHM along the x direction as function of ΔV_{THGEM}.
The spatial resolution improves at higher gain and, with ΔV_{THGEM} set at 1170 V, it reaches 1.67 ± 0.05 mm. The higher the gain, in fact, the better the S/N ratio.
During this investigation, it was not possible to further increase the bias on THGEM electrodes under stable conditions. However, with an analogous detector [59], but with other electrodes, significantly better resolution was indeed achieved (0.67 ± 0.02 mm). Thus, the imaging inhomogeneity and the unsatisfactory gain were the two main factors affecting the spatial resolution of the present imaging system.

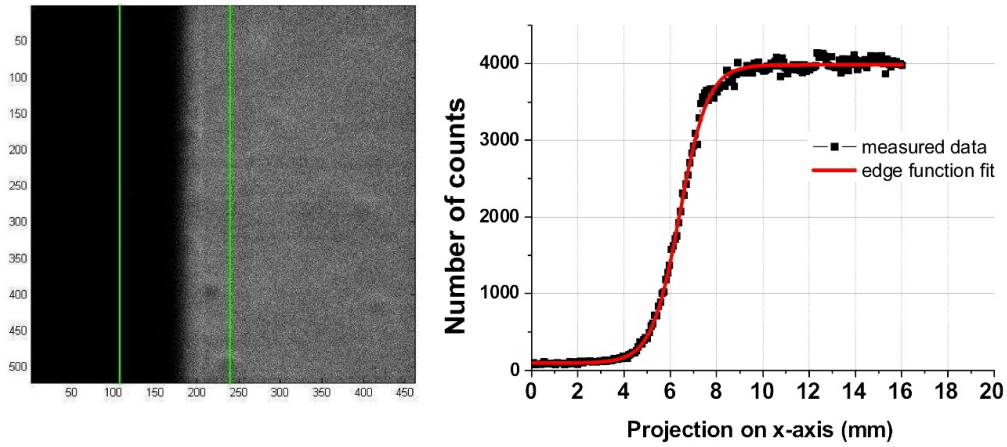

Figure 7.3: Image of the layer edge, and the projection along the x-axis of the area between the green lines is fitted with a suitable edge function.

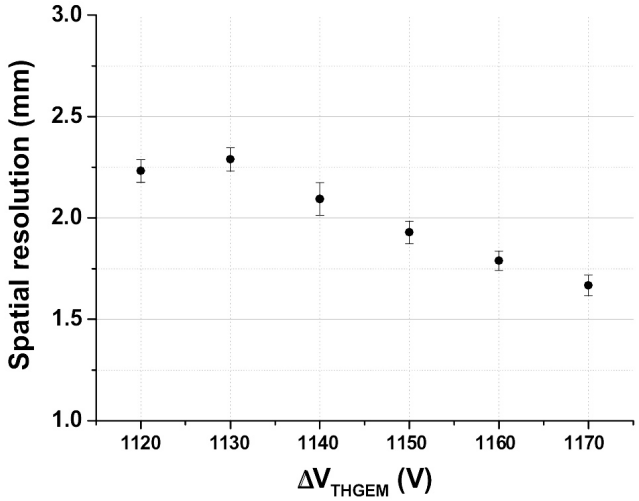

Figure 7.4: FWHM of the PSF as function of the ΔV_{THGEM}.

In order to improve the imaging performance of the THGEM-based detector in term of effective gain, an investigation with a neon-based detector filling was planned, the successful results of which will be described in the next chapter. Preliminary results, indeed, showed that Ne/CH_4 could provide high effective gain at a lower operational voltage than Ar/CH_4.

7.3 Measurements with an α source

Several tests were performed with the ^{241}Am α source in order to investigate the detector response when it is irradiated with heavy charged particles. In the final configuration, in fact, the neutron spectrometer was provided with a neutron-to-charged-particles converter, that emits high LET particles crossing the conversion gap. Moreover, during operation in a BNCT epithermal neutron beam, the gaseous detector will be irradiated with various radiation components (heavy charge particles, photons, recoil protons from hydrogenous materials); it is therefore important to determine in which gain intervals it is sensitive to radiation components having different LET.
Initially, the 4.5 MeV α source was inserted in the chamber; then, a scan of the total collected charge as function of ΔV_{THGEM} was carried out.
The plot in Fig. 7.5 shows the result; the lowest ΔV_{THGEM} value that allows to detect α particles is 880 V, while the maximum value is 1020 V. At this voltage, corresponding to a collected charge of $3.8 \cdot 10^6$ electrons per event at a rate of 5 kHz, the detector was almost fully stable, while at 1030 V it sparked continuously.

When this scan was completed, the α source was removed from the sensitive

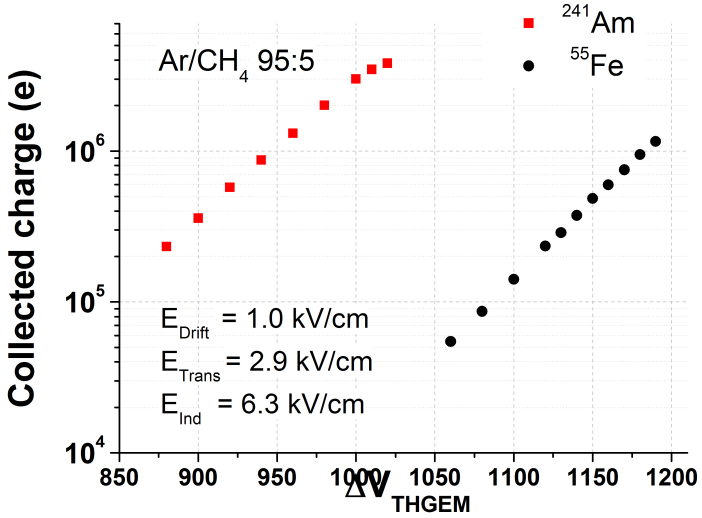

Figure 7.5: Comparison between the charge collection scans performed with 4.5 MeV α particles (^{241}Am) and 5.9 keV photons (^{55}Fe).

area without opening the chamber, and the ^{55}Fe source was instead positioned in front of the detector window, acquiring the scan shown in Fig. 7.5 as well. It is

remarkable that, because of the different LET, there is no ΔV_{THGEM} value that allows to detect simultaneously the 5.9 keV photons and the α particles. The lowest voltage allowing 5.9 keV photon detection is 1060 V, corresponding to a gain of ~ 250; extrapolating to lower voltages the gain curve obtained with the ^{55}Fe source, a gain of ~ 90 is estimable for ΔV_{THGEM} = 1020 V. The α particles release in the conversion gap such an amount of free charges that the detector sparks above ΔV_{THGEM} = 1020 V, and at this voltage the gain is so low that the ^{55}Fe peak is not visible.
It is interesting to note how different is the onset of sparks increasing the THGEM bias, irradiating the detector with the two sources. As above-mentioned, the sparking threshold with the α source is abrupt at 1020 V; on the other hand, when irradiated with the 5.9 keV photons, the detector starts to spark at around 1150 V, and the sparking rate increases progressively with the raising voltage. The high amount of collected charge (some 10^6 electrons) achieved with the ^{241}Am source, suggests that the avalanche process reaches the Raether limit; conversely, the gradual onset of sparks in the ^{55}Fe case may be due to mechanical defects of THGEM electrodes, causing more frequent sparks as function of the increasing applied voltage.

7.4 Stability

It is known that radiation detectors based on hole-type electron multipliers are affected by conditioning effects causing gain variation in time (long-term gain stability). The reasons for these effects are diverse; they may be caused by polarization of the insulator material forming the inner part of the electrodes (FR-4 in the case of THGEM), and also by accumulation of charges on the dielectric surfaces exposed to the avalanche processes.
Several tests have been performed in order to measure and characterize the long-term gain stability of the THGEM-based detector. The measurements were performed irradiating the detector with a collimated ^{241}Am α source (d = 1 mm), located at 1 cm from the conversion gap (counting rate: $\sim$kHz).
The tests were carried out following the hypothesis that, after the bias on electrodes is turned on, the detector gain changes exponentially with time, tending to an asymptotic value; the characteristic time of the exponential is dependent on ΔV_{THGEM}. The goal of this test was to verify this exponential behaviour and to measure the characteristic time (or "conditioning time") for different ΔV_{THGEM} values under identical radiation intensity conditions. Such a characterization has been carried out just from an heuristic point of view, and no hypothesis are guessed concerning the causes of the observed behaviour.
Before starting each measurement, the detector had been sealed (with the gas

ΔV_{THGEM}	τ(min)
960 V	54 ± 16
990 V	46 ± 17
1020 V	26 ± 11

Table 7.2: Weighted mean of τ obtained at different ΔV_{THGEM} values.

flushing) for several days, and all the power supplies had been turned off for at least 12 hours. At time zero, the detector electrodes were biased and the collected charge was recorded with the MCA, from time to time. At a given point, the power suppliers were turned off for 30 minutes and the scan repeated.
Three tests were carried out on three different days, with ΔV_{THGEM} set at 960 V, 990 V and 1020 V respectively; the collected charge versus time is shown in Fig. 7.6. An almost two-fold variation in gain can be seen from the first data point to the last one of each measurement set.
Each scan set was fitted with an exponential function ($y = A \cdot \exp(-t/\tau) + y_0$), and the respective τ values are reported in the plots. The first point of each scan was not considered in the fit, since these points are in the steepest part of the curves, and during the acquisition time (30 s) they were visibly shifted.
During the test performed at ΔV_{THGEM} = 1020 V, the detector sparked approximately once every 10 min. After each spark, the gain suddenly decreased and then started to increase again. The gain shift seems to fit well with the exponential curves; the weighted mean of τ for each ΔV_{THGEM} was calculated and quoted in Table 7.2.
Despite the rather large errors, the measured τ values can be seen as useful order-of-magnitude estimations of how long it is necessary to wait before starting a measurement with an acceptable stability. It is useful to remark that in this case, a two-fold gain variation was detected in several tens of minutes, if the gas had been flushing for a number of days. Single-electron measurements performed immediately after pumping and gas introduction showed 4-fold variations [68]. Anyway, the interpretation of the measured data needs further studies.

7.5 Summary

The gaseous detector, based on double THGEM in cascade and on a 10×10 cm^2 delay-line board, was filled with Ar/CH_4. Irradiating the detector with 5.9 keV photons, a maximum effective-gain of $8.5 \cdot 10^3$ was achieved, with an energy resolution of 20% (FHWM).
The imaging quality was unsatisfactory (in particular, the inhomogeneities of the empty field were very pronounced). A problem in the delay-line board was de-

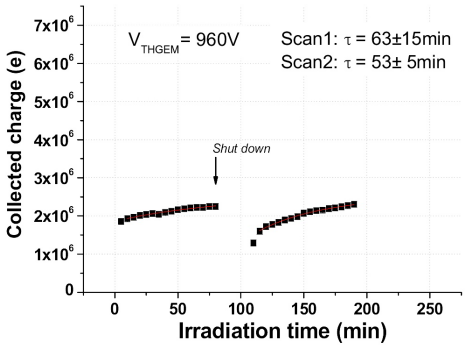

(a)

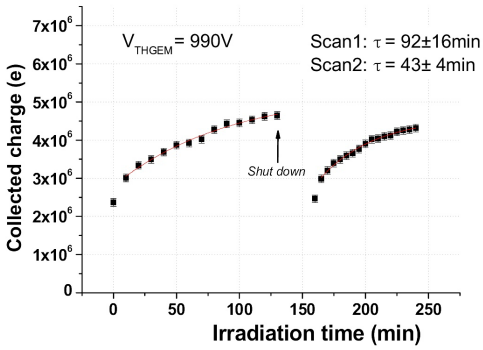

(b)

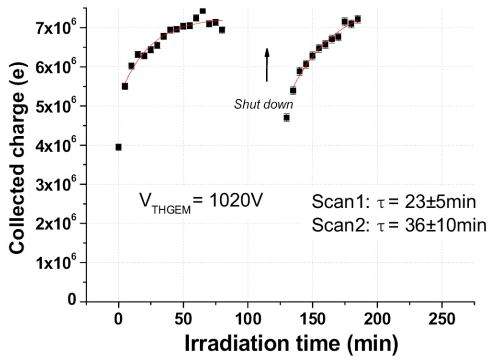

(c)

Figure 7.6: Three stability tests performed with the ^{241}Am alpha source. In each case, the electrodes power supplies were shut down and the scan was repeated after 30 min.

tected, requiring a new device. This problem, together with the insufficiently high gain obtained, caused a quite poor spatial resolution (1.7 mm).
The detector capability to detect heavy charged particles was demonstrated by applying appropriate bias on the THGEM electrodes. Alpha particles from a ^{241}Am source are reliably detectable setting a gain lower than 100, giving rise to energy

spectra whose general trend is reproduced by MC calculations.
As far as the sensitivity to photons at such a low gain is concerned, the detector is not able to see the ^{55}Fe 5.9 keV photons; in contrast, the transparency of the detector to ^{241}Am 60 keV photons has been proved at any gain. Finally, studying the long-time gain stability, a conditioning time for three values of ΔV_{THGEM} has been estimated. When the electrodes are biased, the detector gain increases, reaching a plateau (typically 2-fold higher than the starting point) with a characteristic time which, in the slowest case, is around 1 h.

Chapter 8

Development of the gaseous detector with Ne/CH_4 filling

Charge multiplication occurs at lower operational voltages in gaseous detector filled with Ne mixtures, compared to traditional Ar plus quencher mixtures. Indeed, because of the high first Townsend coefficient of Ne, the avalanche process takes place at lower electric field strength, and for a given THGEM voltage, it is possible to achieve higher gain than in heavier noble gases.
Such a characteristic gives rise to important advantages: operating the THGEM electrodes with lower voltage decreases the risk of discharge due to electrode manufacturing imperfections or to highly ionizing events. Moreover, in case of discharge, the spark energy, which is proportional to the square of the voltage difference applied across the electron multiplier, is moderated.
The detector general set up was the same as used in the experiments described in the previous chapter. However, both the THGEM electrodes and the delay-line board were substituted with new ones of identical design. The detector was filled with Ne plus varying percentages of CH_4 (at 1 atm) by means of two MKS 1179A Mass-Flo® mass flow spectrometers driven by a MKS Type 247 readout system. For each new mixture, after detector pumping, a total gas flow was usually kept at 30 cm^3/min. At first, effective-gain versus ΔV_{THGEM} scans were performed with five different Ne/CH_4 mixtures (Sec. 8.1). Subsequently, a detailed investigation of signal timing as function of methane concentration and drift field was carried out (Sec. 8.2). In the next stage, imaging capabilities of the detector were investigated, such as electronic noise (Sec. 8.3), gain homogeneity (Sec. 8.4) and spatial resolution (Sec. 8.5); moreover, the signal pulse-shape along the DAQ chain was sampled (Sec. 8.6).
Finally, the detector was irradiated with the ^{241}Am α source (Sec. 8.7), setting a suitable gain for detecting highly ionizing particles without sparking.

8.1 Gain measurements

Current-mode gain scans were performed with several Ne/CH_4 mixtures, irradiating the detector with 9 keV X-rays generated by the Roentgen tube. Each gain scan was carried out increasing ΔV_{THGEM} until the onset of sparks; every point shown in Fig. 8.1 was taken with excellent detector stability.
In the pure Ne case, a very steep gain curve reaches its maximum at around 10^6 at ΔV_{THGEM} = 320 V. For a given bias on the electrodes, adding a few percent of methane causes a drastic gain drop; in other words, the presence of methane shifts the gain curves to the right. This effect suggests that the first Townsend coefficient decreases as function of CH_4 concentration.

A loss of maximum achievable gain of around one order of magnitude was

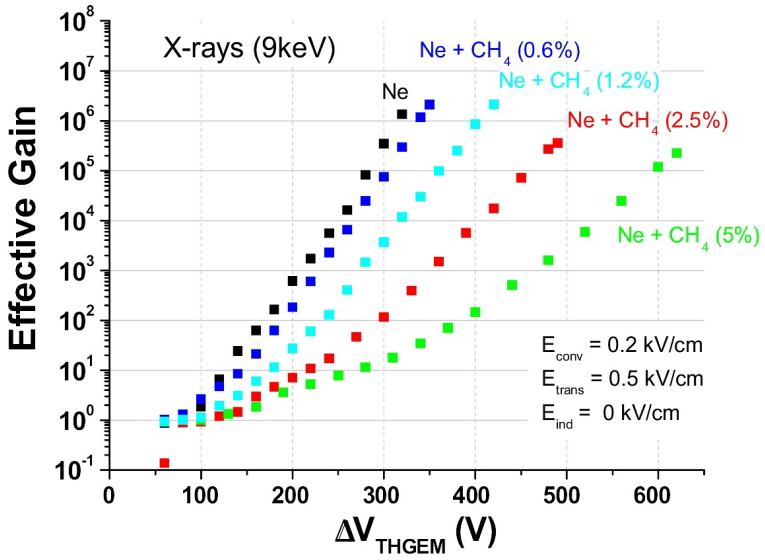

Figure 8.1: Effective-gain curves obtained in current-mode for several Ne/CH_4 mixtures.

detected, going from 0 to 5% of CH_4 concentration; nevertheless, even in the Ne/CH_4 95/5 case the achievable gain ($2 \cdot 10^5$) is noticeably higher than with the Ar/CH_4 95/5 mixture. An higher effective-gain assures a better signal to noise ratio, which in turn could improve the spatial resolution of the imaging system.
No attempts were made to measure gain curves with higher methane concentrations; this in fact would required appreciably higher operational voltages, thus losing the principal advantage of working with Ne based mixtures.

8.2 Pulse-shape analysis

The imaging performance depends strictly on signal pulse-shape. For example, a faster signal induced on the delay-lines allows a better charge localization by the TDC-based imaging system. The rise time of the induction signal depends on the spread of the electron cloud along the drift direction and on the electron drift velocity.
An investigation of the signal pulse-shape has been carried out; in particular, the signal obtained from the second THGEM top was studied, studying its dependence on the electric field along the 10.1 mm conversion gap for various methane concentrations. The signal was processed by a low-noise fast preamplifier (VV44, MPI Heidelberg; rise time: 16 ns) and a shaping amplifier (Ortec 570; gain: 300, differentiation time: 500 ns; no integration); finally, it was acquired and analyzed by a Tektronix® TDS5104B digital oscilloscope. Since the signal is a negative pulse, its fall time (i.e. between 10% and 90% of the negative amplitude) has been measured, as well as the area under the pulse.
Plots in Fig. 8.2 show the obtained results in Ne plus 0%, 1.2% and 2.5% of CH_4. In each case, the E_{trans} was set at 0.5 kV/cm while E_{ind} at 0.6 kV/cm. The voltage across the multiplier electrodes was set in order to achieve effective gains around 10^5: 350 V, 400 V and 600 V, respectively. The detector was irradiated with 9 keV photons from the X-ray generator.

All the scans were performed increasing E_{drift} between 0 and 1 kV/cm, except in the pure Ne case, where the detector sparked for E_{drift} above 0.5 kV/cm. In general, it can be noticed that the higher the methane concentration, the faster the signal fall time; this effect is directly related to the increasing electron drift velocity in Ne mixtures as function of quencher concentration [69, 70]. Moreover, the signal fall time has a minimum around 0.2 kV/cm, that is in the region where the electron drift velocity as a function of the electric field exhibits a maximum in Ne plus methane mixtures [69].
As far as the signal area is concerned, the results can be interpreted considering the dependency on E_{drift} of electron focusing in the THGEM holes, as discussed in Sect. 7.1. For a given E_{drift}, indeed, there exists an optimal ratio between E_{drift} and the electric field in the holes which assures the maximum electron transfer efficiency. In the first case, with ΔV_{THGEM} = 300 V, the E_{drift} value which provides the best focusing efficiency is around 0.2 kV/cm, while in the second case, with ΔV_{THGEM} = 400 V, is around 0.4 kV/cm. When ΔV_{THGEM} is set at 600 V, as in the third case, increasing E_{drift} until 1 kV/cm causes a better electron collection in the holes, as is visible from the asymptotic trend of the signal area. It is reasonable to expect that the maximum value of signal area would be reached when extending the scan to values of $E_{drift} > 1.0$ kV/cm.
In the following measurements, E_{drift} was set at 0.2 kV/cm for each Ne/CH_4 mix-

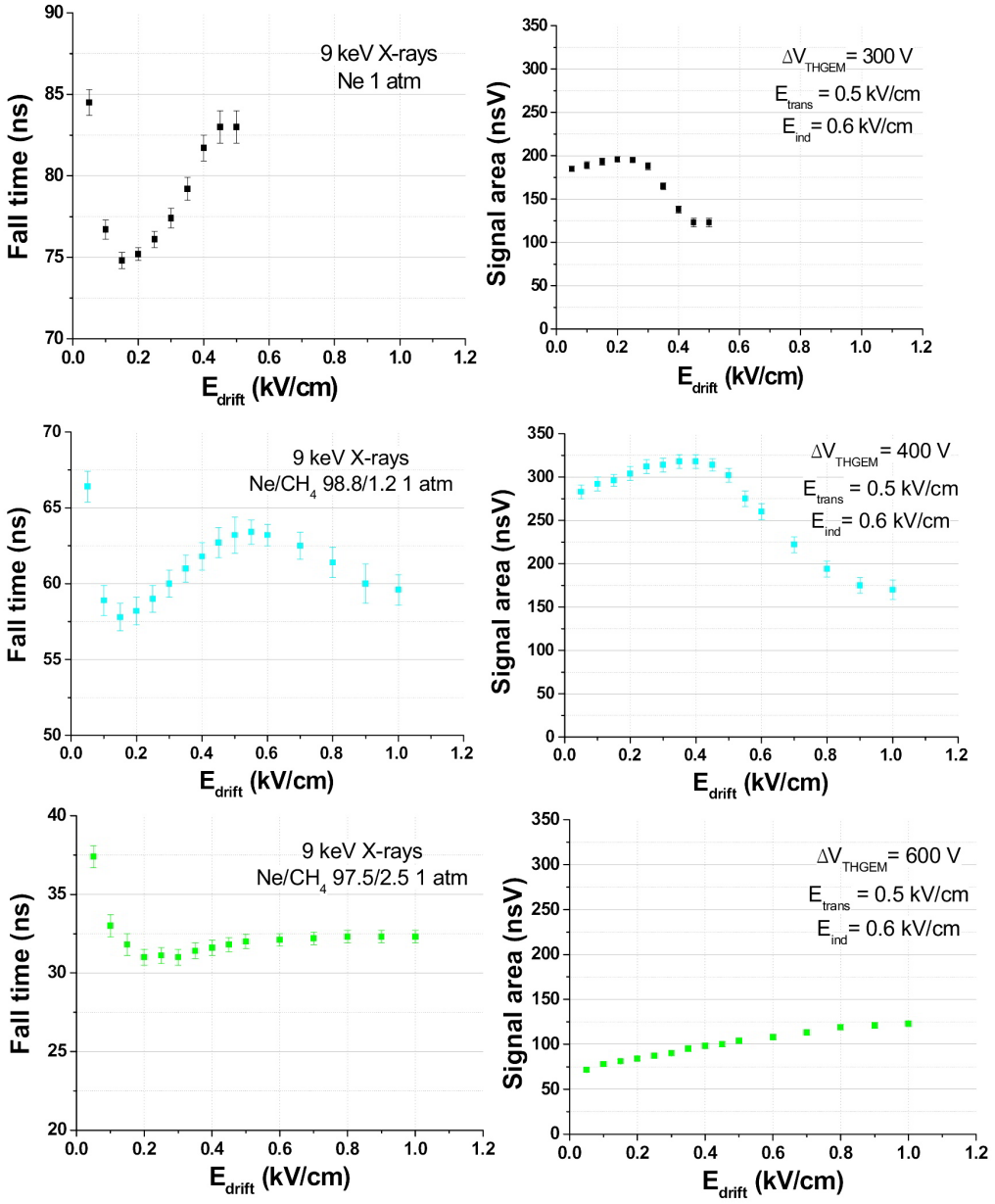

Figure 8.2: Fall time and area of the signal taken on the 2THGEM top, for different gaseous mixtures.

ture; it seemed preferable, in fact, to have the shortest fall time, while a sufficiently high gain is achieved in every case.
The minimal fall time achieved with different CH_4 concentrations is plotted in Fig. 8.3. The reduction of the signal fall time is visible by observing the pulse-

shape on the scope (see Fig. 8.4).

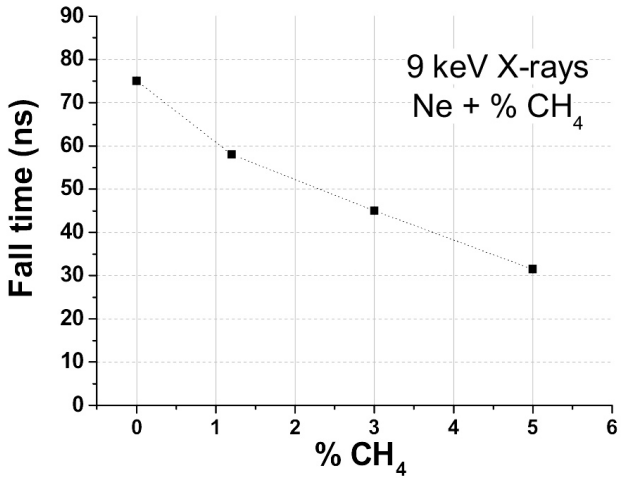

Figure 8.3: Fall time of signal obtained from the 2THGEM top, as function of methane concentration.

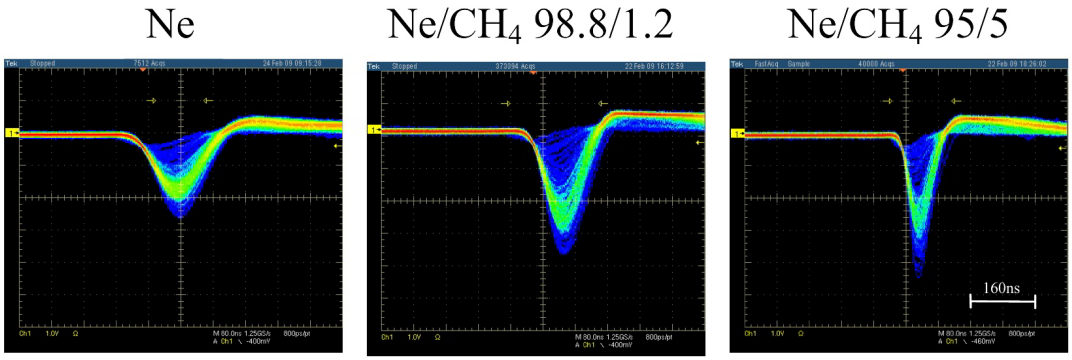

Figure 8.4: Pulse-shape of the 2THGEM top signal for different Ne/CH_4 mixtures.

8.3 Image homogeneity

In order to evaluate the homogeneity of an empty field (i.e. without objects), the entire area of the detector filled with Ne gas was irradiated with 9 keV X-rays for 5 hours (effective gain: $\sim 10^5$, total counts: $1.87 \cdot 10^8$, counting rate: $\sim$ Hz/mm^2).

The obtained image in grey-scale is shown in Fig. 8.5 left: some cold spots are visible, corresponding to regions with lower detection efficiency, that can be caused by dust within the detector, by defects in the graphite anode or by ineffective holes in the THGEM electrodes. Apart from these defects, the empty field image appears acceptably homogeneous, with an overall gain uniformity.
This image was analyzed in order to evaluate the detector electronic noise. Plot in Fig. 8.5 (right) presents the frequency histogram of pixel counts, together with the results of a gaussian fit. The average number of counts per single pixel is 174, with a standard deviation of $\sigma = 16.54$, corresponding to an average spread of 9.5% (slightly more than the purely statistical Poisson width of 7.5%).
In term of signal-to-noise ratio (SNR):

$$\mathrm{SNR} = 20\log_{10}(\mathrm{Mean}/\sigma) = 20.5 \text{ dB} \tag{8.1}$$

which is to some extent better that the value obtained with Ar/CH_4 (SNR = 16.9 dB) [59].

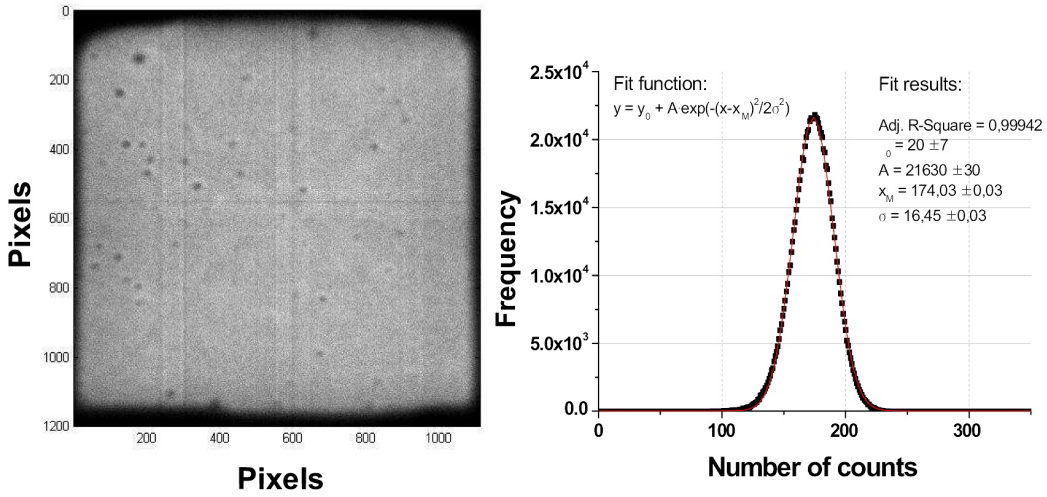

Figure 8.5: Empty field image, irradiating the detector with 9 keV X-rays. On the right, the obtained distribution of counts is fitted with a gaussian function.

8.4 Gain uniformity

The detector gain uniformity was investigated irradiating the detector with the ^{55}Fe 5.9 keV photon source. The source, with a collimator of 1 mm in diameter,

was sequentially placed on a grid of 25 equidistant points across the detector window; for each step, the signal area of the 2THGEM top signal was acquired. The detector was filled with Ne/CH_4 98.8/1.2, and it was operated with ΔV_{THGEM} = 410 V, corresponding to an average gain of around 10^6. As shown in Fig. 8.6, a gain distribution with 22% FWHM has been measured.

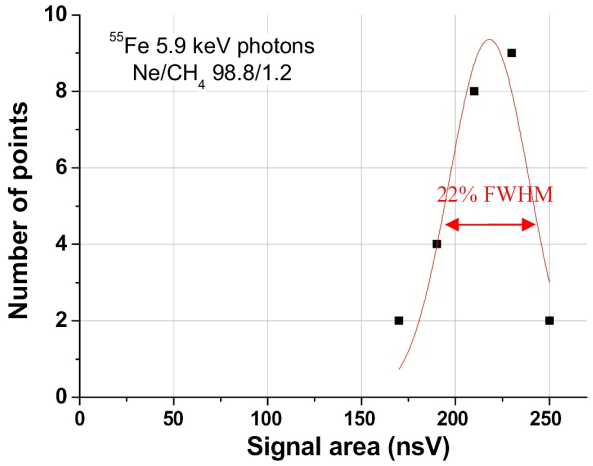

Figure 8.6: Distribution of the gain measured at 25 different points over the detector sensitive area.

8.5 Spatial resolution

The spatial resolution of the detector filled with different mixtures of Ne/CH_4 has been evaluated by means of the ESF analysis method, as explained in Sec. 7.2. For each measurement, an appropriate voltage across the THGEM electrodes was applied in order to achieve an effective gain around 10^5. The detector was irradiated with X-rays generated by the Roentgen tube (voltage: 10 kV). Table 8.1 shows the spatial resolution measured in Ne based mixtures, with 0%, 1.2% and 5% CH_4. Adding several percent of methane to the Ne gas noticeably improves the spatial resolution. This phenomenon can be explained with the increasing electron drift velocity as a function of CH_4 concentration, which in turn produces faster signal pulses.
Even working with a lower gain (10^4), an analogous detector filled with Ar/CH_4 95/5 provided a much better spatial resolution [59]. This fact can be explained considering the projected range of primary electrons in the two noble gases. The projected range (R_p) of electrons in gas, for energies up to few hundred keV, can

Ne + % CH_4	Spatial resolution (FHWM)
0%	5.0 ± 0.6 mm
1.2%	2.8 ± 0.2 mm
5%	1.20 ± 0.15 mm

Table 8.1: Spatial resolution, in terms of the PSF FWHM, measured irradiating the detector with X-rays from the Roentgen tube at 10 kV.

Gas	K-shell binding energy	Photoelectron initial kinetic energy	Density (1 atm, 273 K) (1 atm, 273 K)	Projected Range Range
Ar	3.206 keV	5.773 keV	$1.78 \cdot 10^{-3}$ g/cm^3	0.56 mm
Ne	0.87 keV	8.109 keV	$0.90 \cdot 10^{-3}$ g/cm^3	2 mm

Table 8.2: Projected range computation of K shell photoelectrons emitted by 8.979 keV photons in Ar and Ne.

be estimated by means of the following formula [71]:

$$R_p = 0.71\mathrm{E}^{1.72} \text{ g/cm}^2 \tag{8.2}$$

where E is expressed in MeV. Considering an incoming photon whose energy is 8.979 keV (the K-shell energy in Cu, which is the X-ray tube target material), and the binding energies of K electrons in Ar and Ne, it is possible to calculate the projected range of the photoelectron emitted in the two noble gases (see Table 8.2). (In this analysis, Ar/CH_4 and Ne/CH_4 mixtures are approximated by the respective pure noble gases, since the respective differences in mass stopping power for keV electrons are below 1%). Notice that the projected range of photoelectrons is around four times larger in Ne than in Ar. The detector readout measures the charge-cloud center. Therefore, a longer range of the photoelectron, which is emitted isotropically from the point of interaction of the X-ray photon, directly affects the position resolution measured with the ESF method.
Auger electrons should be taken into account in this analysis as well. In our case, considering the maximum kinetic energy achievable by an Auger electron (i.e. around the K-shell binding energy), their projected range turns out to be about 0.2 mm in Ar and 40 μm in Ne; these values do not affect our previous considerations.
Looking carefully at the image taken with Ne/CH_4 95/5 (see Fig. 8.7 right), one notices a structure of bumps that was immediately recognized as the hexagonal pattern of THGEM holes. This fact proved that the spatial resolution of the gaseous detector, being capable of resolving the submillimetric granularity of the multiplier electrode, must be better than estimated.

In order to reduce the photoelectron range, the detector (filled with Ne/CH_4 95/5)

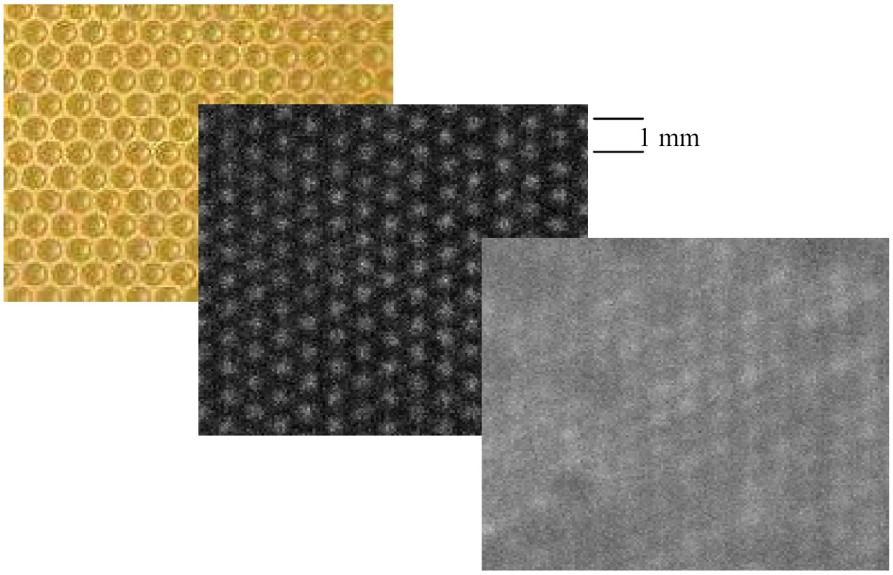

Figure 8.7: From left to right: a picture of the holes pattern on a THGEM surface, compared with images taken irradiating the detector with the X-ray tube, set respectively at 5 kV and 10 kV. In both cases the detector was filled with Ne/CH_4 95/5.

was irradiated decreasing the X-ray tube voltage to 5 kV (that is below the target Cu K-shell binding energy); therefore, a 5 keV bremsstrahlung photon spectrum was produced. The ESF analysis of the obtained image, in which the hole pattern appears prominently (see Fig. 8.7), achieved a remarkable spatial resolution (FWHM) of 0.30 ± 0.05 mm. This result was obtained by analyzing the sum of 100 rows of pixels (pixel linear dimension: 0.0797 mm); it means that in the ESF analysis the bump structure has been integrated along several rows of holes, thus affecting the edge steepness. It is therefore plausible to infer that the spatial resolution of the read-out imaging board itself is even better.
When the detector is irradiated with the Roentgen tube set at 10 kV, the photon electron range is of the same order of magnitude as the holes pattern; therefore, the secondary electron clouds released in the conversion gap is with high probability focused in more than a single hole; for this reason, the hexagonal pattern is less evident than in the 5 keV bremsstrahlung photon case, as shown in Fig. 8.7 right.
Irradiating the whole detector window with 5 keV bremsstrahlung photons (acquisition rate: 300 Hz, total events: $1.25 \cdot 10^7$) the revealing image shown in Fig. 8.8

was obtained. The charge avalanches that emerge from 2THGEM are localized to such an extent that each hole is imaged separately from the others. This image allows to detect some blind holes, that is holes in which no multiplication occurs: a couple of tens of black spots are indeed visible. A larger region of lower efficiency is observed close to the right edge, possibly due to a cluster of blind holes, or to a defect on the resistive anode.
The holes appears regularly arranged in the hexagonal pattern, except in the corners and along a horizontal strip parallel to the lower edge. Therefore, no significant image distortions are detected.

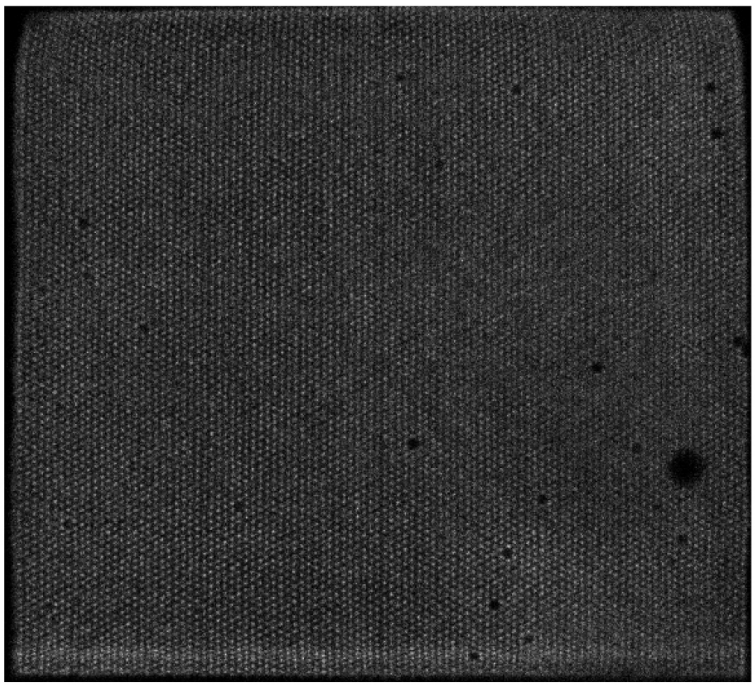

Figure 8.8: Image acquired irradiating the whole detector area with 5 keV bremsstrahlung photons (300 Hz, events: $1.25 \cdot 10^7$).

8.6 Signal pulse-shape along the DAQ chain

The best imaging resolution was obtained, with high stability, when the detector was filled with Ne/CH_4 95/5. Here, it is instructive to show the pulse-shape characteristics of the signal, following each step of the electronic chain.
In the next series the signal area and amplitude, together with the average fall time and signal to noise ratio (S/N) (defined as the ratio between amplitude and noise

RMS) are indicated. The detector was irradiated with 9 keV photons from the Roentgen tube, and ΔV_{THGEM} was set at 610 V.
Figs. 8.9 and 8.10 present typical output signals from the preamplifiers and the TFA. Pulse shapes were acquired by means of the Tektronix TDS5104B oscilloscope.

Trigger signal from the preamplifier:
Signal area = 4.9 ± 0.1 *nsV*; signal amplitude = 89 ± 3 mV; fall time = 30.2 ± 0.4 ns; SNR ratio= 38.

Position signals from the preamplifier:
Signal area = 1.3 ± 0.6 *nsV*; signal amplitude = 20 ± 7 mV; fall time = 31 ± 0.6 ns; SNR ratio= 17.

Trigger signal from the TFA:
Signal area = 191 ± 8 nsV; signal amplitude = 3.1 ± 0.1 V; fall time = 31.4 ± 0.4 ns; SNR ratio= 62.

Position signals from the TFA:
Signal area = 136 ± 5 nsV; signal amplitude = 2.6 ± 0.1 V; fall time = 30.3 ± 0.3 ns; SNR ratio= 34.

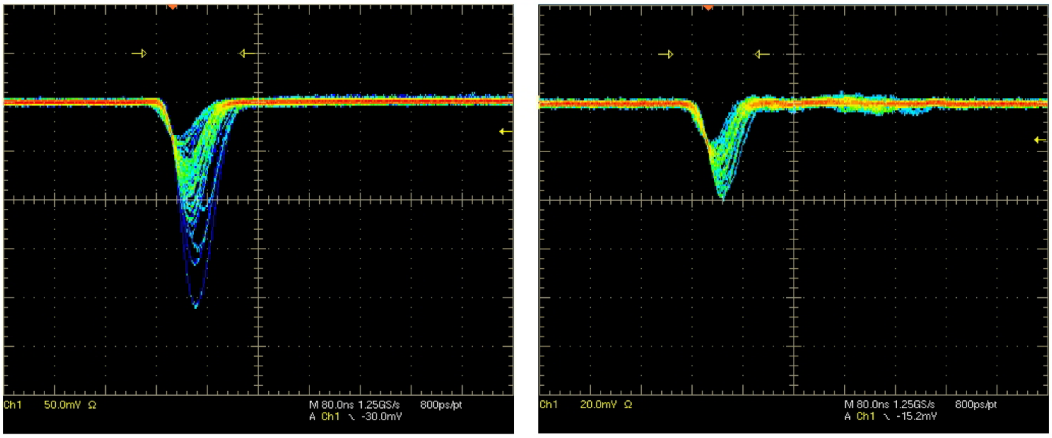

Figure 8.9: Typical pulse shapes of the preamplifier outputs. On the left: trigger signal; on the right: channel x1. Y-scale: 50 mV, x-scale: 80 ns.

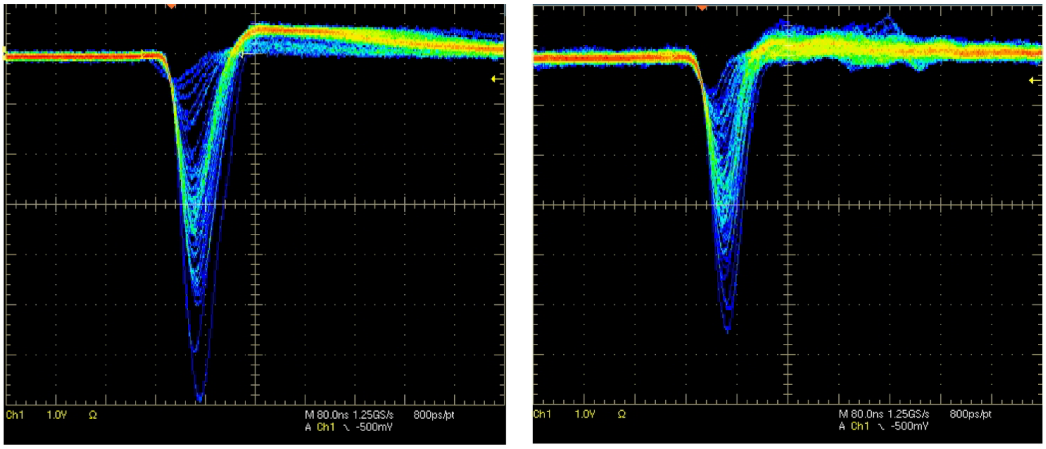

Figure 8.10: Typical pulse shapes of the TFA amplifier outputs. On the left: trigger signal; on the right: channel x1. Y-scale: 1 V, x-scale: 80 ns.

8.7 Measurements with an α source

8.7.1 Signal area versus ΔV_{THGEM}

Since it was planned to couple the gaseous detector to a neutron-to-charged-particle converter, an ^{214}Am α source was also inserted in the detector filled with Ne/CH_4. The conversion gap thickness was set at 3.4 mm. The test was aimed at finding the appropriate gain, in order to detect the α particles under stable conditions.
A calculation was performed by means of the SRIM [67] code. The tracks of 4.5 MeV α particles were simulated, emitted in a parallel beam in Ne/CH_4 at 1 atm. Initially, they traverse a gap of 12.3 mm, corresponding to the distance between the source and the cathode mesh, and then they enter into the 3.4 mm thick conversion gap. The mean energy deposited in this gap is calculated as 260 keV, that is around 29 times more than the energy of a 9 keV photon.
Taking into account the W factor of Ne, a yield of around $7 \cdot 10^3$ secondary electrons can be estimated. Several measurements were taken with the detector filled with two different gaseous mixtures, namely, Ne plus 1.2% and 5% of CH_4. Due to the large amount of charge released by α particles in the gas, the maximum sustainable ΔV_{THGEM} values were respectively 370 V and 570 V, much lower than when the detector is irradiated with 9 keV photons. At such voltages, the detector was completely stable, while increasing the voltage by several volts caused it to spark continuously. In both the gaseous mixtures the Raether limit) was probably reached.
Table 10.3 shows the area of the signal taken on the 2THGEM top. It can be ob-

% CH_4	ΔV_{THGEM}	9 keV X-rays	^{214}Am α particles	Ratio α/X-rays
1.2	340 V	10.1 ± 0.2 nsV	262 ± 5 nsV	26
1.2	360 V	28.8 ± 0.8 nsV	513 ± 7 nsV	18
1.2	370 V	55.7 ± 1.2 nsV	587 ± 8 nsV	11
5	530 V	11.5 ± 0.3 nsV	262 ± 6 nsV	23
5	550 V	37.9 ± 1.5 nsV	392 ± 7 nsV	10
5	570 V	92.0 ± 3.5 nsV	512 ± 9 nsV	6

Table 8.3: 2THGEM top signal areas, taken with two percentages of CH_4, at different ΔV_{THGEM} values and irradiating the detector with two kinds of sources.

served that, for both mixtures, the ratio between signal areas measured using the α and X-ray sources decreases as function of ΔV_{THGEM}. This effect can be explained considering that, in the α case, the large amount of free charges traversing the THGEM holes causes a distortion of the electric field lines. In other words, the very large charge clouds of electrons and ions multiplied in the holes, produce a sort of screening effect of the electric field, which affects the effective gain. Such an effect is anything but a disadvantage; in fact, it improves the detector dynamic range, extending the capability of detecting high ionizing events without sparks.

8.7.2 Signal pulse-shape along the DAQ chain

As in the X-ray case, it is instructive to consider the signal pulse shape along the DAQ chain, when the detector is irradiated with the ^{241}Am source. The detector was filled with Ne/CH_4 95/5, and ΔV_{THGEM} was set at 570 V.

Trigger signal from the preamplifier:
Signal area = 15.1 ± 0.3 nsV; signal amplitude = 105 ± 2 mV; fall time = 67 ± 2 ns; SNR ratio= 50.

Position signals from the preamplifier:
Signal area = 5.5 ± 0.1 nsV; signal amplitude = 40.5 ± 0.5 mV; fall time = 87 ± 2 ns; SNR ratio= 48.

Trigger signal from the TFA:
Signal area = 511 ± 10 nsV; signal amplitude = 3.9 ± 0.9 V; fall time = 54 ± 2 ns; SNR ratio= 74.

Position signals from the TFA:
Signal area = 470 ± 9 nsV; signal amplitude = 3.6 ± 0.1 V; fall time = 79 ± 2 ns;

SNR ratio= 49.

Figs. 8.11 and 8.12 present typical output signals from the preamplifiers and the TFA. As far as signal duration is concerned, such pulse-shapes are much longer than those obtained irradiating the detector with 9 keV photons. This is an effect of the time interval that α particles take to traverse the conversion gap; in fact, α particles with energy of the order of an MeV have a velocity of the order of 7 mm/ns.

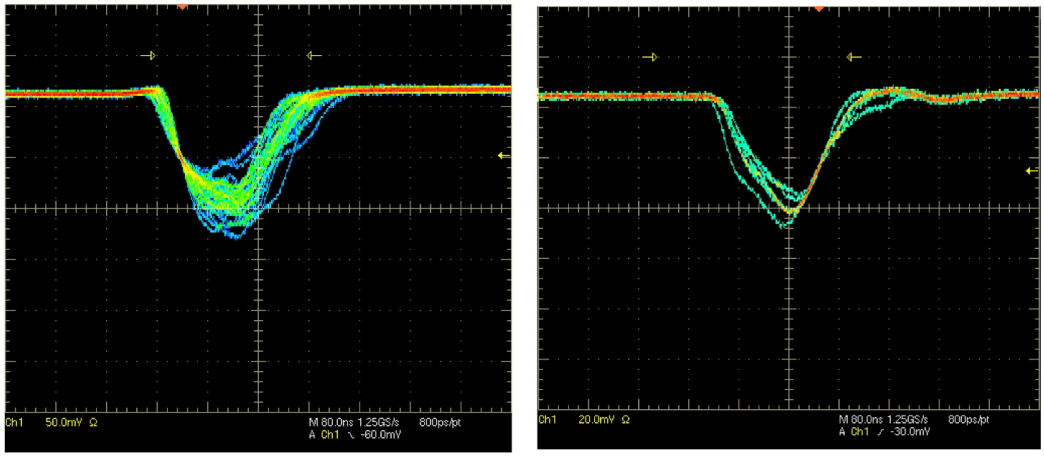

Figure 8.11: Typical pulse shapes of the preamplifier outputs. On the left: trigger signal (y-scale: 50 mV, x-scale: 80 ns); on the right: channel x1 (y-scale: 20 mV, x-scale: 80 ns).

8.8 Summary

The gaseous detector was filled with several Ne/CH_4 mixtures; the dependence of the gain curves on the CH_4 concentration was measured, yielding a maximum effective gain of the order of 10^6 with 0%, 0.6% and 1.2% of CH_4, and of the order of 10^5, with 2.5% and 5% of CH_4. A digital SNR of 20.5 dB was obtained, along with a gain inhomogeneity on the sensitive area surface of 22% (FWHM). Due to the high achievable gain and to the improved signal speed that is obtained when adding several percent of CH_4 to the Ne, a spatial resolution of 0.30 ± 0.05 mm was obtained with a Ne/CH_4 95/5 mixture, using a 5 keV bremsstrahlung photon source. Finally, the detector irradiated with a ^{241}Am α source was operated in fully stable conditions, setting maximum ΔV_{THGEM} values of 370 V and 570 V, respectively in the 1.2% and 5% CH_4 cases.

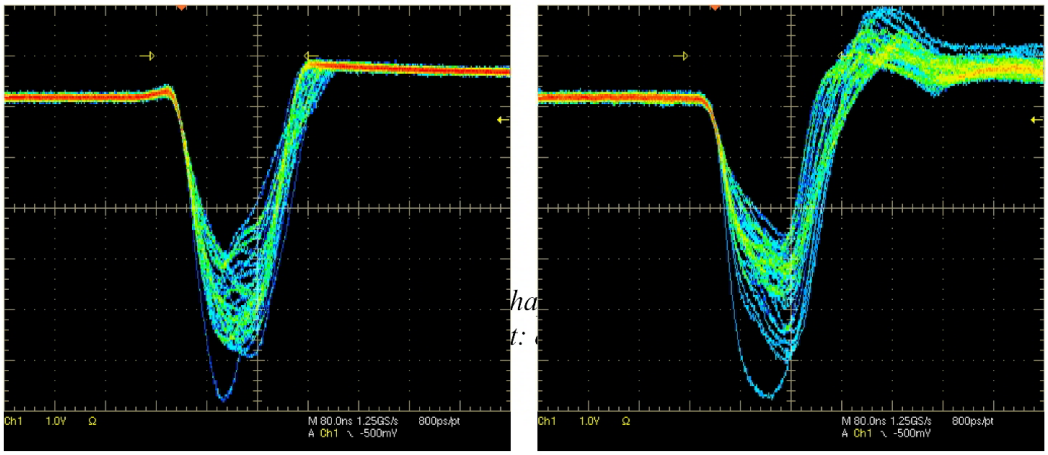

Figure 8.12: Typical pulse shapes of the amplifier outputs. On the left: trigger signal; on the right: channel x1. Y-scale: 1 V, x-scale: 80 ns

Chapter 9

Spectrometer set up and preliminary tests at PTB

Before using a spectrometer in a neutron field with a continuous spectrum and performing spectral unfolding, it is necessary to accurately characterize the detector RFs. Usually, RFs are derived both from MC simulations and experimental measurements, irradiating the detector in monoenergetic beams with various moderator configurations [52]. In this chapter, the first characterization tests carried out with the neutron spectrometer are described. The detector was irradiated in reference neutron beams at the accelerator facility of the Neutron Radiation Department at PTB [72].
Initially, the gaseous detector (filled with Ne/CH_4) was assembled following the design developed by means of MC simulations (Sec. 9.1), and some calculations were performed with SRIM regarding the energy released in the conversion gap by charged particles emerging from the ^{10}B layer (Sec. 9.2).
Then, preliminary tests were performed in monoenergetic neutron beams (1.2 MeV, 5.0 MeV and 4.9 MeV), in order to adjust the electronic settings and to set a proper detector gain (Sec. 9.3). A sort of feasibility test for RF evaluation was carried out placing in front of the detector some simple moderators and comparing the obtained counting rates with MCNP5 calculations (Sec. 9.4).
Finally, a campaign of measurements was carried out with the purpose of characterizing the detector RFs (Sec. 9.5). The aim was to irradiate the spectrometer in various monoenergetic incident beams (with energies between 0.565 MeV and 14.8 MeV) and with different moderator thicknesses (from 0 to 196 mm), and to compare the results with MC calculations. Such a comparison was not fully satisfying, as will be shown below, mainly because of uncertainties on material composition and limitations of the MC code employed.

9.1 Detector set up

The gaseous detector set up, described in Chapter 6, was adjusted for neutron detection, on the basis of the design developed in Chapter 5 by means of MC calculations. The 20 cm diameter stainless steel chamber that contains the gaseous detector was closed with a frontal plate of aluminium (1 mm thick). Following the results obtained with MC calculations, the gaseous detector has been assembled in the "reverse" mode, that is with the read out electrode facing the Al window and with a pure PE albedo reflector close to the cathode (see Fig. 9.1). The albedo reflector has a cylindrical shape, 30 mm thick and with a diameter of 17.5 cm. The conversion gap thickness was set at 3.3 mm.

The neutron converter is made with a 0.1 mm thick aluminium foil, whose sur-

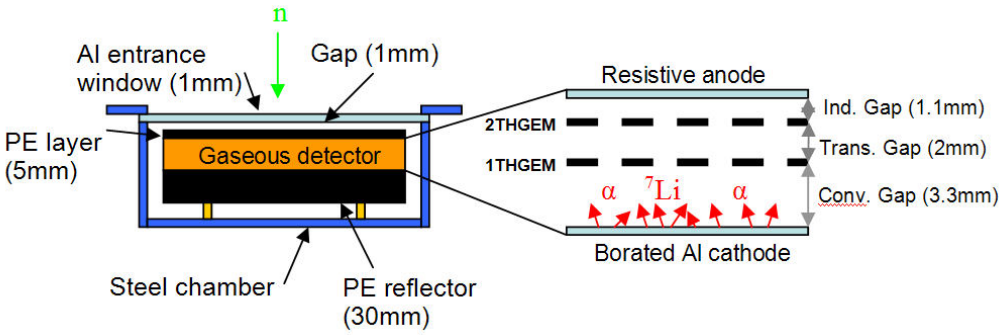

Figure 9.1: General scheme of the detector in the final configuration.

face of 100×100 mm^2 is coated with a 2 μm thick ^{10}B layer. The manufacturer (CASCADE Detector Technology GmbH) guarantees a thickness dishomogeneity of the boron layer less than 4%. In Fig. 9.2, the boron coated Al layer is visible in the steel chamber.

When the chamber had to be filled with gas, it was previously pumped out for about 20 minutes at a pressure of few 10^{-2} millibars; in this condition, the Al window had to resist to a pressure of about 1 atm. In order to protect the inner parts, a $120 \times 120 \times 5$ mm^3 PE layer has been inserted between the read out board and the window (leaving 1 mm of gap between the window and the PE layer). When the chamber is pumped, the Al layer is apparently bent, filling the 1 mm gap and touching the PE layer surface, without anyway affecting the detector operational behavior.

A gas system based on MKS gas mixer mod. 462 was used, unlike the one used at WIS. The detector was filled with a Ne/CH_4 95/5 mixture and continuously flushed with a flow rate of about 140 sccm. Such a mixture was chosen because,

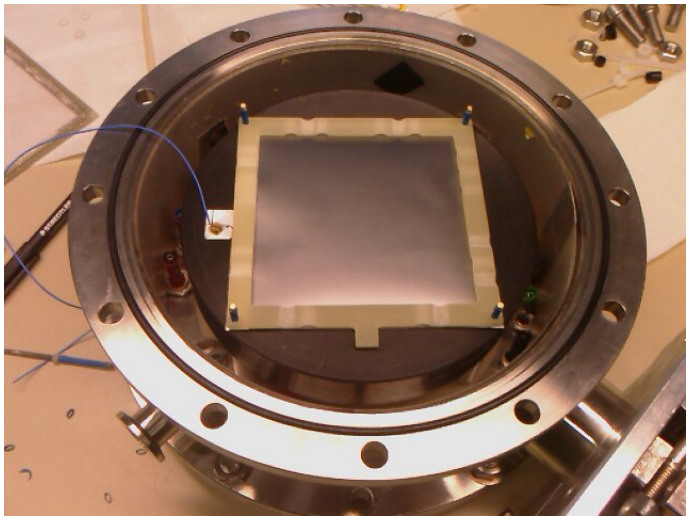

Figure 9.2: The boron coated Al layer is visible in the steel chamber, together with the cylindrical PE albedo reflector.

during the tests carried out at WIS, the gaseous detector filled with the same mixture provided the best performance in terms of reliability and imaging.
In order to test the detector in some neutron reference beams, the detector itself, the preamplifier box, the five TFAs, the HV supply for the anode and the gas system have been installed in the Irradiation Hall; all the remaining electronic devices (TFAs, HV supplies, PC and a digital oscilloscope) were set in the Control Room. The connection between the Irradiation Room and the Control Room consisted of 80 m long BNC and HV BNC cables.

9.2 Calculations with SRIM

Neutrons reaching the converter layer can interact with the ^{10}B nuclei; the capture cross section for thermal neutrons, in particular, is 3837 b. As already mentioned in Sec. 1.1, when such a reaction happens, with 94% of probability an α particle and a ^{7}Li ion are emitted, with respective kinetic energy of 1.47 MeV and 0.84 MeV, together with a 477 keV photon.
Some estimations about the secondary particles emitted by the boron neutron captures in the conversion gap have been carried out with the SRIM software. An α particle emitted in the Ne/CH_4 gas from the boron layer surface has a LET of 1.12 MeV/cm with a projected range of 15.1 mm. In the same condition, a ^{7}Li ion would enter in the gas with a LET of 1.58 MeV/cm and having a projected range of 8.9 mm. Therefore, both kinds of particles can get across the conversion gap.

The W ratio is 36 eV for 1 atm Ne gas [71]. A 1.47 MeV α particle, crossing perpendicularly the 3.3 mm conversion gap, releases in it an energy of 360 keV, creating 10^4 electron-ion couples. A 0.84 MeV ^{7}Li particle, on the other hand, would deposit 450 keV, creating $1.25 \cdot 10^4$ electron-ion couples. Considering an α particle releasing all its energy in the gap (corresponding to a high incidence angle track), $4.08 \cdot 10^4$ electron-ion couples would be created. The previous considerations can be used in order to achieve an estimation of the necessary dynamic range (the detector should in fact detect the most ionizing events without sparking).

9.3 Electronic settings

At first, the spectrometer prototype was irradiated in a monoenergetic neutron beam in order to properly adjust the electronic settings. Initially, the HV bias were set in order to get the following electric field values:

E_{conv} = 0.6 kV/cm
E_{trans} = 0.5 kV/cm
E_{ind} = 0.6 kV/cm (initial value, varied afterwards)

At the beginning of the test the gain of the trigger TFA was set at 50x, and those related to the four spatial channels at 200x.
The detector was placed at 31 cm of distance from the neutron source, consisting in a D(d,n)^{3}He gaseous target. The deuterium gas was contained at 180 kPa in a 3 cm long vessel, having a Molybdenum window of 5 μm. The target was irradiated with a 2.5 μA deuterium beam, resulting in a neutron flux in the frontal direction of $1.59 \cdot 10^5$ cm^{-2}s^{-1} (at the detector window), with an energy of 5.9$\pm$0.2 MeV. No PE/B moderator was placed in front of the Al window.
When the neutron beam was on, the maximum ΔV_{THGEM} sustainable was 600 V (the corresponding gain obtained with 9 keV photons was around 10^5); in this condition the detector was not sparking at all, while at ΔV_{THGEM} = 610 V it sparked continuously. Therefore, it can be reasonably argued that at ΔV_{THGEM} = 600 V the detector was operating close to the Raether limit.
Since the signal amplitudes were huge, the gain of the trigger TFA was decreased from 50x to 20x, and those related to the four spatial channels from 200x to 100x. Fig. 9.3 shows the signals from the TFAs, related to the trigger, $x1$ and $x2$ channels ($y1$ and $y2$ are comparable with $x1$ and $x2$). The CFTD trigger threshold was set at 400 mV, with a resulting frequency of 11 kHZ, while the thresholds of the four stops was 60 mV. In Table 9.1 the average falling time and amplitude are reported.
These values can be compared with those obtained with a similar set up at WIS, irradiating the detector with 4.5 MeV α particles from a ^{241}Am source. In that

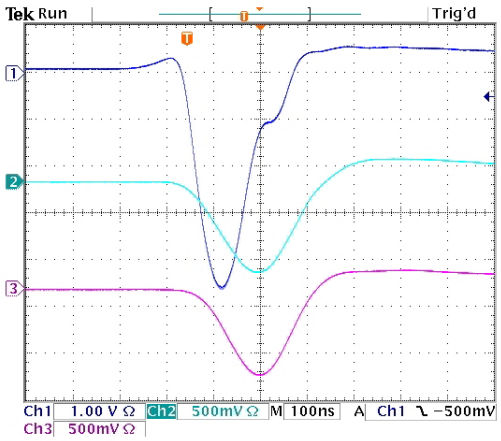

Figure 9.3: Trigger (Ch1), $x1$ (Ch2) and $x2$ (Ch3) signals from the TFAs, with ΔV_{THGEM} = 600 V. Signals are averaged on 128 samples.

Channel	TFA gain	Falling time	Amplitude
Trigger	20x	55 ns	4.2 V
$x1$	100x	80 ns	1.5 V

Table 9.1: Average characteristics of signals shown in Fig. 9.3.

set up the energy deposited by α particles in the 3.3 mm conversion gap was calculated in 260 keV with SRIM. In that measurement, the detector was assembled with the same electrodes except for the cathode, that was a metal mesh. The gaps between the electrodes and the HV settings were the same except the ΔV_{THGEM}, that was set at 580 V. Moreover, the trigger and spatial TFA gains were set at 50x and 200x, respectively. In that occasion, the trigger signal from the TFA had an average falling time of 54 ns and an amplitude of 3.9 V, while the respective values related to the $x1$ signal were 79 ns and 3.6 V.
Since in a noble gas plus quencher mixture the timing characteristics of signals strongly depend on the quencher percentage, the very good agreement between the falling times between the PTB and the WIS setups confirms the reliability of the two gas mixer systems.
By means of the CoboldPc software some images were taken. Remarkable inhomogeneities were detected, whose origin was recognized in cross-talk effects in the fast pre-amplifier box due to the excessive signal amplitudes. For this reason, ΔV_{THGEM} was progressively reduced until 530 V (the corresponding gain obtained with 9 keV photons was around 10^4), causing the diminution of distortion effects. Since the CFTD works properly when the input signals are below

Channel	TFA gain	Falling time	Amplitude
Trigger	6x	60 ns	240 mV
$x1$	60x	72 ns	180 mV

Table 9.2: Average characteristics of signals shown in Fig. 9.4.

2 V, the trigger TFA gain was decreased to 6x and that of the four channels to 60x. Since in these conditions the trigger rate of the four position channels was significantly lower, E_{inv} was set at 1 kV/cm. Moreover, the trigger threshold was set at 300 mV. Signals from the TFAs are shown in Fig. 9.4 and described in Table 9.2; the trigger frequency was 9.5 kHz.

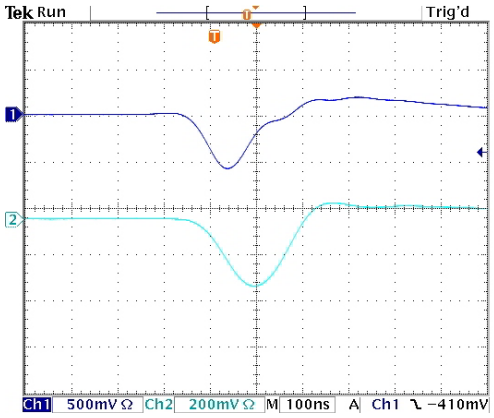

Figure 9.4: Trigger (Ch1) and $x1$ (Ch2) signals from the TFAs, with ΔV_{THGEM} = 530 V. Signals are averaged on 128 samples.

9.4 Evaluation of the detector response with different moderators

Once the electronic settings assuring good quality signals without sparks have been selected, the spectrometer response in neutron beams with two different energies (4.9 MeV and 1.2 MeV) and with several moderator configurations has been investigated. The measured counting rates were checked with MC calculations. This investigation can be seen as a sort of feasibility test for RF measurement.
Two kinds of neutron moderators were used: a PE cylinder (d: 20.5 cm, h: 3.35 cm, ρ = 0.95 g/cm^3) and a set of $20 \times 10 \times 5$ cm^3 PE/B bricks (nominal ^{10}B concentration: 5.6%, ρ = 1.01 g/cm^3). The detector was positioned with the Al window at 42.7 cm from the target. It was irradiated in the following five subsequent configurations:

1. The naked detector (no moderator) (see Fig. 9.5).
2. The PE cylinder was put in contact with the Al window.
3. A wall of PE/B (frontal area: 40×20 cm^2, thickness: 5 cm) was added in front of the PE cylinder.
4. The PE cylinder was removed, keeping the PE/B wall (see Fig. 9.6).
5. A second wall of PE/B bricks was added, for a total thickness of 10 cm.

At first, a deuterium gaseous target was set up. A beam of 2.3 MeV deuterons, with a current of 2.6 μA, irradiated the gaseous target (at 880 mbar), causing at the detector entrance a $4.2 \cdot 10^4$ cm^{-2}s^{-1} flux of 4.9 ± 0.1 MeV neutrons (^{2}H(d,n)^{3}He). The detector was subsequently irradiated in the five configurations; each irradiation took about 15 minutes. Afterwards, the D target was replaced with a T-Ti one (T(p,n)^{3}He). A proton beam of 2.1 MeV with a current of 3.3 μA caused at the detector entrance a flux of 2×10^4 cm^{-2}s^{-1} of 1.2 ± 0.1 MeV neutrons. As in the previous case, measurements in the five configurations were performed.

During each irradiation, an image was acquired, together with the exact irradiation time and the number of counts of a neutron counter, used for determining the relative variations of the neutron fluence during the irradiation of the detector. During the data analysis, the number of events occurred per second in the central 4×4 cm^2 square of the detector sensitive area was achieved, and it was corrected by the neutron fluence fluctuations detected by the monitor (3% of average spread from the mean value). The obtained counting rates, for all the configurations described above and both the neutron energies, are plotted in Fig. 9.7.

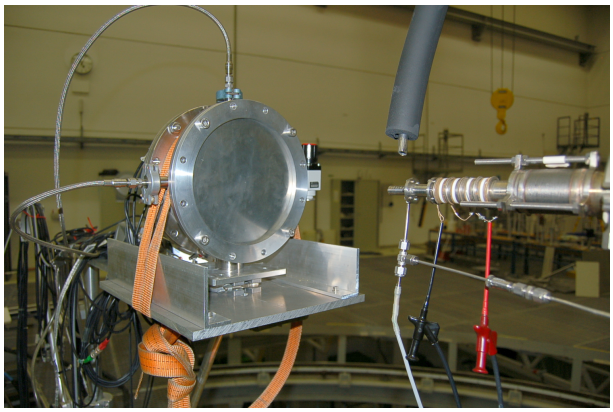

Figure 9.5: The spectrometer placed in the Irradiation Hall in front of the deuterium target.

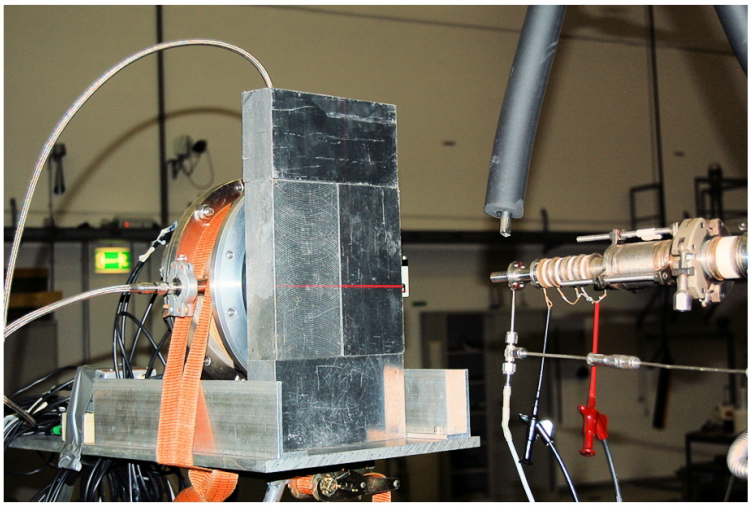

Figure 9.6: The detector shielded with a 5 cm thick PE/B brick wall.

The described experimental set up was reproduced in the MC simulations. For each configuration and incident neutron energy, the amount of neutron captures occurring in the 4×4 cm^2 central region of the B layer was calculated. A monoenergetic and isotropic neutron source irradiating the detector in the various configurations was simulated. Since no data regarding the actual neutron flux were available, in Fig. 9.7 experimental results are compared with the relative amount of calculated data. For a given neutron energy, MC data are normalized to the respective average counting rate.
The MC simulations reproduced the experimental data trend quite nicely. Anyway, for both energies, MC calculations seem to overestimate the neutron captures achieved in the configurations n. 2 and 3, where the round PE moderator is used. It is known that material sold as "pure PE" (which also the plastic inner parts are made of) usually contains several percentages of added compounds, that may affect the neutron moderation and scattering capability of a given material. Moreover, as far as PE/B is concerned, it was considered in the simulations the nominal boron concentration, that by successive chemical analysis was found to be not so reliable. In order to improve the MC accuracy, a detailed knowledge of the plastic materials is necessary.
Ideally, for a spectrometer based on a neutron-to-charged particle converter, the whole process of radiation conversion should be taken into account for an accurate simulation. In other words, the employed MC code should be able to simulate the neutron transport and captures, together with the spectral and directional distributions of secondary charged particles. In this way, important effects like the self-absorption of the converter material would be considered.

The above mentioned troubles (i. e. uncertainty on the material compositions and of secondary tracking of the used MC code) seriously affected the RF evaluation, as it will be described in the next section.

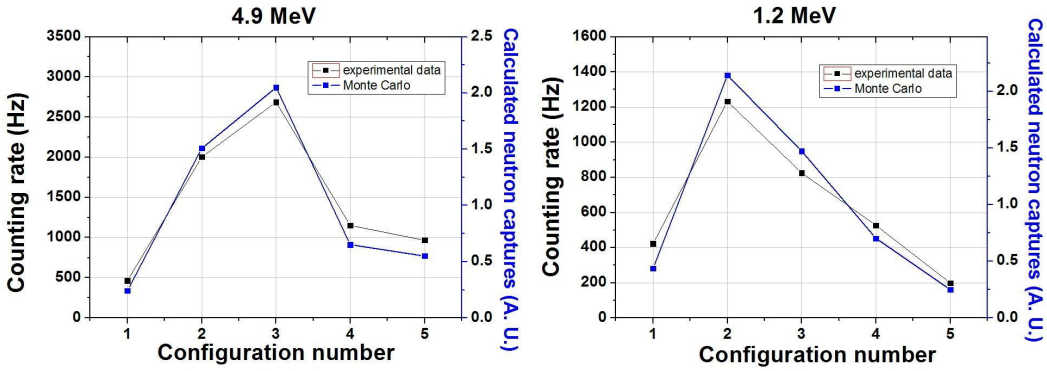

Figure 9.7: Counting rates (black points) in the central 4×4 cm^2 square area compared, for each configuration, with MC data (blue points). The latter are normalized to the mean experimental values. "Configuration numbers" refer to the list of Sec. 9.4.

9.5 RF evaluation

A systematic campaign of measurements was carried out to the purpose of characterizing the detector RFs. Some blocks of PE/B (nominal ^{10}B concentration: 3%) were machined, manufacturing five cylindrical pieces applicable on the detector frontal window. In total, six moderator thicknesses could be achieved: 0, 23, 40, 98, 146 and 196 mm. Fig. 9.8 shows the spectrometer equipped with a 146 mm moderator.

The detector, in each moderator configuration, was irradiated in beams with five different energies, from 0.565 MeV to 14.8 MeV. Table 9.3 reports the neutron sources with the respective energy. In each case an image was acquired, usually containing some 10^5 events.

The absolute neutron flux in the irradiation room was monitored by calibrated neutron detectors. In this way, for each measurement it was possible to achieve the number of counts per unit of incoming fluence. At this step of analysis, the number of counts occurred in the central 4×4 cm^2 area were considered, and they were compared with calculated boron captures in the analogous region of the simulated geometry.

Data concerning the detector in the configuration with no moderator are shown in Table 9.4. As previously mentioned, the performed MC calculations do not take

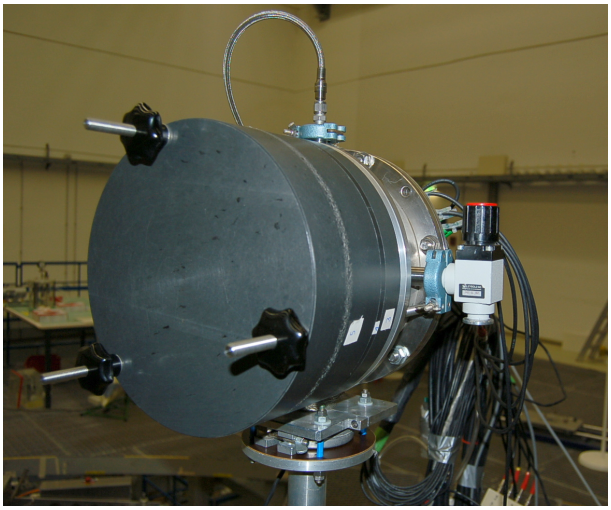

Figure 9.8: The neutron spectrometer equipped with a 146 mm moderator.

Reaction	Target	Neutron energy
^{7}Li(p,n)^{7}Be	LiOH	0.565 $\pm$ 0.015 MeV
^{3}H(p,n)^{3}He	Ti(T)	1.2 $\pm$ 0.091 MeV
^{3}H(p,n)^{3}He	Ti(T)	2.5 $\pm$ 0.127 MeV
^{2}H(d,n)^{3}He	D_2-gas	6 $\pm$ 0.200 MeV
^{3}H(d,n)^{4}He	Ti(T)	14.8 $\pm$ 0.431 MeV

Table 9.3: Characteristic properties of the reference neutron fields at the PTB accelerator facility [72].

into account the probability of secondary charged particles to reach the conversion gap. Since the projected range of α particles (from neutron captures) in solid ^{10}B is 3.5 μm (SRIM), and the boron layer thickness is 2 μm, the expected ratio between calculated neutron captures and measured events should be something more than 2. In Table 9.4, the values of this ratio decreases as a function of incoming neutron energy, ranging from 2.5 (for 0.565 MeV neutrons) to 1.5, for the most energetic neutrons (14.8 MeV). The more energetic are the incoming neutrons, the more simulations underestimate the number of ionizing events in the conversion gap.

In order to explain the discrepancies between experimental and MC data, an hypothesis concerning recoil protons from detector materials was preliminarily investigated. Neutrons having enough kinetic energy, scattering on protons in the various detector components, could produce recoil protons able to ionize the gas the conversion gap. In fact, materials like resin in the THGEM electrodes contain hydrogen, whose nuclei can be knocked-on by neutrons.

Neutron energy	**Experimental data** (Counts ·cm^2)	**MC data** (Captures·cm^2)	**Ratio** (MC/exp.)
0.565 MeV	1.40×10^{-1}	$3.46 \pm 0.04 \times 10^{-1}$	2.5
1.2 MeV	1.03×10^{-1}	$2.17 \pm 0.03 \times 10^{-1}$	2.1
2.5 MeV	5.74×10^{-2}	$1.17 \pm 0.02 \times 10^{-1}$	2.0
6 MeV	2.95×10^{-2}	$5.55 \pm 0.15 \times 10^{-2}$	1.9
14.8 MeV	2.01×10^{-2}	$2.98 \pm 0.11 \times 10^{-2}$	1.5

Table 9.4: Comparison between measured and MC data, expressed per units of incident fluence, obtained with the detector in the naked configuration. In both cases, events in the detector central 16 cm^2 area are considered.

Following this hypothesis, some calculations with the MCNPX [73] code, that enables to simulate recoiling heavy charged particles, were performed. The number of protons incoming in the conversion gap was calculated, with an arbitrary low-energy cut off of 1 MeV. Fig. 9.9 shows a comparison between measured and calculated counts per unit of incident neutron fluence. The calculated counts are defined as follows:

$$\text{MC Counts} = (\text{n. of neutron boron captures})/2.4 + \text{n. of protons} \tag{9.1}$$

The value 2.4, corresponding to the conversion efficiency of the boron layer, seems reasonable and fits the data at best. Despite its arbitrariness, this study can be seen as a first promising step towards the complete comprehension of the experimental data, that would require a simulation with a comprehensive charged particle and neutron transport code.
As far as measurements with moderators are concerned, a not satisfying agreement with measured data has been obtained. Several samples of the employed PE/B blocks were chemically analyzed, detecting a very large spread of ^{10}B (of the order of some percents, even in the same piece). A detailed knowledge of the employed material is definitely necessary for a full characterization of the neutron spectrometer.

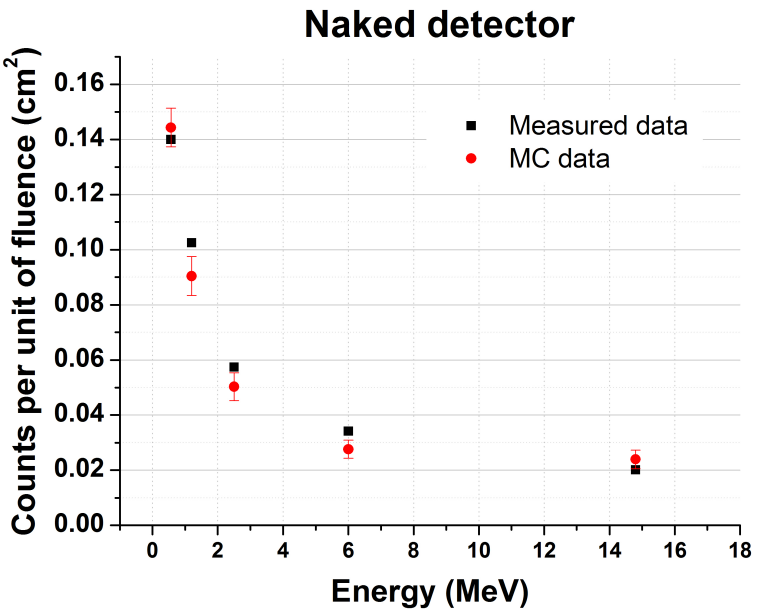

Figure 9.9: Comparison between experimental and calculated data. The counts in the central 16 cm^2 area are shown per unit of incoming neutron fluence. MC data are derived from 9.1.

Conclusions and Outlooks

This thesis work concerns the development of radiation detectors for epithermal neutron beams for BNCT applications. In particular, the here described experimental activity was devoted to improve the dosimetric method based on FGLDs. Moreover, a novel neutron spectrometer with imaging capabilities has been proposed and assembled, and the first important steps of its characterization have been carried out.

At first, the experimental procedure based on FGLDs, that has the unique capability to separately obtain the various dose components in a water equivalent material exposed to an epithermal neutron beam, has been studied and improved. The reliability of the method allowed to use it for the characterization of the LVR-15 epithermal neutron beam, performing in-phantom absorbed dose measurements.

FGLDs with different isotopic compositions were manufactured, inserted in water equivalent phantoms and irradiated at the BNCT facility. Dosimeter images of transmitted light were acquired and analyzed by suitably developed algorithms and, taking into account the sensitivities to the different radiation components, continuous distributions of the various dose components (boron, photon and neutron doses) in a water equivalent material have been achieved.

The experimental set up was simulated by means of MC calculations, using as neutron source the same model that is used by the treatment planning software of the BNCT facility. Calculated in-phantom distributions of neutron transport and absorbed doses have been compared with the experimental results.

Boron dose distributions have been determined on the central plane of both cylindrical and standard water equivalent phantoms, using standard and borated gel dosimeters. The central in-depth dose profile and some transverse profiles were extracted from the dose images. A strong similarity (within few percents) between the boron dose central in-depth profiles of the two phantoms has been found. The boron dose distribution is strictly related to the distribution of the thermal component of the neutron spectrum. In both phantoms the point of maximum boron dose absorption was found on the central axis at 2 cm of depth, which coincides with the point of maximum thermal neutron flux that has been determined by means of MC calculations.

On the other hand, dose transverse profiles in the two phantoms show a dissimilarity that increases with the increasing distance from the central axis. Such trend is confirmed by MC simulations of the thermal neutron flux, and it is due to the loss of inscattering material around the cylinder, with respect to the larger standard phantom. The achieved boron dose distributions were compared with relative calculations of boron neutron captures, finding a very good agreement between the respective distribution trends.
The separation between photon and neutron doses was obtained employing coupled standard and heavy water dosimeters; then, an analysis of the dosimeter images was carried out, requiring the calculation by means of MC simulations of the ratio between neutron dose in light and heavy water. The in-depth profiles of photon and neutron doses in the cylindrical phantom have been determined and compared with data taken by means of TLDs and paired ionization chambers (the latter found in literature), finding a satisfying agreement. The good consistency obtained with other experimental techniques confirms the validity of the proposed method for separating neutron and photon doses, and in particular the adequacy of the parameters chosen for the applied algorithms.
The results shown in this thesis demonstrate the capability of FGLDs to measure continuous distributions of the different dose components in a water equivalent material. Presently, no other dosimetry methods can provide such a possibility. As far as future plans are concerned, it has been noticed that the accuracy of FGLDs applied to photon radiotherapy has been recently drastically increased pre-irradiating each dosimeter in a known uniform photon field, before the measurement irradiation. This procedure allowed to calibrate independently each area of the dosimeter. It is planned, for future measurement campaigns, to perform pre-irradiations of each dosimeter in a reference photon source, that was not possible in the work described in this thesis.

The second part of the experimental activity was devoted to the development of a novel neutron spectrometer with imaging capabilities. Based on the Bonner-sphere principle, it has been designed in order to provide spectral measurements of the neutron beam fast component (100 kev - 20 Mev); moreover, having a flat geometry, it could give useful information regarding the spatial distribution of the incoming neutron beam.
The spectrometer, based on neutron moderators with various thicknesses, a neutron-to-charged-particles converter (consisting in a 2 μm thick ^{10}B layer) and gaseous 2D imaging detector, was designed, assembled and tested. A number of MC calculations has been performed in order to select the best geometric set up and material compositions. A simulated test of the final design has proven, in principle, its capability of unfolding a continuous energy spectrum. As far as the spatial

resolution is concerned, quite poor values have been estimated (some centimeters of FWHM) for the considered neutron energies.
The gaseous detector, having a sensitive area of 10×10 cm^2 is based on double THGEM electrodes coupled to an imaging 2D delay-line board. The gaseous detector was assembled and developed at the Radiation Detection Laboratory of the WIS. Extensive experimental tests were carried out, irradiating the detector with photon and α sources, and investigating its performance with different gaseous mixtures.
At first, the detector was filled with Ar/CH_4 95/5 (1 atm). Irradiating the detector with 5.9 keV photons, a maximum effective gain of $8.5 \cdot 10^3$ was achieved, with an energy resolution of 20% (FHWM). A spatial resolution of 1.7 mm (FHWM) was measured. Moreover, the behaviour of the detector when it is irradiated with α particles from a ^{241}Am was studied, in terms of maximum achievable gain and stability.
Much better performances have been achieved filling the detector with Ne/CH_4 mixtures of various proportions. A maximum effective gain of the order of 10^6 was obtained with 0%, 0.6% and 1.2% of CH_4, and of the order of 10^5, with 2.5% and 5% of CH_4.
Adding some percents of CH_4 to Ne the signal speed is improved. The high gain and signal speed provided by the Ne/CH_4 95/5 mixture allowed to obtain a spatial resolution of 0.3 mm (FHWM), irradiating the detector with a 5 keV bremsstrahlung photon source.
The neutron spectrometer prototype has been assembled following the design optimized by means of MC calculations. The gaseous detector and the ^{10}B layer have been inserted in a steel cylindrical chamber, on whose entrance window some PE/B moderators of various thicknesses can be applied.
The prototype, flushed with a Ne/CH_4 95/5 mixture, has been irradiated in monoenergetic neutron beams (from 0.565 MeV to 14.8 MeV) at the Neutron Physics Department of the PTB. Settings a gain corresponding to 10^4 when it is irradiated with keV photons, the detector could measure, without sparks, neutrons with typical fluences of the order of 10^4 cm^{-2}s^{-1}, with typical counting rates per unit of sensitive area of the order of hundreds of Hz. A campaign of measurements was carried out with the purpose of characterizing the detector RFs with different moderator thicknesses (from 0 to 196 mm).
A not satisfying agreement between measured counting rates and absolute MC calculations was achieved. Mainly, two were the reasons that caused such a discrepancy: the use of a MC code with significant limitations as far as heavy charged particle transport is concerned, and the large uncertainty concerning the isotopic composition of the employed borated plastic.
The next experimental steps for the development of the neutron spectrometer will be the assembly of a novel prototype, whose moderator composition is known in

detail. Due to the difficulty of knowing the exact composition of borated plastic, other geometric configurations of the moderator should be considered, as for example a piece of pure PE coupled to a Cd layer.
A MC code that allows to accurately follow the charged particles produced by neutron boron captures should be used (like GEANT4), in order to include them in the RF calculations. Even if a poor spatial resolution is foreseen, an extensive experimental characterization of this aspect will be performed. The last and most challenging stage of the computational activity will be the development of a "multidimensional" deconvolution algorithm, that will allow to deconvolve the measured data working both in the energy and the spatial degrees of freedom.

Appendix A

The epithermal column of the LVR-15 nuclear reactor

In this work FGLDs have been applied to the characterization of the BNCT facility at the LVR-15 reactor of the Nuclear Research Institute in Řež, near Prague (CZ) [48]. Such a reactor has a nominal power of 9 MW to which corresponds, at the end of its epithermal column properly designed for BNCT experimentation and treatments, a flux of epithermal neutrons of $7 \cdot 10^8$ $cm^{-2}s^{-1}$ (see Fig. A.1 for a schematic representation of the column). The collimator of the epithermal BNCT column has a circular shape, with 12 cm of diameter; Fig. A.2 shows the irradiation room for BNCT treatments.
The neutron spectrum is shown in Fig. A.3; beyond the dominant epithermal component, a not negligible component of fast neutrons is visible, whose contribution to the absorbed dose must be carefully evaluated, due to its high RBE. The construction of the epithermal neutron beam at a horizontal channel of LVR-15 reactor was completed in the year 2000 [74]. A group of patients was treated in the project "Pre-clinical trials of brain tumors" [75]. In the long term the facility at the reactor is utilized for the study of physical and biological aspects of BNCT.

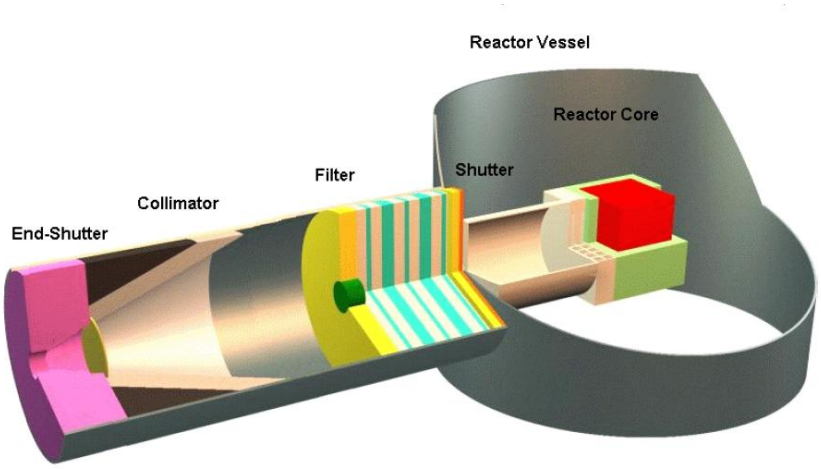

Figure A.1: Scheme of the BNCT epithermal column of the LVR-15 reactor.

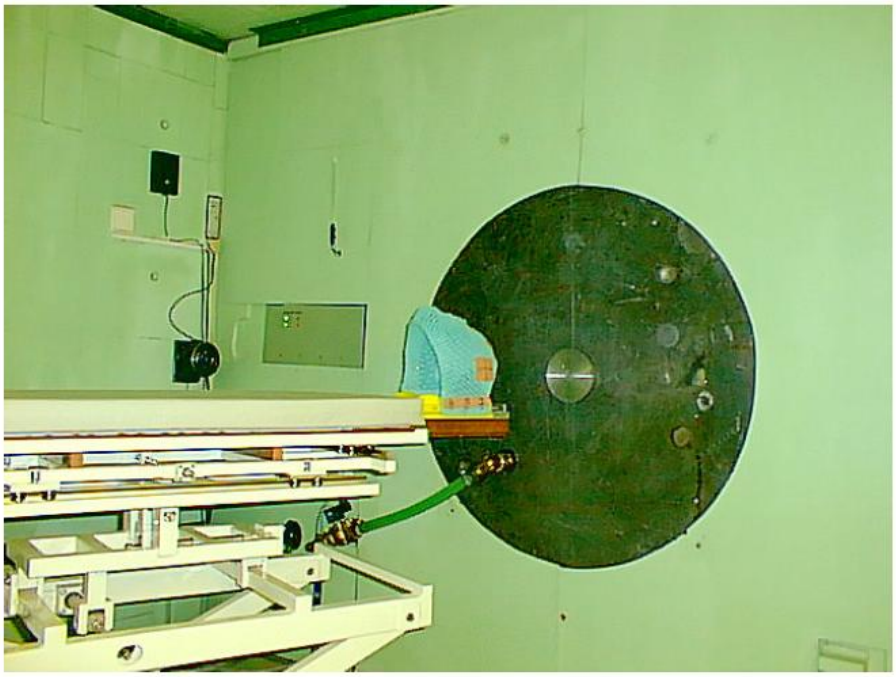

Figure A.2: Irradiation room with the special bed and fixation mask.

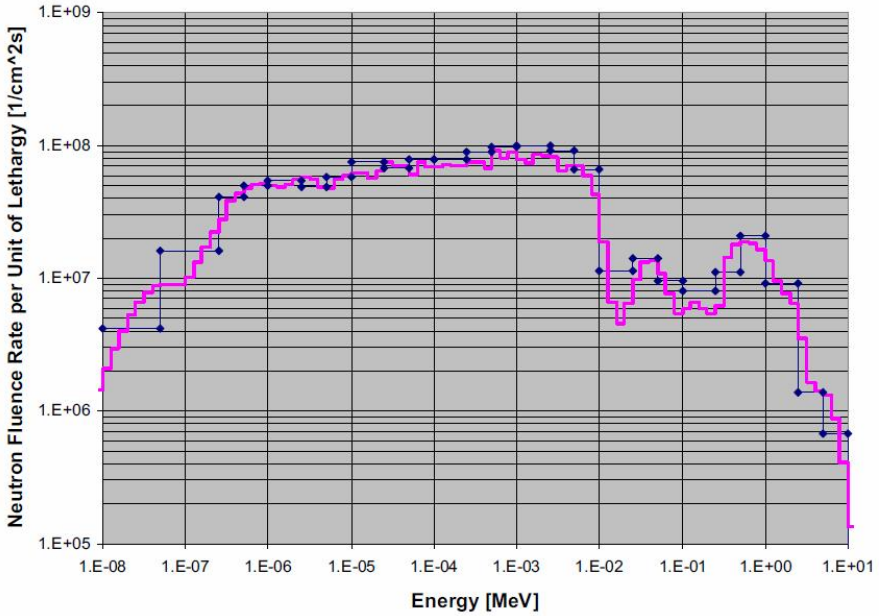

Figure A.3: Neutron spectrum calculated by MCNP code and adjusted with activation foil measurements [48].

Appendix B

Basic principles of gaseous detectors

Aim of this appendix is to describe some basic concepts regarding charge multiplication in gaseous detectors. The reader can find a comprehensive explanation of this topic in [71]; here, just some notions useful to understand the behavior of the detector developed in this thesis work are introduced.
When ionizing radiation crosses a gaseous medium, it undergoes to a discrete number of interactions with the gas atoms, that can be excited and ionized. For example, a photon can interact with an atom by photoelectric effect; then, the electron ejected from its atomic shell can have enough kinetic energy to interact with other atoms and maybe ionize them. At the end, a discrete number of ion-electron pairs are created. The total number of pairs can be expressed as:

$$n_T = \Delta E / W \tag{B.1}$$

where ΔE is the energy released in the medium and W the mean effective energy to produce one pair. In Table B.1 W values of some gases used in this thesis work are reported.
Fig. B.1 depicts a simplified representation of a gaseous detector irradiated in a photon beam, and Fig. B.2 shows the typical trend of the collected charge as function of the voltage applied between the two electrodes.

If no external electric field is present, ions and electrons recombine with each others (region I in the plot). Otherwise, free charges drift along the electric field

Gas	**Z**	**A**	**δ (g/cm^3)**	**W (eV)**
Ar	18	39.9	$1.66 \cdot 10^{-3}$	26
Ne	10	20.2	$8.39 \cdot 10^{-4}$	36
CH_4	10	16	$6.70 \cdot 10^{-4}$	28

Table B.1: Properties of some gases used in this experimental activity.

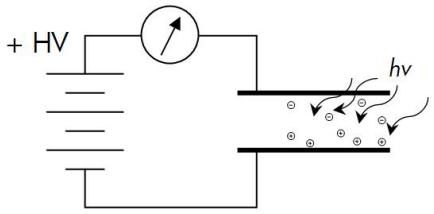

Figure B.1: Basic scheme of a gaseous detector. Free charges produced in the gas by the incoming radiation are collected by the two electrodes.

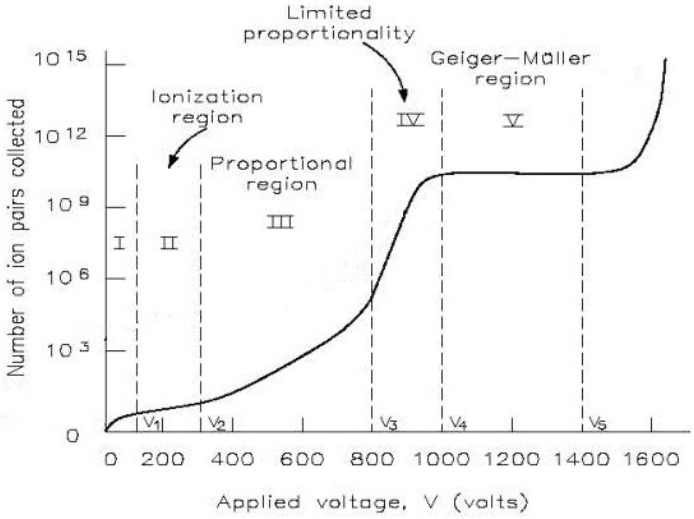

Figure B.2: Charge collected on the electrodes of a typical gaseous detector as function of the voltage applied between them.

lines, and the more intense is the electric field, the lower is the recombination probability (II).
If the electric field is strong enough, then a free electron can gain enough energy to reach the ionization potential, and an ionization encounter may occur. The average distance that an electron has to travel before getting the possibility to ionize an atom is called mean free path for ionization; the inverse of the latter is called first Townsend coefficient (α) and represents the number of ionization pairs created per unit of length. Such a coefficient depends on the gas physical properties and on the electric field strength. After a path dx, if n is the number of free electrons at a given point, the increment of such a quantity will be:

$$dn = n\alpha dx \tag{B.2}$$

and integrating:

$$n = n_0 \exp^{\alpha x} \qquad \text{or} \qquad M = n/n_0 = \exp^{\alpha x} \tag{B.3}$$

where M is called the multiplication factor.
In the general case where α is varying in the space ($\alpha = \alpha(x)$), then M is given by the following:

$$M = \exp\left\{\int_{x_1}^{x_2} \alpha(x)dx\right\} \tag{B.4}$$

This expression describes a multiplication process that is proportional to the initial charge (III). Further increasing the bias between the electrodes, this proportionality is progressively lost (IV), because of the great amount of charges in the gas that causes distortions of the electric field. At even higher voltages, the limited proportionality region ends in a region of saturated gain (V), where the same signal is detected independently of the original ionizing event (Geiger-Müller region).
The multiplication factor cannot be increased at will. Secondary effects, like photon emissions inducing avalanches spread over the gas volume, result in spark breakdown. The phenomenological limit of M is around 10^8, that is called the Raether limit. Usually, the statistical distribution of the electron energies, and therefore of M, does not allow to operate with gain much above 10^6 in order to avoid sparks.

ACRONYMS

ADC	Analog to Digital Converter
BNCT	Boron neutron capture therapy
CCD	Charged Coupled Device
CFD	Constant Fraction Discriminator
DAQ	Data AcQuisition
ESF	Edge Spread Function
FGLD	Fricke Gel Layer Dosimeter
FWHM	Full Width Half Maximum
GL	Grey Level
HDR	High Dose Radiotherapy
IMRT	Intensity Modulated RadioTherapy
LET	Linear Energy Transfer
MC	Monte Carlo
NIM	Nuclear Instrumentation Module
NTCP	Normal Tissue Control Probability
OD	Optical Density
PCB	Printed Circuit Board
PSF	Point Spread Function
RBE	RadioBiological Effectiveness
RF	Response Function
SNR	Signal to Noise Ratio
TDC	Time to Digital Converter
TFA	Time Filter Amplifier
THGEM	THick Gas Electron Multiplier
TLD	ThermoLumuniscence Dosimeter
XO	Xylenol Orange

List of Figures

List of Tables

Bibliography

[1] International Atomic Energy Agency, Current status of neutron capture therapy. IAEA-TECDOC-1223. Vienna (2001). ISSN 1011-4289.

[2] R. F. Barth, J. A. Coderre, M. G. H. Vicente and T. E. Blue, *Boron Neutron Capture Therapy of Cancer: Current Status and Future Prospects*. Clin. Cancer Res. **11**(11) (2005) 3987-4002.

[3] R. F. Barth, *Boron neutron capture therapy at the crossroads: Challenges and opportunities*. App. Rad. Isot. **67** (2009) S3-S6.

[4] O. K. Harling, *Fission reactor based epithermal neutron irradiation facilities for routine clinical application in BNCT - Hatanaka memorial lecture*. App. Rad. Isot. **67** (2009) S7-S10.

[5] H. Jarvinen and W. Voorbraak, Recommendations for the dosimetry of Boron Neutron Capture Therapy (BNCT). NRG Report 21425/03.55339/C (2003) NRG Petten, The Netherlands.

[6] National Institute of Standards and Technology, XCOM Photon Cross Section Database. (http://physics.nist.gov/PhysRefData/Xcom/Text/XCOM.html)

[7] International Commission on Radiation Units and Measurements, Conversion Coefficients for use in Radiological Protection against External Radiation (ICRU Report 57), Bethesda, MD. ICRU Publications, 1998.

[8] R. D. Rogus, O. K. Harling and J. C. Yanch, *Mixed field dosimetry of epithermal neutron beams for boron neutron capture therapy at the MIT-II research reactor*. Med. Phys. **21** (1994) 1611-1625.

[9] D. A. Tattam, D. A. Allen, T. D. Beynon and G. Constantine, *In-phantom neutron fluence measurements in the orthogonal Birmingham boron neutron capture therapy beam*.
Med. Phys. **25** (1998) 1964-1966.

[10] M. Marek, *Small Si-Li detectors for thermal neutron on-line measurements*.
J. The safety of Nuclear Energy **3**(41) (1995) 165-168.

[11] P. M. Munck af Rosenschöld, C. P. Ceberg, J. Capala, K. Sköld and B. R. R. Persson, *Reference dosimetry at the neutron capture therapy facility at Studsvik*.
Med. Phys. **30** (2003) 1569-1579.

[12] C. Aschan, M. Toivonen, S. Savolainen and F. Stecher-Rasmussen, *Experimental correction for thermal neutron sensitivity of gamma ray TL dosemeters irradiated at BNCT beams*.
Radiat. Prot. Dosim. **82** (1999) 65-69.

[13] G. Gambarini, S. Agosteo, U. Danesi, F. Garbellini, B. Lietti, M. Mauri, and G. Rosi, *Imaging and Profiling of Absorbed Dose in Neutron Capture Therapy*.
IEEE Trans. Nucl. Sci. **48**(3) (2001) 780-784.

[14] D. W. Vehar and P. J. Griffin, Development of an Alanine Dosimeter for Gamma Dosimetry in Mixed Environments - Summary of Research.
SAND94-0202, Sandia National Laboratories (1994).

[15] M. Marrale, M. Brai, G. Gennaro, A. Triolo, A. Bartolotta, M. C. D'Oca and G. Rosi, *Alanine blends for ESR measurements of thermal neutron fluence in a mixed radiation field*.
Rad. Prot. Dos. **126** (2007) 631-635.

[16] C. Baldock, *Historical overview of the development of gel dosimetry: a personal perspective*.
J. of Phys.: Conf. Ser.. **56** (2006) 14-22.

[17] C. Baldock, *Historical overview of the development of gel dosimetry: another personal perspective*.
J. of Phys.: Conf. Ser.. **164** (2009) 012002.

[18] X. G. Xu, B. Bednarz and H. Paganetti, *A review of dosimetry studies on external-beam radiation treatment with respect to second cancer induction*.
Phys. Med. Biol. **53** (2008) R193-R241.

[19] C. X. Yu, J. Amies and M. Svatos, *Planning and delivery of intensity-modulated radiation therapy*.
Med. Phys. **35**(12) (2008) 5233-5241.

[20] L. J. Schreiner, *Where does gel dosimetry fit in the clinic?*.
J. of Phys.: Conf. Ser.. **164** (2009) 012001.

[21] M. J. Day and G. Stein, *Chemical effects of ionizing radiation in some gels*.
Nature **166** (1950) 146-147.

[22] J. C. Gore, Y. S. Kang and R. J. Schulz, *Measurement of radiation dose distributions by nuclear magnetic resonance (NMR) imaging*.
Phys. Med. Biol. **29** (1984) 1189-1197.

[23] H. Fricke and S. Morse, *The chemical action of roentgen rays on dilute ferrous sulphate solutions as a measure of radiation dose*.
Am. J. Roentgenol. Radium Therapy Nucl Med. **18** (1927) 430-432.

[24] A. Appleby, E. A. Christman and A. Leghrouz, *Imaging of spatial radiation dose distribution in agarose gels using magnetic resonance*.
Med. Phys. **14** (1986) 382-384.

[25] A. Appleby and A. Leghrouz, *Imaging of radiation dose by visible color development in ferrous-agarose-xylenol orange gels*.
Med. Phys. **18**(2) (2009) 309-312.

[26] C. Baldock, P. J. Harris, A. R. Piercy and B. Healy, *Experimental determination of the diffusion coefficient in two-dimensions in ferrous sulphate gels using the finite element method*.
Phys. Eng. Sci. Med. **24**(1) (2001) 19-30.

[27] F. E. Hoecker, and I. W. Watkins, *Radiation polymerization dosimetry*.
Int. J. Appl. Rad. Isotop. **3** (1958) 31-35.

[28] M. Lepage, M. Jayasekera, S. Å. J. Bäck and C. Baldock, *Dose resolution optimization of polymer gel dosimeters using different monomers*.
Phys. Med. Biol. **46** (2001) 2665-2680.

[29] C. Baldock, R. P. Burford, N. Billingham, G. S. Wagner, S. Patval, R. D. Badawi and S. F. Keevil, *Experimental procedure for the manufacture and calibration of polyacrylamide gel (PAG) for magnetic resonance imaging (MRI) radiation dosimetry*.
Phys. Med. Biol. **43** (1998) 695-702.

[30] P. M. Fong , D. C. Keil, M. D. Does and J. C. Gore, *Polymer gels for magnetic resonance imaging of radiation dose distributions at normal room atmosphere*.
Phys. Med. Biol. **46** (2001) 3105-3113.

[31] R. J. Senden, P. De Jean, K. B. McAuley and L. J. Schreiner, *Polymer gel dosimeters with reduced toxicity: a preliminary investigation of the NMR and optical doseresponse using different monomers*.
Phys. Med. Biol. **51** (2006) 3301-3114.

[32] J. C. Gore, M. Ranade, M. J. Maryañski and R. J. Schulz, *Radiation dose distributions in three dimensions from tomographic optical density scanning of polymer gels: I. Development of an optical scanner*.
Phys. Med. Biol. **41** (1996) 2695-2704.

[33] M. Hilts, C. Audet, C. Duzenli and A. Jirasek, *Polymer gel dosimetry using x-ray computed tomography: a feasibility study*.
Phys. Med. Biol. **45** (2000) 2559-2571.

[34] C. Baldock, L. Rintoul, S. F. Keevil, J. M. Pope and G. A. George, *Fourier Transform Raman spectroscopy of polyacrylamide gels (PAGs) for radiation dosimetry*.
Phys. Med. Biol. **43** (1998) 3617-3627.

[35] M. Mather, A. K. Whittaker, C. Baldock, *Ultrasound evaluation of polymer gel dosimeters*.
Phys. Med. Biol. **47** (2002) 1449-1458.

[36] Y. De Deene, G. Pittomvils and S. Visalatchi, *The influence of cooling rate on the accuracy of normoxic polymer gel dosimeters*.
Phys. Med. Biol. **52** (2007) 2719-2728.

[37] G. Gambarini, C. Birattari, M. Mariani, R. Marchesini, L. Pirola, P. Prestini, M. Sella and S. Tomatis, *Study of light transmittance from layers of Fricke-xylenol-orange-gel dosimeters*.
Nucl. Instr. and Meth. B **213** (2004) 321-324.

[38] G. Gambarini, M. Carrara, S. Gay and S. Tomatis, *Dose imaging with gel-dosimeter layers: optical analysis and dedicated software*.
Rad. Prot. Dos. **213** (2004) 321-324.

[39] M. Carrara, G. Gambarini, S. Tomatis and M. Valente, *Dose distribution measurements by means of gel-layer dosimeters. Evaluation of algorithms*

for artifacts amendment.
Nucl. Instr. Meth. A **579** (2007) 334-338.

[40] M. Carrara, G. Gambarini, G. Bartesaghi, C. Fallai, A. Negri, *A procedure to mathematically amend possible thickness disuniformities in gel-layer dosimetry*.
J. of Phys: Conf. Ser. **164** (2009) 012007.

[41] G. Gambarini, M. Carrara and M. Valente, *3D-Reconstruction of absorbed dose obtained from gel-dosimeter-layers*.
In: Proceedings of 9th ICATPP Conference on Astroparticle, Particle, Space Physics, Detectors and Medical Physics Applications (2006) 705-709. Ed. World Scientific (ISBN 981-256-798-4).

[42] S. Tomatis, M. Carrara, G. Gambarini, R. Marchesini and M. Valente, *Gel-layer dosimetry for dose verification in intensity modulated radiation therapy*.
Nucl. Instr. Meth. A **580** (2007) 506-509.

[43] G. Gambarini, C. Birattari, C. Colombi, L. Pirola and G. Rosi, *Fricke Gel Dosimetry in Boron Neutron Capture Therapy*.
Rad. Prot. Dos. **101** (2002) 419-422.

[44] M. Carrara, S. Tomatis, G. Zonca, G. Gambarini, G. Bartesaghi, C. Tenconi, A. Cerrotta and C. Fallai, *Fricke Gel Dosimeters for the Measurement of the Anisotropy function of a HDR Ir-192 brachytherapy source*.
In: Proceedings of 11th ICATPP Conference on Astroparticle, Particle, Space Physics, Detectors and Medical Physics Applications. In press.

[45] G. Gambarini, V. Collia, S. Gaya, C. Petrovich, L. Pirola and G. Rosi, *In-phantom imaging of all dose components in boron neutron capture therapy by means of gel dosimeters*.
App. Rad. Isot. **61**(5) (2004) 759-73.

[46] S. Å. J. Bäck, J. Medin, P. Magnusson, P. Olsson, E. Grusell and L. E. Olsson, *Ferrous sulphate gel dosimetry and MRI for proton beam dose measurements*.
Phys. Med. Biol. **44** (1999) 1983-1996.

[47] MCNP. A general Monte Carlo N-particle code, version 5. X5 Monte Carlo Team, Los Alamos National Laboratory (2003).

[48] J. Burian, S. Flibor, M. Marek, J. Rejchrt, L. Viererbl and I. Tomandl, *Physics for BNCT*.
J. of Phys: Conf. Ser. **41** (2001) 174-86.

[49] G. Gambarini, F. Gallivanone, M. Carrara, S. Nagels, L. Vogdander, G. Hamper and L. Pirola, *Study of reliability of TLDs for the photon dose mapping in reactor neutron fields for BNCT*.
Rad. Meas. **43** (2008) 1118-1122.

[50] P. J. Binns, K. J. Riley, O. K. Harling, W. S. Kiger, P. M. Munck af Rosenschöld , V. Giusti, J. Capala, K. Sköld, I. Auterinen, T. Serén , P. Kotiluoto, J. Uusi-Simola, M. Marek, L. Viererbl and F. Spurny, *An international dosimetry exchange for boron neutron capture therapy, Part I: Absorbed dose measurement*.
Med. Phys. **32** (2005) 3729-3736.

[51] F. D. Brooks and H. Klein, *Neutron spectrometry - historical review and present status*.
Nucl. Instr. Meth. A **476** (2002) 1-11.

[52] D. J. Thomas and A. V. Alevra, *Bonner sphere spectrometers - a critical review*.
Nucl. Instr. Meth. A **476** (2002) 12-20.

[53] V. F. Sears, *Neutron scattering lengths and cross sections*.
Neutron News **3**(3) (1992) 29-37.

[54] V. Dangendorf, A. Demian, H. Friedrich, V. Wagner, A. Breskin, R. Chechik, S. Gibrekhterman and A. Akkerman, *Thermal Neutron Imaging Detectors Combining Novel Composite Foil Convertors and Gaseous Electron Multipliers*.
Nucl. Inst. Meth. A **350** (1994) 503-510.

[55] H. Friedrich, V. Dangendorf and A. Bräuning-Demian, *Position-Sensitive Thermal Neutron Detector with 6Li foil Converter Coupled to Wire Chambers*.
App. Phys. A **74** (2002) 124-126.

[56] M. Reginatto and P. Goldhagen, MAXED, A Computer Code For The Deconvolution Of Multisphere Neutron Spectrometer Data Using The Maximum Entropy Method.
Environmental Measurements Laboratory. USDOE Report EML 595 (1998).

[57] M. Reginatto and P. Goldhagen, *MAXED, A Computer Code For Maximum Entropy Deconvolution Of Multisphere Neutron Spectrometer Data.* Health Phys. **77** (1999) 579-583.

[58] W. von der Linden, *Maximum-entropy data analysis.* Appl. Phys. A **60** (1995) 155-165.

[59] M. Cortesi, R. Alon, R. Chechik, A. Breskin, D. Vartsky and V. Dangendorf, *Investigations of a THGEM-based imaging detector*. JINST **2** (2007) P09002.

[60] V. Dangendorf, G. Laczko, M. Reginatto, D. Vartsky, M. Goldberg, I. Mor, A. Breskin and R. Chechik, *Detector for time-of-flight fast-neutron radiography. 1. Neutron counting gas detector*. Nucl. Instr. Meth. A **542** (2005) 197-205.

[61] O. Jagutzki, J. S. Lapington, L. B. C. Worth, U. Spillmann, V. Mergel and H. Schmidt-Böcking, *Position sensitive anodes for MCP read-out using induced charge measurement.* Nucl. Instr. Meth. A **477** (2002) 256-261.

[62] M. S. Dixit, J. Dubeau, J. P. Martin and C. K. Sachs, *Position sensing from charge dispersion in micro-pattern gas detectors with a resistive anode*. Nucl. Instr. Meth. A **518** (2004) 721-727.

[63] Korea Atomic Energy Research Institute, Table of Nuclides. (http://atom.kaeri.re.kr/)

[64] C. Shalem, R. Chechik, A. Breskin and K. Michaeli, *Advances in Thick GEM-like gaseous electron multipliers-Part I: atmospheric pressure operation*. Nucl. Instr. Meth. A **558** (2006) 475-489.

[65] R. Alon, J. Miyamoto, M. Cortesi, A. Breskin, R. Chechik, I. Carne, J. M. Maia, J. M. F. dos Santos, M. Gai, D. McKinsey and V. Dangendorf, *Operation of a Thick Gas Electron Multiplier (THGEM) in Ar, Xe and Ar-Xe*. JINST **3** (2008) P01005.

[66] D. N. Sitter, J. S. Goddard and R. K. Ferrell, *Method for the measurement of the modulation transfer function of sampled imaging systems from bar-target patterns*. Appl. Optics **34** (1995) 746-751.

[67] The Stopping and Range of Ions in Matter.
(http://www.srim.org/)

[68] M. Cortesi, V. Peskov, G. Bartesaghi, J. Miyamoto, S. Cohen, R. Chechik, J. M. Maia, J. M. F. dos Santos, G. Gambarini, V. Dangendorf and A. Breskin, *THGEM operation in Ne and Ne/CH_4*.
JINST **4** (2009) P08001.

[69] I. Lehraus, R. Matthewson and W. Tejessy, *Pressure dependence of the relativistic rise in Neon and highest attainable ionization sampling resolution in Neon, Argon, Ethylene and Propane*.
IEEE Trans. Nucl. Sci. **30** (1983) 50-59.

[70] J. C. Bowe, *Drift Velocity of Electrons in Nitrogen, Helium, Neon, Argon, Krypton, and Xenon*.
Phys. Rev. **117** (1960) 1411-1415.

[71] T. Ferbel, Experimental Techniques in High Energy Physics, Addison-Wesley Pub. Comp., Inc., Menlo Park, California (1987).

[72] R. Nolte, M. S. Allie, R. Böttger, F. D. Brooks, A. Buffler, V. Dangendorf, H. Friedrich, S. Guldbakke, H. Klein, J. P. Meulders, D. Schlegel, H. Schuhmacher and F. D. Smit, *Quasi-monoenergetic neutron reference fields in the energy range from thermal to 200 MeV*.
Rad. Prot. Dos. (2004) **110** 97-102.

[73] D. B. Pelowitz,, MCNPX user's manual. Version 2.5.0. (2005). LA-CP-05-0369, Los Alamos Laboratory.

[74] J. Burian, M. Marek, J. Rataj and S. Flibor: The experience from the construction of BNCT facility at the LVR-15 reactor.
In: International Atomic Energy Agency, Current status of neutron capture therapy. IAEA-TECDOC-1223. Vienna (2001). ISSN 1011-4289.

[75] J. Burian, M. Marek, J. Rataj, S. Flibor, J. Rejchrt, L. Viererbl, F. Sus, H. Honova, L. Petruzelka, K. Prokes, F. Tovarys, V. Dbaly, V. Benes, P. Kozler, J. Honzatko, I. Tomandl and V. Mares, *Report on the first patient group of the phase I BNCT trial at the LVR-15 reactor*.
Int. Congr. Ser. **1259** (2004) 27-32.